CFD simulation of bubbly flow under pool scrubbing conditions

Zur Erlangung des akademischen Grades
eines Doktors der Ingenieurwissenschaften (Dr.-Ing.)
von der KIT-Fakultät für Maschinenbau des
Karlsruher Instituts für Technologie (KIT)
genehmigte

DISSERTATION

von

M. Sc. Zhongkai Mei

Tag der mündlichen Prüfung: 01. Dezember 2023
Hauptreferent: Prof. Dr.-Ing. Xu Cheng
Korreferent: Prof. Jinbiao Xiong

I declare that I have developed and written the enclosed thesis completely by myself, and have not used sources or means without declaration in the text.

Karlsruhe, 11.09.2023

. . . .

(Zhongkai Mei)

Acknowledgements

I would like to thank Prof. Dr.-Ing. Xu Cheng to offer me the chance to pursue a Ph.D. degree. With his instructions and comments, I go through a complete cycle of academic training, which benefits me a lot. After numerous discussions with him, my overall academic capability and logical thinking have improved significantly.

I would also like to thank Prof. Jinbiao Xiong for being the second supervisor of the thesis, which provided valuable suggestions for my thesis.

I want to express thanks to all my colleagues in IATF in terms of all passing age and happiness. In particular, I need to thank Dr. Fanli Kong for her time and discussion, which helped me considerably. It is a joyful life experience for me to share treasured memories with all friendly people in the welcoming environment of IATF.

Finally, I would like to thank my parents and friends. Without their help and support, I wouldn’t have had enough courage and confidence to overcome numerous difficulties in the past four years.

Zhongkai Mei

Karlsruhe, 11.09.2023

Abstract

Nuclear safety plays a paramount role in nuclear power plants because the leakage of radioactive materials could result in lethal damage to the environment. In the hypothetical scenarios of coolant loss, the radioactive fission products could escape from the core and move to the pathway. To avoid the radioactive products from releasing into the main system, the water pool, namely the suppression pool in boiling water reactors or the secondary side of a steam generator in pressurized water reactors is utilized to enhance aerosol retention in the form of bubble scrubbing [3]. As a well-established and high-efficiency method, pool scrubbing has been identified as a high-priority nuclear safety research topic after several post-Fukushima activities [4]. However, the current pool scrubbing codes may predict inaccurate decontamination factor because some relevant retention processes in the liquid pool are not included within the available models [4, 7]. As the improved aspects of the single bubble model in the pool scrubbing codes [7], bubble interfacial area and aerosol residence time are particularly investigated in this work, where the CFD approach is utilized to obtain the details in bubble dynamics and aerosol transport in the case of a single bubble with internal particles rising in quiescent liquid.

Since aerosol transport occurs over the whole bubble surface, the three-dimensional bubble interfacial area affects aerosol decontamination factor dramatically. The present pool scrubbing codes [5-7] generally assumed fixed bubble shape, such as the ellipsoidal shape, whereby bubble interfacial area could be calculated accordingly. In the experiments [9-10], significant deformation of bubbles could be observed, which introduces a large deviation in bubble interfacial area. In the meantime, the effect of bubble deformation on aerosol decontamination has been confirmed in the experimental work of Abe et al. [11]. In the absence of bubble shape assumption, bubble interfacial area in this work is calculated based on the VOF method with the concept of isoface, where the credibility of CFD approach is examined with caution. After the validation of bubble dynamics, the transient evolution in long-term bubble dynamics is investigated and the velocity-shape dependence is particularly analyzed. When qualitative analysis of bubble dynamics is finished, the correlation development of bubble terminal interfacial area is carried out based on extensive simulations with a wide coverage of physical properties, which provides a comprehensive empirical correlation eventually based on the curve fitting of the numerical dataset.

In terms of aerosol residence time, the coupling of VOF and LPT methods is performed to resolve aerosol motion in the transient bubble flow field, whereby aerosol residence time could be tracked dynamically. It should be mentioned that particle interfacial behavior on the bubble surface is generally disregarded in previous numerical investigations on pool scrubbing. Most of previous works assumed that particles are decontaminated immediately once the particle reaches the bubble surface. This assumption could be over-simplified particularly when particle size is small enough. Regarding the aerosol size in the accidents, the estimated particle size injected into the scrubbing pool is from 0.01 to 2 μm approximately [2], whereas a single micron

particle impacting the gas-liquid interface could present different interfacial behaviors according to experimental observations [12-13]. In this case, the neglect of particle interfacial behavior could result in considerable overestimation of aerosol decontamination factor. Therefore, we refer to the experiments of a single particle impacting the stagnant gas-liquid interface and analyze the process of multi-particle hitting the moving bubble surface. Through the dimensionless analysis of the particle momentum equation, a new criterion based on particle Weber number is derived and a developed interfacial penetration model is coupled with the VOF-LPT method to include the effect of particle interfacial behavior on aerosol decontamination.

The developed interfacial penetration model is calibrated by the benchmark data of single bubble decontamination experiment by Fujiwara et al. [25], which is then applied in parametric studies of influential factors on aerosol transport behaviors. After the qualitative analysis of the effects of both bubble dynamics and aerosol properties on aerosol transport behaviors, residence-time distribution analysis is introduced into aerosol decontamination process to account for temporal removal behavior at first. As for the investigation on aerosol mean residence time, considering that swarm bubbles of pool scrubbing in experiments could generally come to the quasi-stable status, particles in simulation are injected into the rising bubble as the bubble comes to the terminal status, which is to track aerosol residence time under the circumstance of a terminal internal flow field. After conducting a comprehensive analysis, a key parameter is applied to characterize aerosol decontamination process within bubble swarm zone under pool scrubbing conditions, which is found to affect aerosol mean residence time critically.

Kurzfassung

Die nukleare Sicherheit ist von höchster Wichtigkeit in Kernkraftwerken, da das Austreten von radioaktiven Materialien zu verheerenden Umweltschäden führen könnte. In hypothetischen Szenarien des Kühlmittelverlusts könnten radioaktive Spaltprodukte aus dem Kern austreten und sich weiterbewegen. Um zu verhindern, dass die radioaktiven Produkte in das Hauptsystem gelangen, wird in Siedewasserreaktoren oder auf der Sekundärseite eines Dampferzeugers in Druckwasserreaktoren ein Wasserbecken, auch Suppressionsbecken genannt, verwendet. Dies verbessert die Aerosolretention durch das sogenannte Pool Scrubbing [3]. Nach weiteren vergleichbaren Aktivitäten wie in Fukushima wurde Pool Scrubbing als etablierte und hoch effiziente Methode im Bereich der nuklearen Sicherheit identifiziert [4]. Die aktuellen Pool Scrubbing-Codes können jedoch die Dekontaminationsfaktoren nur ungenau vorhersagen, da einige relevante Retentionsprozesse im Flüssigkeitsbecken in den verfügbaren Modellen nicht enthalten sind [4, 7]. In dieser Arbeit werden besonders die Blasengrenzflächen sowie die Verweilzeit der Aerosole mit Hilfe eines verbesserten Einzelblasenmodells für Pool Scrubbing-Codes untersucht [7]. Dabei wird der CFD-Ansatz verwendet, um Details zur Blasendynamik und zum Aerosoltransport im Fall einer einzelnen Blase mit internen Partikeln in ruhiger Flüssigkeit zu erhalten.

Da der Aerosoltransport über die gesamte Oberfläche der Blase erfolgt, beeinflusst die dreidimensionale Blasengrenzfläche den Aerosoldekontaminationsfaktor dramatisch. Die aktuellen Pool Scubbing-Codes [5-7] gehen im Allgemeinen von einer festen Blasenform aus, wie z. B. der ellipsoiden Form, wodurch die Blasengrenzfläche entsprechend berechnet werden kann. In den Experimenten [9-10] konnte jedoch eine erhebliche Verformung der Blasen beobachtet werden, was eine große Abweichung der Blasengrenzfläche mit sich bringt. Gleichzeitig wurde der Einfluss der Blasenverformung auf die Aerosoldekontamination in der experimentellen Arbeit von Abe et al. [11] bestätigt. Ohne Annahmen über die Blasenform, wird in dieser Arbeit die Blasengrenzfläche auf der Grundlage der VOF-Methode mit Hilfe des „isoface"-Konzepts berechnet. Hierbei wird der Glaubwürdigkeit des CFD-Ansatzes eine besondere Aufmerksamkeit geschenkt. Nach der Validierung der Blasendynamik wird die transiente Entwicklung in der Langzeit-Blasendynamik untersucht und die Abhängigkeit zwischen der Geschwindigkeit und der Blasenform wird besonders analysiert. Nach Abschluss der qualitativen Analyse der Blasendynamik erfolgt die Entwicklung einer Korrelation für die terminale Blasengrenzfläche. Dies geschieht auf der Grundlage umfangreicher Simulationen mit einem großen Umfang an physikalischen Eigenschaften. Schließlich wird die Korrelation an die numerischen Datensätze angepasst.

In Bezug auf die Verweilzeit der Aerosole wird die Kopplung von VOF- und LPT-Methoden durchgeführt, um die Bewegung von Aerosolen im transienten Blasenströmungsfeld aufzulösen, wodurch die Verweilzeit dynamisch verfolgt werden kann. Es sei darauf hingewiesen, dass das Verhalten von Partikeln an der Blasenoberfläche in früheren numerischen Untersuchungen zum Pool Scrubbing im Allgemeinen nicht berücksichtigt wurde. In den meisten früheren Arbeiten

wurde angenommen, dass Partikel sofort ausgewaschen werden, sobald das Partikel die Blasenoberfläche erreicht. Diese Annahme könnte besonders dann zu einfach sein, wenn die Partikelgröße klein genug ist. In Bezug auf die Aerosolgröße bei Unfällen liegt die geschätzte Partikelgröße, die in das Reinigungsbecken eingebracht wird, bei etwa 0,01 bis 2 µm [2]. Währenddessen kann ein einzelnes Mikron-Partikel je nach experimentellen Beobachtungen unterschiedliches Verhalten an der Gas-Flüssig-Grenzfläche aufweisen [12-13]. In diesem Fall könnte die Vernachlässigung des Verhaltens von Partikeln an der Grenzfläche zu einer erheblichen Überschätzung des Aerosoldekontaminationsfaktors führen. Daher beziehen wir uns auf die Experimente eines einzelnen Partikels, das auf die ruhende Gas-Flüssig-Grenzfläche auftrifft und analysieren den Prozess, bei dem mehrere Partikel auf die bewegte Blasenoberfläche treffen. Durch die dimensionslose Analyse der Partikel-Impuls-Gleichung wird ein neues Kriterium auf Grundlage der Partikel-Weber-Zahl abgeleitet und ein entwickeltes Grenzflächenpenetration-Modell wird mit der VOF-LPT-Methode gekoppelt, um den Einfluss des Verhaltens von Partikeln an der Grenzfläche auf die Aerosoldekontamination zu berücksichtigen.

Das entwickelte Modell für die Grenzflächenpenetration wird anhand der Benchmark-Daten des Experiments zur Dekontamination von Einzelblasen von Fujiwara et al. [25] kalibriert und in parametrischen Studien zu Einflussfaktoren auf das Verhalten des Aerosoltransports angewendet. Nach der qualitativen Analyse der Auswirkungen sowohl der Blasendynamik als auch der Aerosoleigenschaften auf das Verhalten des Aerosoltransports, wird die Analyse der Verteilung der Verweilzeit eingeführt, um das zeitliche Entfernungsverhalten zu berücksichtigen. In Bezug auf die Untersuchung der mittleren Verweilzeit der Aerosole wird ein quasi stationärer Zustand der Blasenschwärme in Pool Scrubbing Experimenten berücksichtigt. Sobald dieser Zustand von einer Blase erreicht wurde, werden in der Simulation Partikel in die aufsteigende Blase injiziert. Damit kann die Verweilzeit der Aerosole unter den Bedingungen eines terminalen internen Strömungsfeldes verfolgt werden.

Contents

Acknowledgements iv
Abstract vi
Kurzfassung viii
Contents x
List of Figures xii
List of Tables xvi
Nomenclature xviii
1 Introduction 1
  1.1 Background 1
  1.2 Objectives of this study 4
2 State of the Art 7
  2.1 Experimental investigation of pool scrubbing 7
    2.1.1 Physical operating conditions 7
    2.1.2 Particle characteristics 8
    2.1.3 A brief summary 9
  2.2 Numerical calculation of decontamination factor 9
    2.2.1 Overall decontamination factor calculation 10
    2.2.2 Local decontamination factor calculation 10
    2.2.3 A brief summary 12
  2.3 Bubble shape and interfacial area 13
    2.3.1 Single bubble shape 13
    2.3.2 Three-dimensional interfacial area 14
    2.3.3 A brief summary 17
  2.4 Particle deposition on gas-liquid interface 17
    2.4.1 Particle deposition mechanism 17
    2.4.2 Particle interfacial behavior 20
    2.4.3 Aerosol residence time 23
    2.4.4 A brief summary 24
3 Fundamentals of Methodology 25

3.1 The description of VOF method 25
3.1.1 The interface compression scheme 26
3.1.2 The interface advection scheme 27
3.2 The description of LPT method 28
3.3 The development of the interfacial penetration model 29
3.4 Residence-time distribution analysis 33
3.5 Numerical configuration 34
3.6 Parameter normalization and dimensionless numbers 35
4 Bubble Dynamics and Topology 37
4.1 Selection and validation of numerical approach 37
4.2 Bubble dynamics 42
4.3 Modeling of bubble terminal interfacial area 48
4.3.1 Correlation development in axisymmetric regime 48
4.3.2 Correlation development in oscillatory regime 51
4.3.2.1 Bubble hydrodynamics phenomenon 52
4.3.2.2 Bubble breakup 54
4.3.2.3 Correlation development 58
4.3.3 A comprehensive description of bubble terminal interfacial area 61
4.4 Conclusion 63
5 Particle Motion inside Bubbles 65
5.1 Validation of interfacial penetration model based on experimental data 65
5.2 Analysis of aerosol trajectory in the gas phase 70
5.3 Parametric study of principal influential factors based on We_p criterion 73
5.3.1 Influence of particle size and density 73
5.3.2 Influence of gas-liquid surface tension 75
5.4 Influence of *Eo* and *Ga* numbers on aerosol transport behavior 76
5.4.1 Influence of *Eo* numbers 77
5.4.2 Influence of *Ga* numbers 81
5.5 Aerosol residence time 84
5.5.1 Investigation of aerosol residence-time distribution 84
5.5.2 Investigation of aerosol mean residence time 86
5.6 Conclusion 90
6 Conclusion and Outlook 91
Bibliography 93
List of Publications 98

List of Figures

Fig. 1.1. Schematic of pool scrubbing process. 2

Fig. 1.2. Schematic of single bubble model in SPARC-90 [7]. 3

Fig. 1.3. Description of task classifications. 6

Fig. 2.1. Representation of Hill's spherical vortex [50]. 11

Fig. 2.2. Method classification in calculating local aerosol decontamination. 12

Fig. 2.3. Typical bubble shape evolution versus bubble size from experimental observations [55] at water temperature equal to 29°C. 13

Fig. 2.4. Visualization of aerosol transport from the experimental work of Abe et al. [11]. 14

Fig. 2.5. Computing schematic of bubble interfacial area in the experiment [22]. 15

Fig. 2.6. Theoretical calculation results of a specific case with rising height 20 cm and bubble size 4 mm by the work Charvet et al. [33]. 20

Fig. 2.7. Observation of particle interfacial behavior on the water surface in the experiment [73]. 21

Fig. 2.8. Observation of oblique impact on the water surface in the experiment [78]. 22

Fig. 2.9. Observation of micron hydrophilic particles in the experiment [81]. 23

Fig. 3.1. Schematic of particle motion inside rising bubble. 29

Fig. 3.2. Schematic of interaction between particle and gas-liquid interface. 30

Fig. 3.3. Schematic of the interfacial penetration model. 32

Fig. 3.4. Schematic of a bubble with internal aerosol rising in quiescent liquid. 34

Fig. 4.1. Wall effect on bubble terminal interfacial area. 37

Fig. 4.2. Mesh sensitivity study of isoAdvector and MULES for a 6 mm bubble. 38

Fig. 4.3. Validation of bubble aspect ratio in simulation by experimental data. 39

Fig. 4.4. Validation of bubble terminal velocity in simulation by experimental data. 39

Fig. 4.5. Comparison of bubble initial interfacial area for isoAdvector and MULES 40

Fig. 4.6. Comparison of bubble terminal interfacial area for isoAdvector and MULES based on experimental data.. 41

Fig. 4.7. Effect of Galilei numbers on bubble interfacial area for isoAdvector and MULES. 41

Fig. 4.8. Effect of Eötvös numbers on bubble interfacial area for isoAdvector and MULES. 41

Fig. 4.9. Bubble trajectory component and projection with bubble size equal to 7 mm. 42

Fig. 4.10. Temporal evolution of bubble interfacial area and rising velocity with bubble size equal to 7 mm. 43

Fig. 4.11. Bubble shape evolution in the quasi-stable stage. 43

Fig. 4.12. Bubble trajectory component and projection with bubble size equal to 6 mm. 44

Fig. 4.13. Temporal evolution of bubble interfacial area and rising velocity with bubble size equal to 6 mm. 45

Fig. 4.14. Velocity-shape dependency in the damped oscillatory stage. 45

Fig. 4.15. Temporal evolution of bubble internal flow field. 46

Fig. 4.16. Velocity-shape dependency for a single oscillatory period.................................... 46

Fig. 4.17. Velocity-shape dependency in the context of straight and helical trajectories........ 47

Fig. 4.18. Coverage of *Ga* and *Eo* numbers for curve fittings base on the work [23]............ 48

Fig. 4.19. Dependence of bubble interfacial area on *Eo* and *Ga* numbers. 49

Fig. 4.20. Terminal bubble shape versus *Ga* and *Eo* numbers. 50

Fig. 4.21. Three-dimensional surface fitting of bubble terminal interfacial area. 51

Fig. 4.22. Three observed bubble behaviors in simulation.. 52

Fig. 4.23. Temporal variation in bubble central thickness. 53

Fig. 4.24. Temporal variation in bubble interfacial area. 54

Fig. 4.25. Relationship between bubble deformation factor and central thickness with *Eo*=4.5. 54

Fig. 4.26. Relationship between bubble deformation factor and central thickness with *Eo*=5.55

Fig. 4.27. Transient bubble shape evolution with *Eo* equal to 4.5. 56

Fig. 4.28. Transient bubble shape evolution with *Eo* equal to 5. 56

Fig. 4.29. Three-dimensional bubble breakup process. 57

Fig. 4.30. Phase plot of bubble breakup behaviors.. 58

Fig. 4.31. Relationship between bubble maximum deformation and bubble breakup behaviors. 58

Fig. 4.32. Dependency of bubble terminal interfacial area on *Ga* and *Eo* numbers. 59

Fig. 4.33. Comparison between predicted and experimental data. 60

Fig. 4.34. Comparison of empirical correlations with water temperature equal to 8 and 29 °C. 61

Fig. 4.35. Bubble transient interfacial area with *Eo* equal to 1. 62

Fig. 4.36. Bubble terminal interfacial area with *Eo* equal to 1. 63

Fig. 5.1. Experimental setup of the single bubble experiment by Fujiwara et al. [25]. 66

Fig. 5.2. Aerosol size distribution in experiment [25] and in simulation. 67

Fig. 5.3. Comparison of different criteria based on the benchmark data. 67

Fig. 5.4. Comparison of aerosol size distribution in the beginning and at the end. 68

Fig. 5.5. Transient decontamination factor and exponential trend versus bubble rising height based on the benchmark data. 68

Fig. 5.6. Comparison of aerosol size distribution at different bubble rising heights based on the benchmark data. 69

Fig. 5.7. Temporal evolution of aerosol motion inside the rising bubble. 69

Fig. 5.8. Spatial position and temporal removal on bubble surface. 70

Fig. 5.9. Temporal particle horizontal and vertical displacement. 72

Fig. 5.10. Temporal particle turning and intersection angle. 72

Fig. 5.11. Temporal evolution of aerosol internal circulation. 73

Fig. 5.12. Parametric study of particle size effect on aerosol transport. 74

Fig. 5.13. Comparison of particle size effect on aerosol removal position. 74

Fig. 5.14. Parametric study of particle density effect on aerosol transport. 75

Fig. 5.15. Bubble rising height with different gas-liquid surface tension coefficients. 76

Fig. 5.16. Parametric study of gas-liquid surface tension effect on aerosol transport. 76

Fig. 5.17. Variation in terminal decontamination factor with Eötvös numbers. 78

Fig. 5.18. Influence of Eötvös numbers on aerosol velocity distribution. 78

Fig. 5.19. Sensitivity study of the influence of timestep on aerosol removal distribution. 79

Fig. 5.20. Influence of Eötvös numbers on aerosol removal distribution. 80

Fig. 5.21. Mechanism of how ultrafine aerosol deposits on the bubble surface affected by gas-liquid surface tension. 80

Fig. 5.22. Dependency of aerosol removal distribution on changing Eötvös numbers. 81

Fig. 5.23. Variation in terminal decontamination factor with Galilei numbers. 82

Fig. 5.24. Influence of Galilei numbers on aerosol velocity distribution. 82

Fig. 5.25. Influence of Galilei numbers on aerosol removal distribution. 83

Fig. 5.26. Dependency of aerosol removal distribution on changing Galilei numbers. 83

Fig. 5.27. Temporal evolution of aerosol residence-time distribution function with high surface tension. 85

Fig. 5.28. Temporal evolution of aerosol residence-time distribution function with low surface tension. 85

Fig. 5.29. Aerosol mean residence time and variance with various sized particles. 86

Fig. 5.30. Dependency of aerosol decontamination on bubble size, particle size and surface tension in the context of terminal flow field. 87

Fig. 5.31. Evolution of *E*-curve in the context of terminal flow field. 88

Fig. 5.32. Dependency of aerosol mean residence time on bubble size, particle size and surface tension in the context of terminal flow field. 89

Fig. 5.33. Distribution of aerosol mean residence time. 89

List of Tables

Table 4.1 Physical properties for validation. 38

Table 4.2 Physical properties in the air-water system. 42

Table 4.3 Physical properties in the high *Ga* system. 51

Table 4.4 Terminal interfacial area in the high *Ga* system 59

Table 4.5 Bubble terminal interfacial area under different conditions. 63

Table 5.1 Initial particle position 71

Table 5.2 Physical properties of parametric studies for aerosol transport. 73

Table 5.3 Physical properties of changeful bubble dynamics in simulation. 77

Table 5.4 Physical properties applied in simulation. 84

Table 5.5 Investigated cases for aerosol mean residence time. 87

Nomenclature

a	a half of bubble width, m.
A	bubble surface area, m^2.
A_i	surface area of the elementary triangles of an isoface, m^2.
b	a half of bubble height, m.
B_i	boundary list of given cell, dimensionless.
C_i	ID of cell i, dimensionless.
C_α	comprehensive factor, dimensionless.
C_c	Cunningham correction factor, dimensionless.
C_p	particle concentration, kg/m^3.
$C_{\mathrm{p},0}$	initial particle concentration, kg/m^3.
d	diameter, m.
D_inlet	injector size, m.
D_B	particle diffusion coefficient, dimensionless.
E	aspect ratio, dimensionless.
Eo	Eötvös number, dimensionless.
$E(t)$	residence time distribution function, s^{-1}.
$F(t)$	cumulative aerosol decontamination function, dimensionless.
F_j	face j of given cell, dimensionless.
F_σ	surface tension force on the bubble interface, N/m.
F_drag	drag force, N/m.
F_Br	Brownian force, N/m.
F_ST	surface tension force on the particle, N/m.
g	gravity acceleration, m/s^2.
Ga	Galilei number, dimensionless.
h	bubble rising height, m
$h(t)$	temporal bubble rising height, m
$H(\boldsymbol{x}, t)$	indicator field function, dimensionless.
k	coefficient, dimensionless.
k_B	Boltzmann's constant, m^{2}kg/s^{2}K.
k_i	coefficient of inertial impaction, dimensionless.
k_g	coefficient of gravitational deposition, dimensionless.
k_D	coefficient of Brownian diffusion, dimensionless.

$k_{\mathrm{interface}}$	interface curvature, dimensionless.
l	perpendicular distance from bubble arch centroid to central axis, m.
L	displacement, m.
L_{p}	particle displacement in interfacial process, m.
L^*_{xyz}	normalized particle mean displacement, dimensionless.
m	bubble arch centroid
m_{p}	particle mass, kg.
n	normal, dimensionless.
$n_{\mathrm{interface}}$	interfacial normal, dimensionless.
N	number, dimensionless.
N_{initial}	initial particle number, dimensionless.
N_{remain}	remained particle number, dimensionless.
$N(t)$	cumulative removed aerosol number, dimensionless.
p	pressure, pa.
R-squared	criterion of goodness, dimensionless.
R_{b}	bubble radius, m.
s	bubble arc length, m.
s_{ij}	auxiliary function, dimensionless.
Δt	time interval, s.
Δt^*	dimensionless time interval, dimensionless.
t	physical time, s.
t_{b}	bubble residence time, s.
t_{p}	particle penetration time, s.
T	temperature, K.
$u^*_{\mathrm{deposition}}$	particle deposition velocity, m/s.
u_1	particle initial velocity, m/s.
u_2	particle rebound velocity, m/s.
$u_{\mathrm{p,n}}$	particle normal velocity component, m/s.
$u'_{\mathrm{p,n}}$	particle normal velocity component after a timestep, m/s.
$u_{\mathrm{p,h}}$	particle horizontal velocity component, m/s.
$u_{\mathrm{interface}}$	bubble interface moving velocity, m/s.
U_{b}	bubble rising velocity, m/s.
U_{T}	bubble terminal velocity, m/s.
U_{p}	particle velocity, m/s.
U_{c}	particle centrifugal deposition velocity, m/s.
U_{v}	particle incoming vapor velocity, m/s.
U_{g}	particle gravitational settling velocity, m/s.
U_{B}	particle Brownian diffusion velocity, m/s.

U_{inlet}	inlet gas velocity, m/s.
U_{flow}	local gas streamline velocity, m/s.
U_{comp}	compressive velocity, m/s.
U^{*}_{cen}	bubble mass rising velocity, dimensionless.
$U(r, \varphi, z)$	fluid velocity function, dimensionless.
V	volume, m^3.
V_{i}	volume of cell i, m^3.
V_{b}	bubble volume, m^3.
$\Delta V_{\text{j}}(t, \Delta t)$	volume quantity transportation across face j, m^3.
We_{p}	particle Weber number, dimensionless.
We_{impact}	impact Weber number, dimensionless.
We_{inlet}	inlet Weber number, dimensionless.
$\boldsymbol{x}$	displacement vector, dimensionless.
x	displacement in x direction, m.
y	displacement in y direction, m.
y_i	actual value of bubble interfacial area, m^2.
$\hat{y}_i$	predicted value of bubble interfacial area, m^2.
$\bar{y}_i$	mean value of bubble interfacial area, m.
z	displacement in z direction, m.
z_{top}	positions at bubble top along bubble central axis, m.
z_{bottom}	positions at bubble bottom along bubble central axis, m.

Greek symbols

α_{g}	gas volume fraction, dimensionless.
β	angle between local interfacial normal and gravity vector, rad.
δ	distance between bubble top and bottom along central axis, m.
η_{total}	total particle collection efficiency, dimensionless.
θ	gas-solid contact angle, rad.
λ	mean free path of gas molecules, J/K.
μ	viscosity, Ns/m^2.
ρ	density, kg/m^3.
σ	gas-liquid surface tension coefficient, N/m.
σ^2	variance, dimensionless.
ς	Gaussian random numbers, dimensionless.
τ	particle relaxation time, s.
φ	contact angle between three-phase contact line and central axis, rad.
$\psi(\boldsymbol{x})$	Stokes stream function, dimensionless.

$\psi(r, \varphi, z)$	Stokes stream function with cylindrical coordinates, dimensionless.

Superscripts

*	normalization.

Subscripts

c	carrier phase.
g	gas phase.
l	liquid phase.
p	particle phase.
x	spatial direction x.
y	spatial direction y.
z	spatial direction z.

Abbreviations

BDF	bubble deformation factor.
CFD	Computational Fluid Dynamics.
CPD	cells per diameter.
DF	decontamination factor.
isoAdvector	isoAdvector scheme.
LPT	Lagrangian Particle Tracking.
MRT	aerosol mean residence time.
MULES	Multidimensional Universal Limiter with Explicit Solution.
PIMPLE	Pressure Implicit with Splitting of Operator.
SSE	residual sum of squares.
SST	total sum of squares.
VOF	Volume of Fluid.

1 Introduction

In this chapter, the background of this thesis will be introduced. After the indication of deficiency in previous studies, the objectives of this thesis will be clarified in detail.

1.1 Background

The guarantee of nuclear safety is of uttermost significance in nuclear power plants because the release of radioactive materials into the environment could bring about irreversible and long-term damage to public health, such as Fukushima nuclear accident. In terms of light water reactors, if the accident such as the loss of coolant accident happens, the absence of coolant could lead to core damage, where the radioactive fission products could escape from the core and move to the pathway [1]. The components of fission products are rather complex, which are subject to fuel matrix and operation conditions [2]. Typically, the largest quantities of fission products consist of ^{133}Xe, ^{131}I, ^{132}Te, ^{133}I, ^{134}Cs, and ^{137}Cs [2]. In general, the steam and non-condensable gas (H_2, CO, CO_2, etc) mixture are generated during the core damage process, which servers the carrier medium to transport the radioactive material. To avoid the radioactive product from releasing into the main system, the water pool, namely the suppression pool in boiling water reactors or the secondary side of a stream generator in pressurized water reactors is utilized to enhance aerosol retention in the form of bubble scrubbing [3]. Aside from aerosol retention, the additional purpose of pool scrubbing is to condense the steam from the reactor's primary coolant system to restrict the containment pressure, where the hot gas could be cooled down to achieve the thermal equilibrium eventually inside the liquid pool. Due to its significance, pool scrubbing has already been identified as a high-priority nuclear safety research topic after several post-Fukushima activities [4].

To predict the decontamination factor (*DF*) under pool scrubbing conditions, several numerical codes were developed, such as SUPRA [5], BUSCA [6] and SPARC-90 [7]. In the SPARC-90 model, the overall processes of pool scrubbing could be divided into four zones, which are injection zone, transition zone, swarm zone and pool surface zone, respectively as shown in Fig. 1.1. In the injection zone, the non-condensable gas and steam with aerosol is injected into the liquid pool through a pipe, which results in the formation of a large globule. It should be mentioned that the formation of globule regime is subject to the inlet velocity, where the criterion is decided by the inlet Weber number as [8]

$$We_{\mathrm{inlet}} = \frac{\rho_{\mathrm{l}} D_{\mathrm{inelt}} U_{\mathrm{inelt}}^{2}}{\sigma} \tag{1.1}$$

The threshold of We_{inlet} for globule regime should be below 10^5, whereas the flow condition could be treated as jet regime with We_{inlet} above 10^5 [8]. Once the globule detaches the nozzle, the primary bubble will break up and disperse into small bubbles due to the instabilities at the bubble surface in the transition region. As the bubble coalescence rate is roughly equal to breakup rate, bubble swarm is established with a stable bubble size distribution approximately [7]. In the bubble swarm zone, the removal capability for radioactive aerosol particles is thought to be pronounced as indicated in the SPARC-90 model [7]. When bubble swarm comes to the pool surface region, the occurrence of bubble breakup will take place, which could also give rise to numerous micro-droplets in the atmosphere.

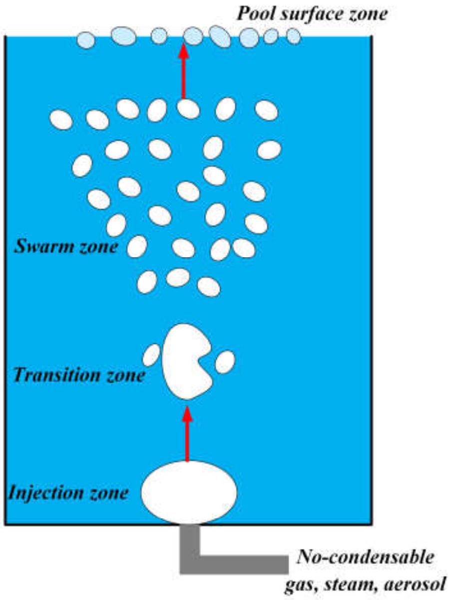

Fig. 1.1. Schematic of pool scrubbing process.

The present study is focused on the processes in the swarm zone. In the SPARC-90 model, the overall physical phenomena in the swarm zone are divided into two separate parts, related to single bubble and swarm bubble, respectively. As for the single bubble related phenomena, the prediction of different parameters is conducted including bubble size, bubble shape and rising velocity. The resolved bubble dynamics serves as the input information for the analysis of aerosol particle behavior inside the single bubble. The process of particle decontamination inside the rising bubble is considered by several mechanisms, such as inertial impaction, gravitational deposition, Brownian diffusion, and vapor condensation [7]. The schematic of the single bubble model is shown in Fig. 1.2. Correspondingly, the net local deposition velocity U_{net} accounting for the above effects could be written as

$$U_{\mathrm{net}} = U_{\mathrm{c}} + U_{\mathrm{v}} + U_{\mathrm{g}}\cos\beta + U_{\mathrm{B}} \tag{1.2}$$

Once the net deposition velocity is attained, the decontamination factor in the single bubble could be expressed as

$$DF = \exp\left(\frac{1}{\pi a^2 b}\int_0^{t_\mathrm{b}}\int_0^{A} U_\mathrm{n}\,\mathrm{d}A\mathrm{d}t\right) \tag{1.3}$$

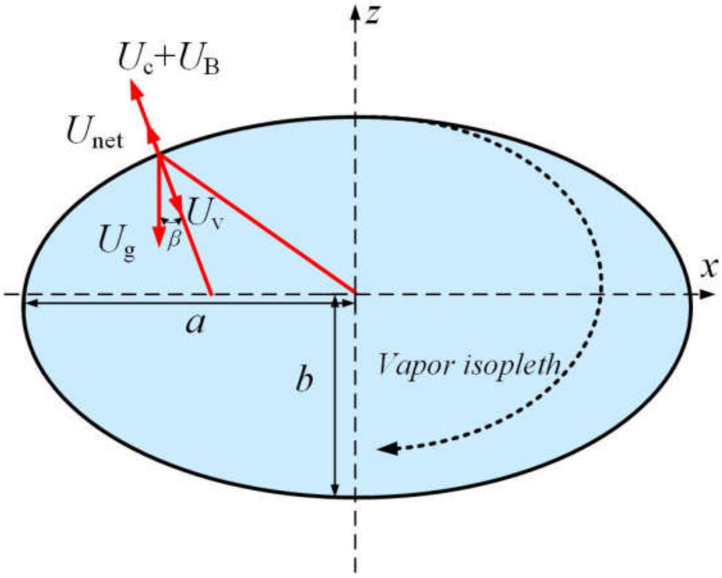

Fig. 1.2. Schematic of single bubble model in SPARC-90 [7].

However, a considerable deficiency may exist for the single bubble model [7] given that the bubble is assumed to be a constant bubble shape, such as the ellipsoidal shape. Regarding the air bubble rising in liquid water, the interfacial area may be time-dependent and vary dynamically following the bubble deformation [9-10]. As a key factor affecting mass transfer, the bubble interfacial area should be evaluated carefully rather than computing it simply with the ellipsoidal shape assumption. Furthermore, the oscillation of the gas-liquid interface of the bubbly flow contributes to the particle migration from the gas phase to the liquid phase in experimental observations [11], which also implies the limitation in the predefined shape assumption to reveal the real particle transport. Therefore, the full description of the bubble shape and its three-dimensional interfacial area is the indispensable premise to reveal the dependence of aerosol deposition on bubble dynamics, where the Computational Fluid Dynamics (CFD) method will be utilized as the crucial tool to fulfill this purpose.

Apart from that, another important aspect is related to aerosol residence time. It could be inferred that the decontamination factor in swarm zone is mainly determined by bubble residence time and aerosol residence time. As the name implies, residence time means the physical time where bubbles or aerosol particles stays in swarm zone for mass transfer. If bubble residence time is much larger than aerosol residence time, a satisfied decontamination could be guaranteed. Otherwise, the removal performance could be limited because of insufficient physical time with respect to mass transfer. To investigate aerosol residence time with a broad range of physical parameters in the swarm zone, the systematic analysis of influential factors to affect aerosol decontamination is indispensable, which is also one of main targets in this thesis. The CFD method is also employed to investigate the process of aerosol transport inside the gas bubble. In particular, particle behavior on the gas-liquid interface is especially considered in this thesis, which hasn't been paid enough attention in the previous studies hitherto. Regarding the aerosol size in real power plant accidents, the estimated particle size distribution injected into the scrubbing pool is from 0.01 to 2 μm [2]. A single micron particle impacting the gas-liquid interface may present two or three modes dependent on particle wettability and impact parameters according to experimental observations [12-13]. Specifically, the hydrophobic particles may sink across the interface, oscillate around the interface or bounce off from the interface [12], while hydrophilic particles may sink across or suspend on the interface [13]. However, in previous theoretical, experimental, and numerical studies, few works consider this point and the effect of particle interfacial behavior on particle removal is generally ignored. As a consequence, Eq. (1.3) in SPARC-90 [7] only characterizes the transport process of the different particles toward the bubble boundary, while the feature of the interaction between the particle and the bubble surface is not manifested yet. Provided that the local particle transport through the gas-liquid interface is dominant by the impact conditions inside each bubble, the global mass transfer rate of the bubbly flow under pool scrubbing conditions is also affected significantly by the particle interfacial behavior, which hasn't been illuminated either qualitatively or quantitatively to date.

As an improvement of previous studies, the interfacial process of micron particles on the bubble surface will also be analyzed in this thesis and an interfacial penetration model will be implemented into the CFD solver to include the effect of particle interfacial behavior on aerosol decontamination. After the validation of the developed solver, it is applied to analyze the aerosol residence time. Since there is no previous investigation about aerosol residence-time distribution analysis, the basic concepts will be introduced at first, where the characteristics will be analyzed accordingly. At the end, a study is performed to investigate aerosol mean residence time.

The impetus of this work is motivated by the improvement of modeling of decontamination factor in SPARC-90 [7]. To fully describe the three-dimensional bubble interfacial area and aerosol residence time, the CFD method is employed based on open-source software OpenFoam-7 [14]. To capture bubble shape and three-dimensional interfacial area, Volume of Fluid (VOF) method is applied. Regarding the intermediate air bubbles from 1.3 to 6 mm rising in water [15], the bubbles are accompanied by unregular momentary shape and time-dependent bubble interfacial area. In this context, the application of the VOF method is appropriate because the VOF method has been proven to be capable to deal with complex topology changes [16-17]. The evolution of particle motion is governed by Newton's second law in the Lagrangian frame [18-19]. Since the solving of the Newton‘s equations requires the flow information of the carrying phase, the VOF method will be performed at first in each time step, and subsequently, the VOF results will be passed to the governing equations in the Lagrangian frame to track the particle motion. Therefore, the combination of the VOF method with the Lagrangian Particle Tracking (LPT) method in the OpenFoam environment will be conducted for the above two purposes.

1.2 Objectives of this study

In the present study, the primary aims are to investigate bubble interfacial area and aerosol residence time under different conditions comprehensively, which serves as a crucial step for the improvement of aerosol particle decontamination model in SPARC-90. With the aid of CFD methods [20-21], transient bubble interfacial area is tracked. Correlation of terminal interfacial area is developed based on the numerical results covering various conditions. As for the aerosol decontamination process, an interfacial penetration model coupling with the VOF-LPT method is developed to include the effect of particle interfacial behavior on aerosol decontamination. Given that particle retention is affected by both the bubble dynamics and the particle interfacial behavior, bubble dynamics is extensively investigated individually at first. Then, the implication of changeful bubble dynamics and aerosol properties in aerosol decontamination process will be analyzed as a whole. After the parametric study of the influential factors is performed, the key parameters on residence-time distribution inside the rising bubble will be summarized and the dependency of aerosol mean residence time on the key parameters will be checked. The entire study could be divided into five subtasks.

(I) Analysis of single bubble dynamics in the rising process

The three-dimensional bubble interfacial area in simulation is validated by the experimental data [22] of a single bubble rising in viscous fluid given that the bubble in this context could keep a stable shape and a rectilinear path. Afterward, the transient evolution in long-term bubble dynamics is investigated and the velocity-shape dependence is particularly analyzed.

(II) Development of correlation for bubble terminal interfacial area

According to the previous phase plots [23-24], the Eötvös and Galilei numbers are selected as the key dimensionless numbers to determine the bubble terminal interfacial area. Through the extensive simulations over a wide parameter range, an empirical correlation is proposed based on the numerical dataset. Meanwhile, the accompanied bubble hydrodynamics phenomena due to the variation in physical properties will also be explored.

(III) Development of the interfacial penetration model

To include the effect of particle interfacial behavior on aerosol decontamination, a new criterion based on particle Weber number is derived in light of the dimensionless analysis of the particle momentum equation. The new interfacial penetration model is coupled with the VOF-LPT solver, which will be validated against the single bubble decontamination experiment data [25].

(IV) Analysis of aerosol transport behavior inside the rising bubble

Owing to the presence of particle interfacial behavior, the effect of bubble dynamics and aerosol properties on the particle transport process will be divided by the process of particles approaching and impacting the interface, respectively. Specifically, the probability of particle-interface encounter, aerosol deposition velocity and aerosol removal distribution will be investigated in detail.

(V) Investigation of aerosol residence time

Based on the results in subtask IV, key influential factors on aerosol residence time will be evaluated, whereby the analysis of aerosol residence time could be performed. Since residence-time distribution analysis is introduced into aerosol decontamination process to account for temporal removal behavior at first, the characteristics will be checked in detail. Then, the main influential factors will be analyzed to account for aerosol mean residence time in the swarm zone under pool scrubbing conditions.

As a logic diagram of above five subtasks, the description of task classification is exhibited in Fig. 1.3. The emphasized subjects of this thesis are bubble interfacial area and aerosol residence time, where validation, qualitative analysis and quantitative fitting are carried out in sequence. The main contributions of this work will be an interfacial penetration model and a comprehensive correlation of bubble terminal interfacial area from the quantitative aspect. Apart from that, since the current works related to the particle interfacial behavior are mainly restricted to a single particle hitting the stagnant gas-liquid interface, the utilization of the available knowledge of the single particle toward multi-particles inside the rising bubble is also an important application under the industrial background. The revelation of the dependence of bubble dynamics and particle properties on aerosol decontamination will also benefit the fundamental comprehension of the pool scrubbing process form the qualitative viewpoints.

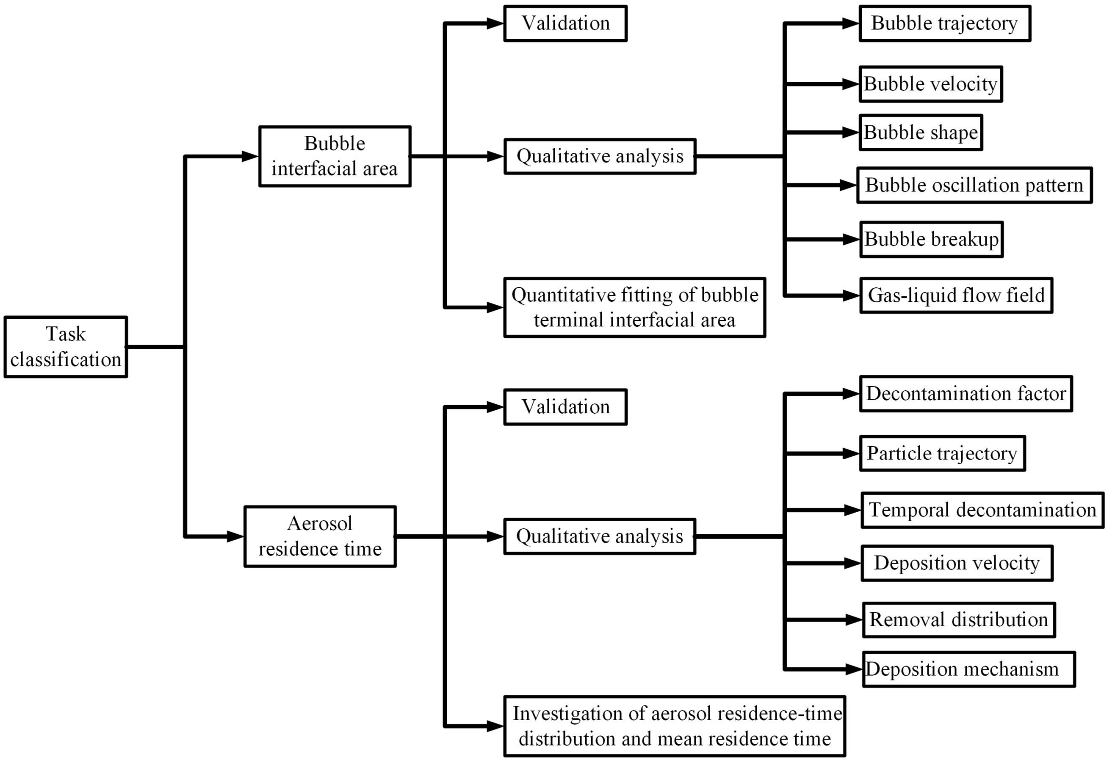

Fig. 1.3. Description of task classifications.

2 State of the Art

In this chapter, the aerosol decontamination process in experimental works is reviewed, where the dependency of aerosol decontamination on physical operating parameters and particle characteristics is included in detail. Then, the numerical methods for calculating the global decontamination factor and local decontamination factor are examined. After that, bubble dynamics including bubble shape, bubble interfacial area and so on is included, where the method of calculating bubble interfacial area is particularly illustrated due to its importance. Finally, particle deposition mechanism and particle interfacial behavior are revisited, where the present findings in this part will serve as the stepstone for the development of the interfacial penetration model in this thesis.

2.1 Experimental investigation of pool scrubbing

The aerosol decontamination process in the liquid pool can be influenced by various factors. However, a comprehensive summary of previous investigations in this area is currently lacking. In this section, we aim to address the primary effects from two perspectives: the physical operating parameters and particle characteristics. By concluding qualitative relationships in previous works, we aim to enhance the understanding of these effects.

2.1.1 Physical operating conditions

The significance of physical operating conditions in influencing the retention capacity of bubbles in the liquid pool is self-evident. Numerous studies [26-32] have sought to summarize the influence of various factors that affect the decontamination factor, such as inlet gas flow rate, initial injection direction, steam fraction, pool temperature, and pool height. Several experimental investigations [26-28] have reported that an increase in inlet gas flow rate leads to an increased decontamination factor, while Farhat et al. [29] have reported the opposite relationship. Farhat et al. [29] attribute this discrepancy to the influence of hydrodynamic regimes on flow morphology. As mentioned earlier, the inlet gas flow rate can be characterized by the inlet Weber number, which determines the transition from the globule regime to the jet regime as the flow rate increases [8]. Based on the summarized results by Farhat et al. [29], an increasing Weber number in the globule regime has an adverse impact on the decontamination factor, whereas a positive dependency is observed in the jet regime. Particularly, given that different flow regimes bring about the difference in aerosol removal mechanism, a minimum decontamination factor has been found in the transition from the globule to jet regimes in their work [29].

The initial injection direction of bubbles depends on the configuration of the nozzle. When bubbles are injected horizontally, they initially move horizontally and then rise vertically, while vertically downward injected bubbles initially travel downward and then rise due to the buoyancy force [30]. The disparity in gas injection directions impacts the relative velocity between the gas and liquid, thereby influencing the residence time of the bubbles and subsequently affecting aerosol removal. As stated in Ref. [30], the influence of gas injection direction on aerosol decontamination is particularly pronounced when low gas flow rates is used.

In terms of the inlet gas component, the presence of steam not only alters the overall bubble size distribution by atomizing larger bubbles but also facilitates the phase change process, enabling the transfer of airborne aerosols from the gas phase to the liquid phase, as indicated by Eq. (1.2). Experimental observations [26] have confirmed that an increasing steam fraction results in an increased decontamination factor. The increase in pool temperature raises concerns regarding the retention capacity of pool scrubbing. Dehbi et al. [31] reported a significant decrease in the decontamination factor as the pool temperature approached the saturation temperature. At saturation vapor pressure, the ratio of steam condensation upon contact with liquid water substantially diminishes, leading to a lower aerosol decontamination factor. Moreover, a similar dependence of the decontamination factor on pool temperature is observed in the absence of steam condensation for non-condensable gas as reported by Li et al. [32]. This also indicates that not only the influence of steam condensation but also the variation in bubble dynamics during the temperature-rise process may contribute to the degradation of pool decontamination efficiency. It is understandable that an increase in pool height results in improved aerosol decontamination performance, as it increases the bubble residence time and extends the physical time for aerosol transport. In fact, an exponential trend of removal with respect to pool height is universally observed in particle collection experiments [26, 33], which serves as the fundamental basis for Eq. (1.3) as presented previously.

2.1.2 Particle characteristics

In addition to the physical operating conditions, the impact of particle characteristics on overall scrubbing efficiency should be emphasized. Among the various parameters of particle properties, particle size has received significant attention in previous studies. Generally, aerosols with sizes larger than 1 μm have been shown to be effectively decontaminated during the pool scrubbing process [34]. Since the inlet aerosol typically exhibits a size distribution, larger aerosols tend to be collected during pool scrubbing, while smaller aerosols may escape from the liquid pool, posing a risk to public health. Consequently, the investigation of ultrafine aerosols is of great interest in pool scrubbing due to the high potential for residual exposure to the environment. As for particle density, its influence is considered by the density ratio between the particle phase and gas phase. As particle density increases, both the removal contributions from inertial impaction and gravity sedimentation improve due to increased particle inertia, as demonstrated in previous studies [35].

The solubility of particles plays a crucial role as it can alter the interface properties. Fujiwara et al. [36] noted that a rising bubble containing soluble aerosols exhibits a rounder shape and lower terminal velocity compared to a clean bubble or a bubble with insoluble aerosols, attributed to the Marangoni effect. In this case, the solubility of aerosols is understood to have a similar effect to surfactants, namely reducing the gas-liquid surface tension coefficients [37]. However, if soluble aerosols on the bubble surface behave similarly to surfactants, they may potentially impair the performance of pool scrubbing, as observed in particle collection experiments [38]. Despite the fact that the addition of surfactants can shift the bubble size distribution towards smaller sizes, Koch et al. [38] reported that surfactants lead to an increasingly rigid interface, ultimately causing the complete cessation of bubble internal circulation, which significantly hinders aerosol scavenging.

Apart from interface properties, another important aspect linked to aerosol solubility is hygroscopic growth [7]. When the aerosol-laden bubbles pass through the liquid pool, the relative humidity inside the bubble may increase substantially, which may induce the microstructural rearrangements of the soluble aerosol followed by a growth size [39]. Since hygroscopic growth can lead to deviations in both the aerosol size distribution at the outlet and the size-dependent removal efficiency, comprehensive investigations addressing this specific issue can be found in the studies [39-40].

In existing pool scrubbing models, the potential influence of aerosol concentration is not included, and the decontamination factor is thought to be independent of aerosol concentration [41]. However, Sun et al. [42] held the opposite opinion and explored the dependence of the decontamination factor on aerosol concentration. They reported that the dependence turns out to be obvious in the context of the water submergence higher than 1.6 m with the aerosol concentration less than $1\times10^{11}/\mathrm{m}^3$. Similarly, Xu et al. [43] also found that the difference in decontamination factor induced by the aerosol concentration is not significant when the water height is less than 1 m. Based on the feedback from the experimental works, the preliminary numerical modeling is carried out by Kim et al. [44]. They postulated that the effect of aerosol concentration embodies in a manner similar to that of surfactants to contaminate bubble interface, whereby they defined a so-called aerosol concentration factor to modify the previous theoretical model [45]. Since the investigation of aerosol concentration remains rudimentary at present, whether the postulation [44] could reveal the mechanism in the physical reality should be further checked in the future.

2.1.3 A brief summary

To sum up, it has been observed that both physical operating conditions and particle characteristics can have a significant impact on the aerosol decontamination factor, as indicated by the above experimental investigations. While experimental works can uncover the macroscopic dependence of the aerosol decontamination factor on various factors, the microscopic transport of aerosols through rising bubbles is rarely taken into account in previous experiments, which is the main focus of this thesis. Additionally, since several factors, such as bubble rising velocity and particle size, have been proven to be important for aerosol decontamination, these factors will be given special consideration in the further investigation conducted in this thesis.

2.2 Numerical calculation of decontamination factor

In this section, the calculation of overall decontamination factor in current pool scrubbing codes will be introduced. Then, the numerical methods for the calculation of decontamination factor inside a single bubble will also be included for better understanding.

2.2.1 Overall decontamination factor calculation

Based on the available experimental database, several analytical models have been developed for the calculation of the overall decontamination factor in the liquid pool, such as SUPRA [5], BUSCA [6], and SPARC-90 [7]. However, these models tend to show a significant deviation in the calculated decontamination factor compared to the measured values, which indicates that some important retention processes in the liquid pool are not adequately captured by the existing pool scrubbing codes [4].

In addition to the above-mentioned pool scrubbing codes, Abe et al. [11] conducted experimental work to validate the physical model used in the system code MELCOR. They reported good agreement between the measured average gas velocity at high submergence and the calculated results by MELCOR. However, there were relatively large deviations observed in bubble rising velocity and aspect ratio compared to empirical correlations in MELCOR, which may be attributed to bubble deformation under various experimental conditions. Fujiwara et al. [37] evaluated the decontamination factor for a single bubble and emphasized the influence of aerosol properties on bubble hydrodynamics. They found that the unconsidered aerosol solubility properties in MELCOR could lead to significant deviations in the decontamination factor between experimental and calculated results, as bubble shape and rising velocity are affected by aerosol solubility. Furthermore, He et al. [46] proposed a new analytical model framework and validated their model using experimental data. Through comparison with other pool scrubbing codes, their developed code demonstrated equivalent predictive ability, aligning well with benchmark data.

2.2.2 Local decontamination factor calculation

Above pool scrubbing codes generally calculate aerosol decontamination factor with the aid of empirical correlations from experimental sources, where the information on aerosol motion inside rising bubbles is not available. As mentioned before, the LPT method could be used to track aerosol motion, which is of particular interest under the circumstance of a single rising bubble. In terms of previous numerical works [47-50], since the application of LPT method requires information on bubble morphology and internal flow field, a spherical bubble with Hill's vortex flow [51] is usually presupposed in advance as exhibited in Fig. 2.1. The Vector *n* is the unit outward-pointing normal vector of the streamline, which could be given as [50]

$$n(\boldsymbol{x}) = \frac{-\nabla\psi(\boldsymbol{x})}{\parallel \nabla\psi(\boldsymbol{x}) \parallel} \tag{2.1}$$

With respect to the Hill's vortex, the so-called Stokes stream function could be defined by the cylindrical coordinates (r, φ, z) as [50]

$$\psi(r, \varphi, z) = -\frac{3}{4} U_{\mathrm{b}} R_{\mathrm{b}}^{-2} r^2 \left(R_{\mathrm{b}}^2 - r^2 - z^2\right), \qquad (r^2 + z^2 \leq R_{\mathrm{b}}^2) \tag{2.2}$$

The fluid velocity inside the bubble could be derived from the stream function as [50]

$$U(r,\varphi,z)=\left(-\frac{1}{r}\frac{\partial\psi}{\partial z},0,\frac{1}{r}\frac{\partial\psi}{\partial r}\right) \tag{2.3}$$

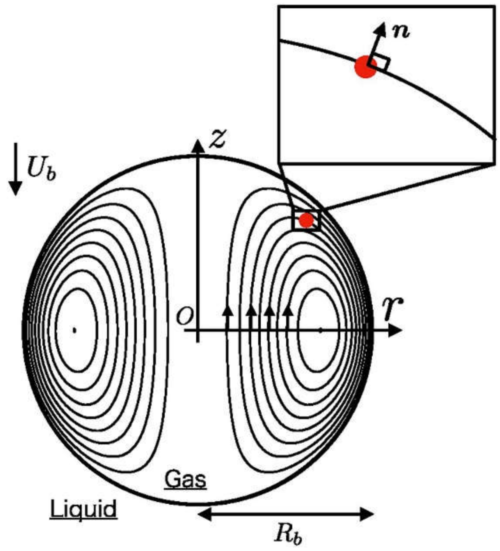

Fig. 2.1. Representation of Hill's spherical vortex [50].

In the context of the steady spherical vortex model described in Eq. (2.2) and (2.3), internal particles generally follow the internal gas circulation and are assumed to be removed once particles impact the bubble surface in the previous studies [47-50]. Laker et al. [47] conducted numerical simulations using these setups and reported that the strength of bubble internal circulation plays a crucial role in influencing aerosol transport mechanisms. They also indicated that the presence of surface active contaminants could have a substantial impact on bubble internal circulation, leading to a deterioration of the decontamination factor. This numerical finding was further supported by particle collection experiments conducted by Koch et al. [38]. Motegi et al. [48] investigated the transport process of 0.1 and 1 μm particles and stressed that the nonuniform aerosol concentration due to increased particle size could affect the distribution of aerosol decontamination on the bubble surface substantially. Additionally, Sun et al. [49] changed the predefined bubble shape from spherical to ellipsoidal shape and described the internal flow by a modified Hill vortex flow. They found that when the equivalent size between spherical and ellipsoidal bubbles are the same, the decontamination factor of ellipsoidal bubble is higher than that of spherical bubble, which also implies the significant effect of bubble shape on aerosol decontamination factor.

However, neither spherical nor ellipsoidal shape could be a comprehensive description for bubbles in the presence of bubble size distribution under pool scrubbing conditions according to the experimental observations [11] because bubble size could vary more than ten millimeters in the liquid pool. In this context, bubble shape could be fully irregular and oscillating, which disobeys the constant shape assumption dramatically. To address this limitation, researchers have turned to the CFD method, which enables the description of time-dependent bubble shape. By coupling the CFD method with the LPT method, a more accurate representation of the aerosol transport process through rising bubbles can be achieved. This combination of techniques provides a comprehensive approach to studying the complex dynamics of bubbles and their impact on aerosol decontamination.

Akbar et al. [52] conducted a study using the VOF-LPT approach and compared their results with those obtained from the Hill vortex flow assumption. They reported that as the bubble rises and undergoes shape changes, the internal circulation pattern becomes stronger and more complex, resulting in aerosol decontamination factors that differ from those predicted by the presupposed internal flow assumption. Building upon the work of Akbar et al. [52], Mirzaee et al. [53] investigated particle collection in the air sampling process and discovered that the oscillation of the bubble interface at the inlet significantly contributes to particle collection. Pan et al. [54] explore the effect of bubble size on aerosol decontamination and indicated that bubble deformation could affect aerosol decontamination dramatically through the variation in internal flow pattern. In particular, a new method to calculate aerosol decontamination is proposed by Fujiwara et al. [25]. They estimated the aerosol velocity by the local gas velocity on the basis of small stokes number of particles, where the flow field is resolved by the level-set method. Through the comparison with experimental data, their numerical model is proven to be feasible in given conditions. In terms of the above works, the method classification is summarized in Fig. 2.2.

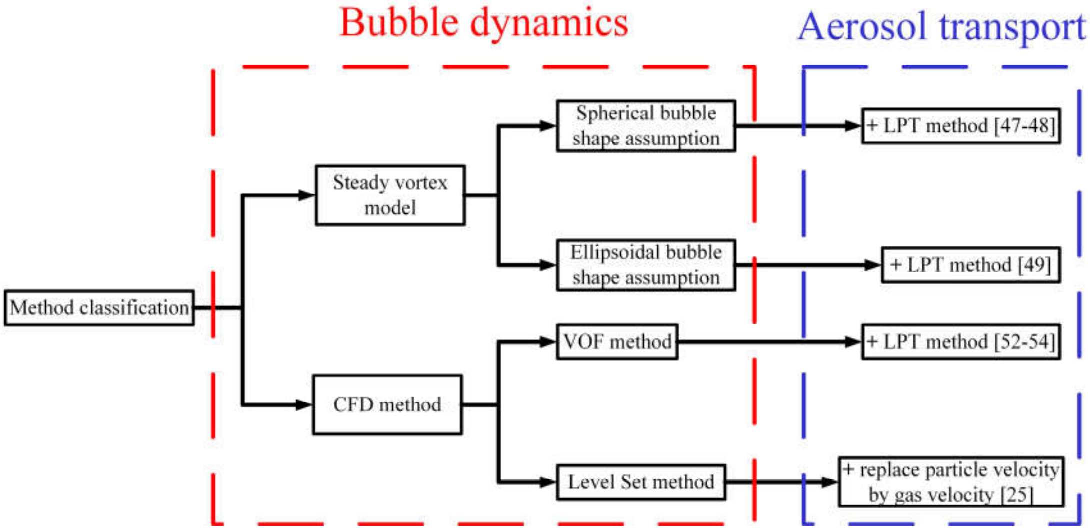

Fig. 2.2. Method classification in calculating local aerosol decontamination.

2.2.3 A brief summary

Previous numerical calculations about aerosol decontamination factor are reviewed. In general, the overall aerosol decontamination factor of the whole pool scrubbing process could be obtained with the help of stand-alone pool scrubbing codes [5-7], where the information on local aerosol motion is missing. As a supplement, the steady vortex model or CFD methods [47, 52] could be employed to provide the detail on aerosol transport behavior inside rising bubbles, which benefit the understanding of aerosol decontamination mechanisms. Following the previous manner [52-54], the VOF-LPT method will be built in this thesis to investigate the aerosol decontamination process by an isolated bubble.

2.3 Bubble shape and interfacial area

2.3.1 Single bubble shape

According to the above literature review, it is evident that bubble dynamics significantly influence aerosol transport, particularly in terms of bubble shape. The effects of bubble shape on aerosol decontamination can be understood from two perspectives, which are the interfacial forces acting on the rising bubble and the transient shape oscillation on particle transport, respectively.

In the case of a single air bubble rising in water, the terminal shape of the bubble changes with its size, as observed in experiments [55]. For sufficiently small bubbles, the dominant surface tension effect maintains a spherical terminal shape. As the bubble size increases, surface wobbling occurs, leading to deformations such as oblate ellipsoidal shapes, followed by the appearance of spherical-cap or ellipsoidal-cap terminal shapes [55]. The typical evolution of bubble shape with respect to different bubble size is illustrated in 2.3.

With increased bubble deformation, the cross-sectional area of the bubble expands, leading to an increase in pressure drag from the surrounding fluid acting on the bubble surface [56]. Compared to a spherical bubble, the presence of a deformed bubble contour results in an increase in friction drag around the deformed bubble surface [57]. Furthermore, the size of lift force and virtual mass force are also influenced by bubble shape, as indicated in previous studies [58-59].

These changes in interfacial forces due to bubble shape alterations have consequential effects on critical factors such as bubble residence time, bubble motion, and internal circulation patterns. These variations, in turn, exert a significant impact on the process of mass transfer.

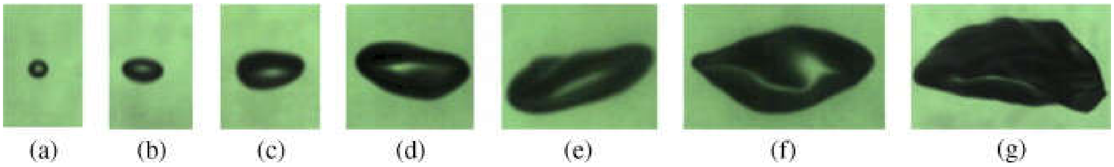

Fig. 2.3. Typical bubble shape evolution versus bubble size from experimental observations [55] at water temperature equal to 29°C.

Besides the terminal bubble shape, the transient bubble shape oscillation also affects internal particle motion significantly. Due to the wobbling nature of air bubbles rising in water, the intermediate bubbles from 1.3 to 6 mm may present a slight or considerable shape oscillation dependent on the size and physical conditions in the rising process [60]. Abe et al. [11] found that the oscillation in the gas-liquid interface benefits the shift of particles from the gas phase to the liquid phase. The typical particle removal process as a result of the interface oscillation recorded by the high-speed camera is shown in Fig. 2.4.

Moreover, the consistent standpoint about the oscillating interface on particle removal can be found in the work of Yan et al. [61]. They considered the effect of the fluctuating gas-liquid interface and built a mathematical model under the jet condition. The results indicated that the influence of the oscillating interface on aerosol removal is dominant in the case of low inlet velocity. Given that bubble shape oscillation may affect the encounter between the particle and the gas-liquid interface significantly, the effect of transient bubble shape and its oscillation on particle transport will be further examined in this work later.

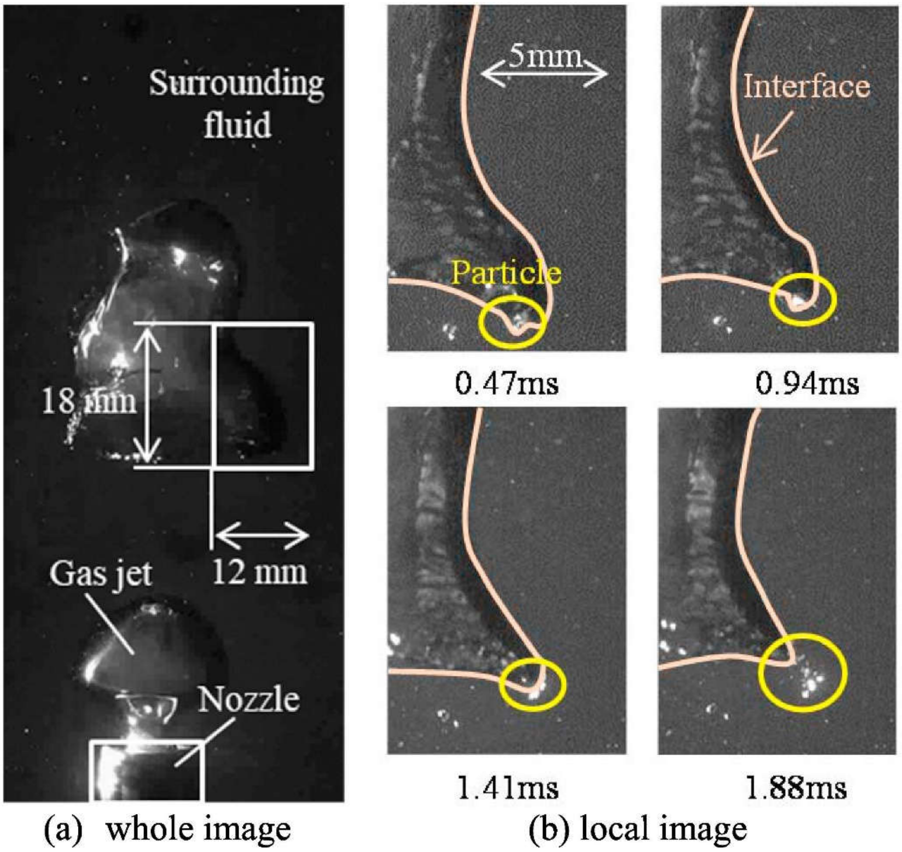

Fig. 2.4. Visualization of aerosol transport from the experimental work of Abe et al. [11].

2.3.2 Three-dimensional interfacial area

Among all bubble dynamics, the three-dimensional bubble interfacial area is of main interest in this work because it is one of the key factors to predict the mass transfer rate inside the liquid pool as revealed in Eq. (1.3). In physical conditions, the large three-dimensional interfacial area inside the liquid pool could present the enhanced capacity of particle retention generally because of the high probability of particles hitting the gas-liquid interface. Due to its importance, the crucial bubble parameter, namely the three-dimensional bubble interfacial area will be carefully addressed in this part.

The measurement of interfacial area for a single bubble generally requires the three-dimensional bubble shape reconstruction [62]. A commonly used approach for developing a bubble space model involves capturing bubble images using a high-speed camera. By employing shape reconstruction algorithms and making certain assumptions, two-dimensional projected parameters from the images can be converted into three-dimensional space parameters [62]. However, obtaining a complete description of the three-dimensional bubble shape through this model can lead to significant data processing requirements. Therefore, it may be impractical to apply this method for tracking the transient interfacial area as a function of physical time or the terminal interfacial area as a function of bubble size.

As an alternative, Legendre et al. [22] adopt a simplified method to measure the bubble interfacial area in the high-viscosity system based on Pappus's first theorem. Due to the large liquid viscosity, the bubbles rise in a straight trajectory and meet with the axisymmetric shape assumption. Under this circumstance, the computing schematic of the bubble interfacial area is presented as Fig. 2.5, where s stands for bubble arc length, m is the centroid of the arch and l is the perpendicular distance from m to the central axis. Based on Pappus's first theorem and the axisymmetric shape assumption, the three-dimensional bubble surface area can be thought to be generated by rotating the arc s around the central axis for a full circle, whereby the measured bubble surface area in the experiment [22] could be expressed as

$$A = 2\pi \cdot s \cdot l \tag{2.4}$$

Apart from the bubble rising in the viscous liquid, the same methodology has also been applied in the measurement of bubble interfacial area for the air-water system by Wen et al. [63]. They measured the temporal evolution of bubble interfacial area versus time and found that the contribution from increasing bubble size results in a large growth ratio in bubble surface area. However, it should be mentioned that an air bubble rising in water could present a wobbling bubble as exhibited in Fig. 2.3, whether the axisymmetric shape assumption is viable for different-sized bubbles should also be checked further.

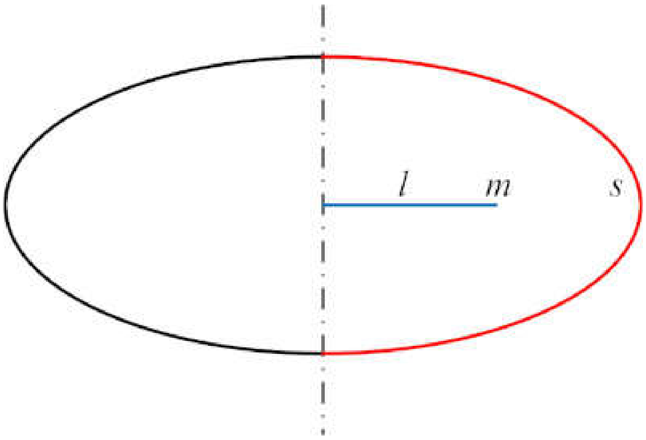

Fig. 2.5. Computing schematic of bubble interfacial area in the experiment [22].

It is important to note that the investigation of the three-dimensional interfacial area for a single bubble in the aforementioned experimental works has certain limitations when considering the water properties under pool scrubbing conditions. In pool scrubbing conditions, both the gas and liquid phases undergo significant changes in physical properties due to variations in pressure and temperature. Consequently, the bubble presents a highly wobbling shape with complex deformations, which greatly deviate from the predefined shape assumption in experimental works.

Therefore, employing the CFD method to calculate the transient and terminal bubble interfacial area under different physical properties appears to be a promising approach to account for the highly irregular bubble shape across a wide range of physical properties.

In simulations, the calculation of bubble interfacial area could be performed in two ways, such as the size of gas volume fraction and the area of an isoface. The application of gas volume fraction to predict gas-liquid interfacial area is generally applied in the cases of heat or mass transfer and bubble interfacial area in simulation could be approached by [64]

$$A = \int \left|\nabla \alpha_{\mathrm{g}}\right| \mathrm{d}V = \int \sqrt{\left(\frac{\partial \alpha_{\mathrm{g}}}{\partial x}\right)^2 + \left(\frac{\partial \alpha_{\mathrm{g}}}{\partial y}\right)^2 + \left(\frac{\partial \alpha_{\mathrm{g}}}{\partial z}\right)^2}\, \mathrm{d}V \tag{2.5}$$

In particular, this method may only be feasible to predict the interfacial area of the global domain and not locally. Furthermore, the adjacent cells close to the interfacial cells may also be taken into account because the gradient is not rigorous equal to zero in these cells, which may lead to the overestimation of bubble interfacial area significantly [65]. Another method is to calculate the bubble interfacial area by the size of an isoface [20]. The isoface is formed by the cutting of the interfacial cells by the elementary triangles and all triangles will connect to form an isoface, which could be treated as a consistently closed multi-face geometry. The size of the bubble interfacial area in simulation could also be calculated as [20]

$$A = \sum_{i=1}^{N} A_i \tag{2.6}$$

Apparently, the calculation of bubble interfacial area by the isoface is much more precise than that by gas volume fraction because the bubble interfacial area is well represented by the surface area of the isoface. Therefore, the bubble interfacial area in this work is calculated by the size of the isoface.

Previous numerical studies, both directly and indirectly, have considered the importance of bubble interfacial area [66-67]. Lalanne et al. [66] specifically investigated the interfacial area during bubble shape oscillation and calculated bubble surface energy based on its size. They observed an antiphase relationship between bubble surface energy and kinetic energy in slowly rising bubbles. Chen et al. [67] examined the bubble detachment area under rolling oscillation conditions and highlighted the significant influence of surrounding water on this area. However, in these CFD works, the validation of three-dimensional bubble interfacial area in simulations has generally been overlooked. Therefore, it is crucial to assess the credibility of this key bubble hydrodynamics based on available experimental data. Moreover, several influential factors such as the interface sharpening scheme, mesh resolution, and the threshold of gas volume fraction for the isoface remain unexplored. As the quantitative evaluation of bubble interfacial area is essential for developing a reliable interfacial area correlation under pool scrubbing conditions, the relevant calibration and evaluation process of bubble interfacial area is summarized in Section 4.1.

2.3.3 A brief summary

As mentioned earlier, both bubble shape and interfacial area play significant roles in aerosol decontamination. Under pool scrubbing conditions, bubble shape can exhibit wobbling and irregular characteristics, which should be carefully considered. Previous studies have examined the three-dimensional interfacial area of single rising bubbles from both experimental and numerical perspectives. Experimental approaches involve developing bubble space models to determine the interfacial area of individual bubbles. One simplified method proposed by Legendre et al. [22] offers a way to calculate bubble interfacial area, but it has not been widely adopted despite its importance. On the other hand, numerical simulations estimate the interfacial area based on gas volume fraction or isoface, yet the accuracy of these numerical methods requires validation through experimental data. In summary, the following key points can be drawn from the literatures as

(1) Bubble shape has a significant impact on both bubble dynamics and aerosol decontamination, primarily through interfacial forces and the oscillatory interface. The change in terminal bubble shape can alter interfacial forces, which in turn affect bubble residence time, motion, and internal circulation patterns, ultimately influencing aerosol decontamination. Furthermore, the oscillatory interface is confirmed to benefit aerosol transport in both experimental and numerical findings [11, 53], whose effect has been considered in the process of mathematical modeling in the numerical work [61].

(2) In experimental works, obtaining the three-dimensional interfacial area of a single bubble is achievable through the development of bubble space models. However, due to the extensive data processing requirements, temporal and terminal information regarding the bubble interfacial area is often lacking. As an alternative approach, the interfacial area of a bubble can be measured using Pappus's first theorem, assuming the bubble shape conforms to the axisymmetric shape assumption [22]. This simplified method has also been employed in the analysis of air-water systems by Wen et al. [63]. However, the validity of the axisymmetric shape assumption should be scrutinized for bubbles of various sizes, given their inherent wobbling nature.

(3) In numerical studies, the calculation of bubble interfacial area can be performed using either the gas volume fraction or the isoface size. The calculation based on gas volume fraction is applicable to the entire domain but lacks local accuracy, as noted in a previous study [65]. This method is typically employed in cases involving heat or mass transfer. On the other hand, the isoface approach represents the bubble morphology through a multi-face geometry, providing a more precise representation of the bubble surface. Therefore, in this work, the isoface method will be utilized to calculate the bubble interfacial area, capturing the bubble surface with higher accuracy.

2.4 Particle deposition on gas-liquid interface

2.4.1 Particle deposition mechanism

In terms of particle deposition mechanisms, the first theoretical model including bubble dynamics to predict particle transport efficiency is developed by Fuchs [45]. They assumed that the total absorption coefficient of particles by the surrounding liquid could be divided by three mechanisms independently, which are inertial impaction, gravitational deposition, and Brownian diffusion. In this context, the differential equation of particle transport inside rising bubbles can be expressed as [45]

$$\frac{\mathrm{d}C_{\mathrm{p}}}{\mathrm{d}h} = -k \cdot C_{\mathrm{p}} \tag{2.7}$$

After the integration, Eq. (2.7) can be rewritten as

$$C_{\mathrm{p}} = C_{\mathrm{p,0}} \cdot e^{-kh} \tag{2.8}$$

In this context, the total particle collection efficiency η_{total} can be expressed as

$$\eta_{\mathrm{total}} = 1 - \frac{C_{\mathrm{p}}}{C_{\mathrm{p,0}}} = 1 - e^{-kh} \tag{2.9}$$

Based on Eq. (2.9), the large absorption coefficients or bubble rising height could lead to a high particle deposition efficiency. To disintegrate the total absorption coefficients, each absorption coefficient including the effects of inertial impaction, gravitational deposition, and Brownian diffusion can be expressed separately as [45]

$$k_{\mathrm{i}} = \frac{9U_{\mathrm{b}}\tau}{2R_{\mathrm{b}}^{2}} \tag{2.10}$$

$$k_{\mathrm{g}} = \frac{3g\tau}{4U_{\mathrm{b}}R_{\mathrm{b}}} \tag{2.11}$$

$$k_{\mathrm{D}} = 1.8(\frac{D_{\mathrm{B}}}{U_{\mathrm{b}}R_{\mathrm{b}}^{3}})^{0.5} \tag{2.12}$$

According to Eq. (2.10) - (2.12), it can be got that the increase in bubble rising velocity improves the effect of inertial impaction but deteriorates the effect of gravitational deposition, and Brownian diffusion, whereas the increase in bubble size negatively impacts all these effects. The analysis suggests that the effect of bubble rising velocity on particle transport is subject to the physical conditions, while the influence of bubble size is monotonous. It should be mentioned that the increase in bubble rising velocity could bring about the enhancement in internal flow field, but bubble residence time in the liquid pool could also be reduced accordingly. In this case, whether the increase in bubble rising velocity could contribute to aerosol decontamination or not is still subject to the competitive effect as indicated by Li et al. [32]. Regarding the influence of bubble size, small bubbles are confirmed to improve the pool scrubbing effect in the experimental observation [68]. Given that the distance between internal particles and the gas-liquid interface is shortened if the bubble size decreases, the probability of the particle collision on the interface is increased and the particle collection rate is improved thereby [33]. Moreover, the dependence of particle transport on bubble size has been applied in the system design, such as the containment-filtered venting system [69].

On the basis of Fuch's model, the theoretical calculation could be carried out as the explicit expression of bubble rising velocity is provided. Pich et al. [70] chose bubble rising velocity as a function of bubble volume, which could be written as [71]

$$U_\mathrm{b} = 2.4 \cdot {V_\mathrm{b}}^{1/6} \tag{2.13}$$

In terms of particle relaxation time and particle diffusion coefficient, these correlations could be expressed as [70]

$$\tau = \frac{\rho_\mathrm{p} d_\mathrm{p}^2}{18\mu_\mathrm{g}} \tag{2.14}$$

$$D_\mathrm{B} = \frac{k_\mathrm{B} T}{3\pi\mu_\mathrm{g} d_\mathrm{p}} \tag{2.15}$$

With a combination of Eq. (2.7) - (2.15), a typical case of theoretical calculation could be presented as shown in Fig. 2.6. According to the theoretical calculation results, when aerosol size is below 0.1 μm, the Brownian diffusion could dominate aerosol decontamination, whereas the effect of inertia impaction is predominant progressively with aerosol size larger than 1 μm. As aerosol size is between 0.1 and 1 μm, all removal mechanisms could be limited, which results in a small particle deposition efficiency within this range. However, radioactive particles with the size between 0.1 and 1 μm have shown a high probability to escape from the liquid pool as indicated by Gupta et al. [4], which requires further examination of the corresponding deposition mechanisms comprehensively. Furthermore, for intermediate-sized bubbles from 1.3 to 6 mm, bubble dynamics could be attributed to the surface tension force dominant regime [60]. In physical occasions, the gas-liquid surface tension coefficients may experience significant change as a result of changing temperature. Although surface tension could affect bubble dynamics substantially, the accompanied effect on particle deposition mechanism is not embodied in the theoretical model, which will be further analyzed in this thesis further.

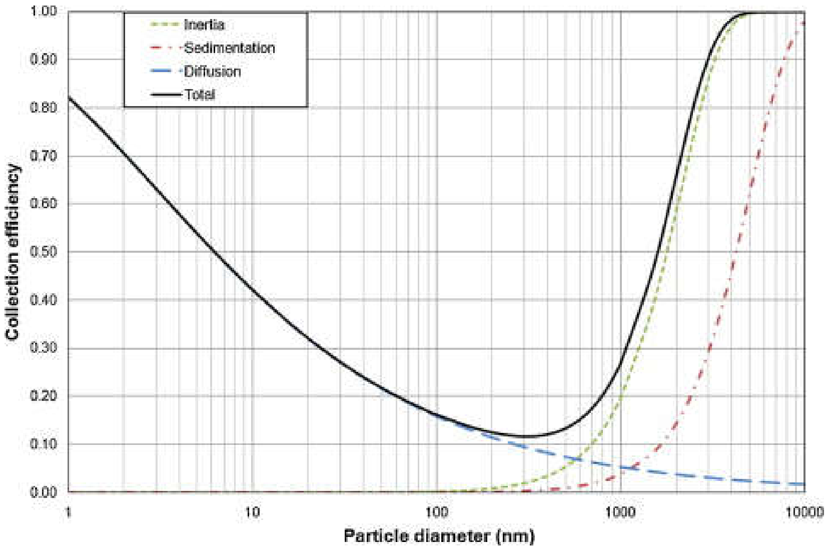

Fig. 2.6. Theoretical calculation results of a specific case with rising height 20 cm and bubble size 4 mm by the work Charvet et al. [33].

2.4.2 Particle interfacial behavior

In addition to its impact on bubble dynamics, the variation in surface tension can directly influence aerosol decontamination through particle interfacial behavior, especially when particles reach the micron-submicron scale. Depending on their affinity for water, particles can be classified as hydrophobic or hydrophilic. As a particle interacts with the gas-liquid interface, whether it could present interfacial behaviors or not is largely associated with the impact Weber number, which is defined as follows

$$We_{\mathrm{impact}} = \frac{\rho_{\mathrm{l}} d_{\mathrm{p}} U_{\mathrm{p}}^{2}}{\sigma} \tag{2.16}$$

Under the circumstance of large We_{impact} numbers, the interfacial interaction falls within the regime dominated by inertia, and the capillary effect could be safely disregarded [72]. By contrast, when We_{impact} numbers are small enough, the capillary effect will play a significant role in the interfacial interaction. This implies that the influence of gas-liquid surface tension on particle motion should be carefully considered in such scenarios.

According to Ref. [2], the aerosol size distribution of the fission products from the contamination vessel to the liquid pool is estimated in the submicron-micron range from 10 nm to 2 μm approximately, which suffices the capillary-dominant impact fully. However, the current experimental facilities are not able to track the particle interfacial detail when it comes to the submicron level. Therefore, the literature review of particle interfacial behavior will be focused on the regime from millimeter to micron, where the effect of surface tension gradually becomes dominant. The characteristics of millimeter-micron particles could serve as important references to analyze the potential behavior of submicron particles.

A classic observation of particle interfacial behavior is reported by Lee et al. [73] as exhibited in Fig. 2.7. The particle size in Fig. 2.7 is generally equal to 2 mm with an impact velocity less than 2 m/s and the particle is hydrophobic. Since the interaction is already within the capillary-dominant regime, three conspicuous interfacial behaviors are shown in Fig. 2.7. Fig. 2.7 (a) presents the process of the released particle impacting the water surface and then oscillating around the interface. In contrast, Fig. 2.7 (b) and (c) show the temporal evolution of released particles rebounding from or sinking into the interface, respectively. Lee et al. [73] categorized these interfacial behaviors as oscillation, rebound and submergence in order. Although there are some follow-up works [74-75] after the experimental observation of Lee et al. [73], the particle size is still limited to the millimeter scale owing to the limited observation methods.

To investigate the characteristics of micron-sized particles for practical relevance, Wang et al. [12] developed a dynamic model to analyze particle behavior and derived a simple criterion based on energy conservation, known as the impact velocity criterion. Their theoretical analysis revealed three interfacial behaviors for micron-sized particles, which were consistent with the observations made for millimeter-sized particles in the experiment conducted by Lee et al. [73]. Additionally, Wang et al. [12] found that for particle sizes below 10 μm, the surface tension force was the dominant force. To validate their theoretical findings, Wang et al. [76] conducted further experimental work to observe the motion of micron-sized particles, focusing on particles ranging from 50 to 200 μm in size. However, in the experiment, only two impact modes, namely submergence and oscillation, were observed, and there was a significant deviation in the critical velocity size compared to the theoretical predictions [12, 76]. This suggests that the surface tension force may not be the sole dominant force, and the prerequisite of energy conservation should include other mechanisms of energy dissipation [77].

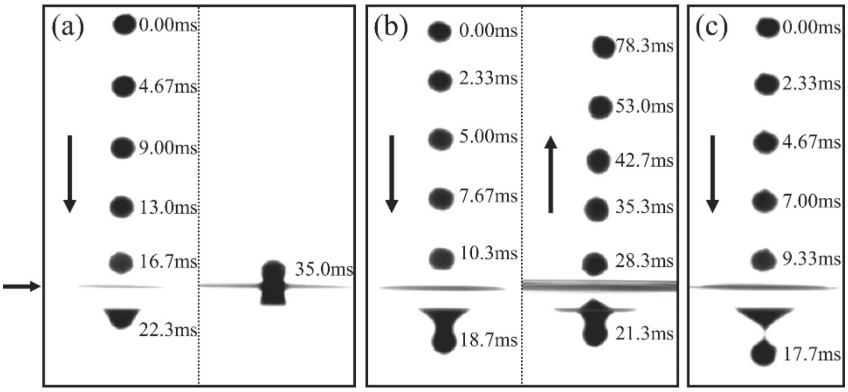

Fig. 2.7. Observation of particle interfacial behavior on the water surface in the experiment [73].

In an effort to improve upon previous studies, Ji et al. [77] utilized the VOF method to model the process of micron-sized particles impacting the gas-liquid interface, and they analyzed the energy transformation during this process. Their findings revealed that the hydrodynamic force was dominant during the early stages, while the surface tension force became the dominant force in the later stages. It is important to note that even though the exploration of a single particle impacting the gas-liquid interface has already been extended to a micron scale, the minimum particle size reported in experimental works is still larger than 10 μm as a result of the limitation in the observation method. Even though the investigated range of particle size in this work is generally within submicron-sized, the decrease in particle size will result in the capillary effect being more dominant according to Eq. (2.16). Since the impact behavior of micron and submicron particles are both located in the capillary-dominant regime, the available knowledge of micron particles from the current literature will be used to model the submicron particle transport in the next section.

One common aspect in the aforementioned investigations is that the particle is intentionally directed to impact the gas-liquid interface in a vertical manner. However, in real-world scenarios, particles may exhibit a stochastic impact angle when they collide with the gas-liquid interface, which can significantly alter the impact dynamics. An illustration of a typical oblique impact observed in experimental studies [78] is depicted in Fig. 2.8.

In Fig. 2.8, the observed particle size is approximately 200 μm, and the impact velocity does not exceed 3 m/s. A notable distinction from Fig. 2.7 is the evident difference in sphere motion and liquid surface distortion. The crucial characteristic is the non-axisymmetric wetting along the direction of velocity, leading to an imbalance of hydrodynamics and surface tension forces acting on the particle. Another significant factor is the impact angle, which plays a crucial role in determining particle behavior. A large impact angle tends to cause the particle to sink into the water, while a small impact angle allows the particle to remain on the interface. The impact angle's influence on particle behavior has been corroborated by Ji et al. [79]. They conducted additional CFD simulations to examine the possibility of particle rotation based on previous experimental observations [78]. The simulation results revealed that the non-axisymmetric wetting pattern leads to non-axisymmetric distribution of fluid pressure and shear stress along the particle surface, generating a viscous moment that induces particle rotation.

The aforementioned investigations pertain to the examination of impact behaviors involving hydrophobic particles. Due to the complex nature of fission product compounds, some radioactive particles may possess hydrophilic characteristics. Zhu et al. [13, 80-82] conducted studies on micron-sized hydrophilic particles, and a representative experimental observation of such particles is depicted in Fig. 2.9.

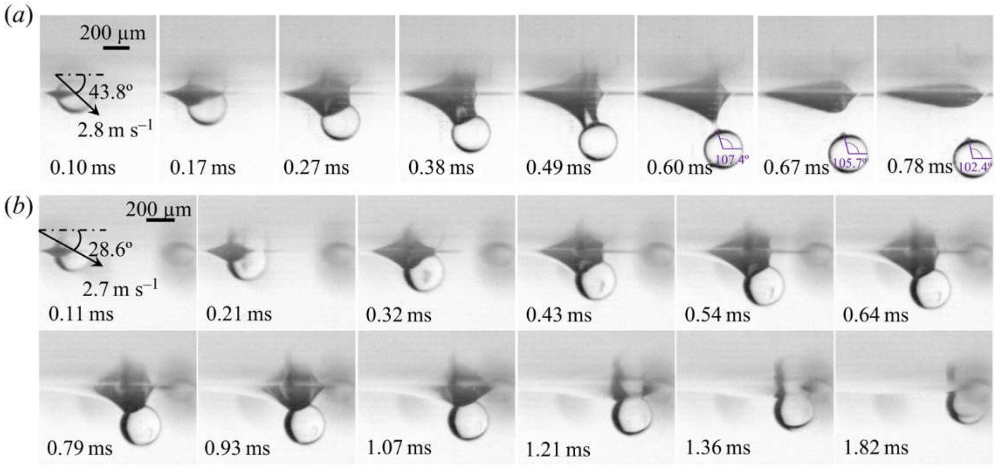

Fig. 2.8. Observation of oblique impact on the water surface in the experiment [78].

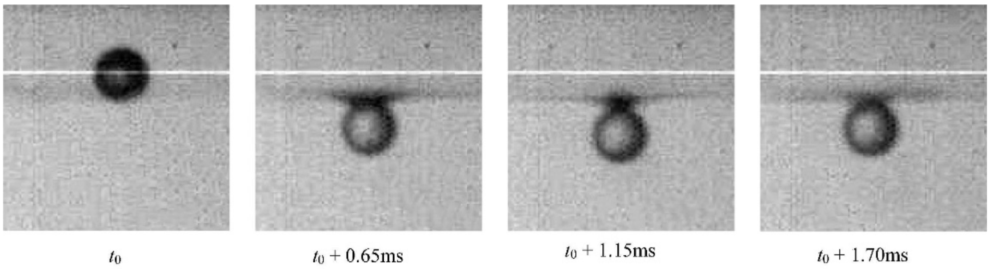

(a) Suspension mode ($d_p = 222\mu$m, $u_{p0} = 0.50$m/s, $\gamma = 73.9$mN/m)

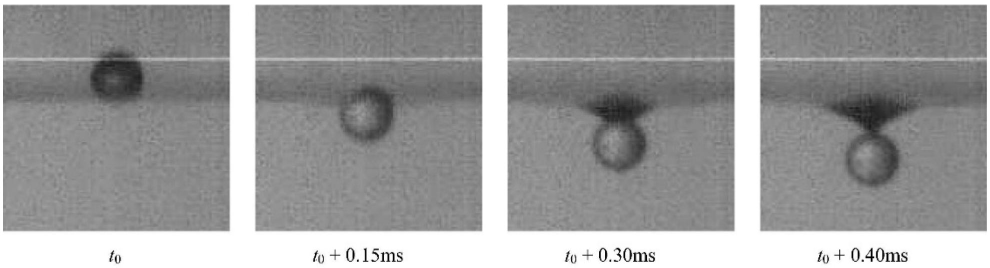

(b) Submergence mode ($d_p = 209\mu$m, $u_{p0} = 0.68$m/s, $\gamma = 73.9$mN/m)

Fig. 2.9. Observation of micron hydrophilic particles in the experiment [81].

According to Fig. 2.9, it has been established that micron-sized hydrophilic particles exhibit two types of particle interfacial behaviors, similar to hydrophobic particles depicted in Fig. 2.7. These behaviors significantly impact particle scavenging during the pool scrubbing process. As for the hydrophilic particles, their wettability is not sensitive to liquid properties, but the size of hydrodynamic and surface tension forces may change dramatically with the changing liquid properties [13]. To be specific, whether the hydrophilic particles can penetrate the interface is insensitive to the gas-liquid surface tension but an obvious hindrance effect of increasing dynamic viscosity is found in the submergence process [13]. If the rising bubble surface is partially covered with insoluble particles, the impact behavior may also change accordingly [80], which behaves similarly as interfacial behaviors presented in Fig. 2.7. Under the circumstance of the particle-laden interface, the attached particle size and the liquid dynamic viscosity has a remarkable effect on the particle penetration probability [80]. As the bubble surface is contaminated by the soluble particles, the soluble particles will take an effect like the manner of surfactants as mentioned before [37]. Besides the aspect of interface distortion, the appearance of surfactants on the interface is found to affect the particle surface wettability and particle penetration time [82]. Considering that if the difference between particle penetration time and bubble residence time is prominent, the decontamination efficiency of pool scrubbing will also be affected thereby.

2.4.3 Aerosol residence time

As previously mentioned, residence time is a crucial factor throughout pool scrubbing process because it affects the mass transfer time significantly. In terms of bubble residence time, its size at different regimes could be estimated by the ratio between zone length and bubble mean velocity [4]. Different from bubble residence time, aerosol residence time inside the swarm zone is of interest in this thesis. It is important to note that, to the author's knowledge, there is no prior investigation specifically addressing aerosol residence time. Therefore, to analyze aerosol residence time, we will introduce the concept of residence-time distribution analysis in this thesis further, drawing from the fundamental knowledge outlined in the literature [83].

2.4.4 A brief summary

We shortly presented previous studies about particle deposition mechanisms in this section and the influential factors related to particle deposition mechanisms are discussed. Regarding particle interfacial behavior, the present studies from millimeter to micron-sized particles are included as important references because of the restriction for observation of micron particles in experimental works. Furthermore, as there is a lack of investigation into aerosol residence time distribution in existing literature, fundamental concepts will be further referenced from the literature [83] in this thesis. In summary, the key conclusions derived from the aforementioned studies are as follows

(1) According to the previous theoretical work, particle deposition mechanisms consist of inertial impaction, gravitational deposition, and Brownian diffusion. When aerosol size is below 0.1 μm, the predominant Brownian diffusion could dominate aerosol decontamination, whereas the effect of inertia impaction is predominant progressively with aerosol size larger than 1 μm. As aerosol size is between 0.1 and 1 μm, all removal mechanisms could be limited, which results in a limited particle collection efficiency within this range.

(2) Based on the affinity of particles towards water, they can be classified as hydrophobic or hydrophilic, and both types exhibit at least two distinct interfacial behaviors. Considering that the aerosol size injected into the liquid pool is at the nano-micron level, the impact of particles on the gas-liquid surface will fall into the capillary-dominant regime, where surface tension force will play a paramount role in particle transport. In order to develop a numerical model, the knowledge available from studies on the impact of single micron-sized particles will be utilized to derive the interfacial penetration model afterward.

3 Fundamentals of Methodology

In this chapter, a theoretical derivation of an interfacial penetration model is presented based on experimental observations. Additionally, a criterion is proposed to elucidate various particle interfacial behaviors in simulations. Due to the intricate nature of submicron particles interacting with the gas-liquid interface, essential simplifications are indispensable to capture the prevailing factors. The suggested interfacial penetration model is integrated with the VOF-LPT method, and all governing equations are provided. Subsequently, the fundamental definition of residence-time distribution analysis in the context of aerosol decontamination processes is presented. Finally, general numerical configurations and parameter normalization techniques are introduced to facilitate subsequent parametric analysis in the following sections of this thesis.

3.1 The description of VOF method

As previously mentioned, the combination of the VOF and LPT methods will be utilized to characterize the aerosol decontamination process within the ascending bubble. The cases investigated in this study are defined under isothermal conditions to minimize complexity. Simultaneously, as the air bubble rises through water, the incompressible and immiscible conditions can be met, leading to a simplified form of the continuity equation, which is expressed as

$$\nabla \cdot U = 0 \tag{3.1}$$

Simultaneously, the momentum equation could be expressed as

$$\frac{\partial(\rho U)}{\partial t} + \nabla \cdot (\rho U U) = -\nabla p + \rho g + \nabla \cdot \mu\left(\nabla U + \nabla U^{\mathrm{T}}\right) + F_{\sigma} \tag{3.2}$$

The Continuum Surface Force (CSF) model [84] is considered to include the volumetric representation of the surface tension force as

$$F_{\sigma} = \sigma k_{\text{interface}} n_{\text{interface}} \tag{3.3}$$

In the VOF method, the interface is indicated by the gas volume fraction α_g as

$$\alpha_\mathrm{g} = \begin{cases} 0 & liquid \\ 0 < \alpha_\mathrm{g} < 1 & interface \\ 1 & gas \end{cases} \tag{3.4}$$

To guarantee the continuity of physical properties in the interfacial region, the fluid density and viscosity in this region are calculated by a weighted average as

$$\rho = \alpha_\mathrm{g}\rho_\mathrm{g} + (1 - \alpha_\mathrm{g})\rho_\mathrm{l} \tag{3.5}$$

$$\mu = \alpha_\mathrm{g}\mu_\mathrm{g} + (1 - \alpha_\mathrm{g})\mu_\mathrm{l} \tag{3.6}$$

The evolution of bubble interface and bubble motion is captured by the exchange of gas volume fraction in adjacent cells, which leads to a transport equation to govern the processes as

$$\frac{\partial \alpha_\mathrm{g}}{\partial t} + \nabla \cdot (\alpha_\mathrm{g} U) = 0 \tag{3.7}$$

Particular attention should be paid to Eq. (3.7) because it affects the sharpness of the bubble interface and consequently, both three-dimensional bubble interfacial area and aerosol decontamination are influenced. As mentioned before, bubble interfacail area in simulation is calculated by the size of an isoface [20]. If the bubble presents a smeared interface with the increasingly expanding interfacial region, the resultant effect will deteriorate the precision of the calculated bubble interfacial area embodied as the underestimation of its size ordinarily. As for aerosol decontamination, given that the judgment of aerosol position is referred to from gas volume fraction in the developed model, the smeared interface tends to keep the aerosol inside the bubble, which should be avoided in simulation beforehand.

Since the above two aspects both imply the necessity of the interface sharpness of the rising bubble, two kinds of interface sharpening schemes inside the OpenFOAM software [14] will be employed and compared to meet this requirement. The selected schemes [85-86] are termed MULES (Multidimensional Universal Limiter with Explicit Solution) and isoAdvector in this thesis.

3.1.1 The interface compression scheme

The so-called MULES scheme attempts to restrict the interface smear by the introduction of an algebraic function in Eq. (3.7) as

$$\frac{\partial \alpha_{\mathrm{g}}}{\partial t} + \nabla \cdot \left(\alpha_{\mathrm{g}} U\right) + \nabla \cdot \left[U_{\mathrm{comp}} \alpha_{\mathrm{g}} (1 - \alpha_{\mathrm{g}})\right] = 0 \tag{3.8}$$

where U_{comp} is the compressive velocity and it can be calculated as [85]

$$U_{\mathrm{comp}} = \min\left(C_{\alpha} |U|, \max\left(|U|\right)\right) \frac{\nabla \alpha_{\mathrm{g}}}{\left|\nabla \alpha_{\mathrm{g}}\right|} \tag{3.9}$$

It should be mentioned that the introduced artificial advection term $\nabla \cdot [U_c \alpha_g (1-\alpha_g)]$ will only be carried out in the interfacial region, which compresses the interface diffusion in an algebraic way [85].

3.1.2 The interface advection scheme

In contrast with the MULES scheme, the isoAdvector scheme reconstructs and advects the interface based on the interpolation of the gas volume fraction field. To be specific, the time-dependent volume fraction α inside an interfacial cell at timestep t is calculated by [86]

$$\alpha_{\mathrm{i}}(t) = \frac{1}{V_{\mathrm{i}}} \int_{C_{\mathrm{i}}} H(\boldsymbol{x}, t) dV \tag{3.10}$$

The indicator field function $H(\boldsymbol{x}, t)$ could be expressed as

$$H(\boldsymbol{x}, t) = \frac{\rho(\boldsymbol{x}, t) - \rho_{\mathrm{g}}}{\rho_{\mathrm{l}} - \rho_{\mathrm{g}}} \tag{3.11}$$

For timestep t to timestep $t+\Delta t$, the update of volume fraction could be written as

$$\alpha_{\mathrm{i}}(t + \Delta t) = \alpha_{\mathrm{i}}(t) - \frac{1}{V_{\mathrm{i}}} \sum_{\mathrm{j} \in B_{\mathrm{i}}} s_{\mathrm{ij}} \Delta V_{\mathrm{j}}(t, \Delta t) \tag{3.12}$$

$\Delta V_j(t, \Delta t)$ is the volume quantity transportation across face j, which could be calculated by [86]

$$\Delta V_{\mathrm{j}}(t,\Delta t)=\frac{1}{V_{\mathrm{i}}}\sum_{\mathrm{j}\in B_{\mathrm{i}}}\int_{t}^{t+\Delta t}\int_{F_{\mathrm{j}}}H(\boldsymbol{x},t)u(\boldsymbol{x},t)\,\mathrm{d}S_{\mathrm{ij}}\mathrm{d}t \tag{3.13}$$

The comparison of the two schemes will be performed regarding the calibration and evaluation of the bubble interfacial area in Section 4.1. Once the scheme is selected, it will be used for the whole study as a default setting.

3.2 The description of LPT method

The motion of aerosol particles is governed by Newton's motion equation within the resolved flow field obtained through the VOF method at each time step. Due to the significantly smaller size of aerosol particles compared to the bubble diameter, the occupied volume and their effect on the internal flow field can be neglected [52]. In other words, the temporal evolution of the fluid phase influences the particle phase, but not the other way around. In this scenario, the motion of aerosol particles is governed by

$$\frac{\mathrm{d}U_{\mathrm{p}}}{\mathrm{d}t}=F_{\mathrm{drag}}+\frac{g(\rho_{\mathrm{p}}-\rho_{\mathrm{c}})}{\rho_{\mathrm{p}}}+F_{\mathrm{Br}} \tag{3.14}$$

The middle term in Eq. (3.14) represents the overall effect of gravity force and buoyancy force on the particle. Once the instantaneous particle velocity is determined by Eq. (3.14), the particle displacement can be attained simultaneously as

$$\frac{\mathrm{d}L_{\mathrm{p}}}{\mathrm{d}t}=U_{\mathrm{p}} \tag{3.15}$$

It should be mentioned that when the particle size comes to micron-submicron length, the fluid phase can’t be treated as a continuous medium anymore. As a consequence, the Cunningham correction factor C_{c} should be introduced to feature particle drag force and Brownian force as [87-88]

$$F_{\mathrm{drag}}=\frac{18\mu_{\mathrm{g}}}{d_{\mathrm{p}}^{2}\rho_{\mathrm{p}}C_{\mathrm{C}}}(U_{\mathrm{g}}-U_{\mathrm{p}}) \tag{3.16}$$

$$C_{\mathrm{C}}=1+2\lambda(1.257+0.4e^{-\frac{1.1d_{\mathrm{p}}}{2\lambda}})/d_{\mathrm{p}} \tag{3.17}$$

$$F_{\mathrm{Br}}=\varsigma\sqrt{\pi S_{0}/\Delta t} \tag{3.18}$$

$$S_0 = \frac{216\mu_{\mathrm{g}} k_{\mathrm{B}} T}{\pi^2 d_{\mathrm{p}}^5 \rho_{\mathrm{p}}^2 C_{\mathrm{C}}} \tag{3.19}$$

3.3 The development of the interfacial penetration model

According to Eq. (3.14), the general process of aerosol motion inside a rising bubble is displayed in Fig. 3.1. The internal streamline will develop in the process of the bubble rising in water, which leads the aerosol moving close to the bubble surface. The internal streamline generally circulates near the bubble surface, while the aerosol may deviate from the direction of the internal streamline to impact the bubble surface owing to aerosol inertia. As discussed before, the interplay between micron-submicron aerosol and gas-liquid interface could be characterized as a kind of capillary-dominant impact [72], which means that the surface tension force on the aerosol is supposed to be a principal force once the aerosol touches the bubble surface. In this context, Eq. (3.14) should be rewritten on the impact position accordingly as follows

$$\frac{\mathrm{d}U_{\mathrm{p}}}{\mathrm{d}t} = F_{\mathrm{drag}} + \frac{g(\rho_{\mathrm{p}} - \rho_{\mathrm{c}})}{\rho_{\mathrm{p}}} + F_{\mathrm{Br}} + F_{\mathrm{ST}} \tag{3.20}$$

Nevertheless, including the explicit expression of F_{ST} into Eq. (3.20) is not practical for submicron particles due to their extremely small size, which would require an excessively refined mesh resolution. Alternatively, in the absence of this critical force in Eq. (3.14), the interfacial penetration model is derived as a compromise to include the effect of surface tension force on particle behavior in this thesis.

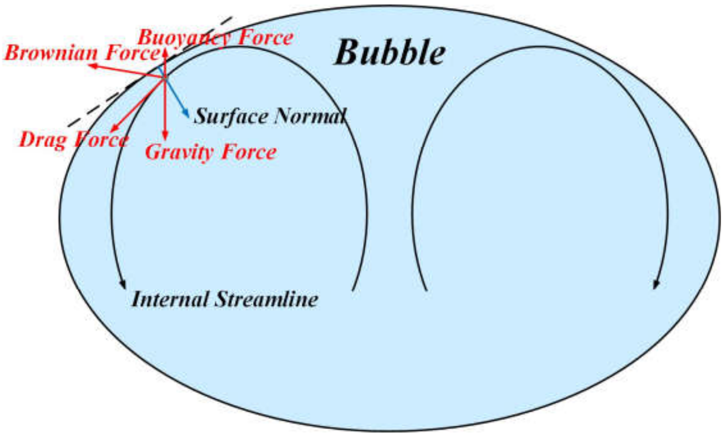

Fig. 3.1. Schematic of particle motion inside rising bubble.

The theoretical derivation of the interfacial penetration model begins by examining the physical process of how a particle interacts with the gas-liquid interface, as delineated in Fig. 3.2. As the impact happens, U_{p} can be disintegrated into the horizontal component $u_{\mathrm{p,h}}$ and the vertical component $u_{\mathrm{p,n}}$ according to the direction of local interfacial normal $n_{\mathrm{interface}}$. As for contact angles, φ stands for the contact angle between the three-phase contact line and the particle central axis, while θ represents the gas-solid contact angle. Throughout the whole impact process, φ and θ are time-dependent and affected by both three-phase physical properties and hydrodynamics, which brings about the temporal variation in surface tension force thereby [77].

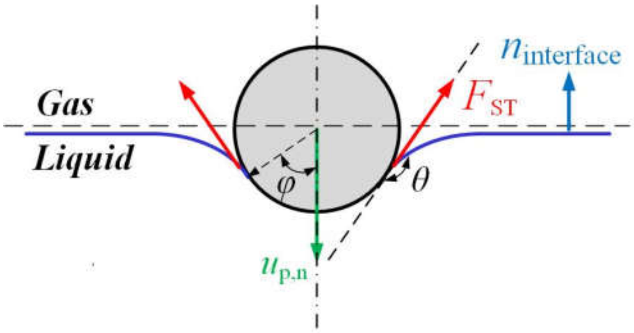

Fig. 3.2. Schematic of interaction between particle and gas-liquid interface.

It has been stated that during the whole impact process, the hydrodynamics force is predominant is the initial slamming stage, whereas the surface tension force is paramount in the middle and late stage [77]. Since the investigated case is featured by a kind of capillary-dominant impact, the particle interfacial behavior is hypothesized to be ruled mainly by the surface tension force in the middle and late stages. Regarding particle velocity, the horizontal component $u_{\mathrm{p,h}}$ may affect the non-axisymmetric particle wetting and then influence both hydrodynamics and surface tension forces on particles [78]. By contrast, the increase in vertical component $u_{\mathrm{p,n}}$ advantages the depth of particle submergence on the interface, which could beget a rising particle penetrating probability thereafter. It is undisputed that $u_{\mathrm{p,n}}$ is much more influential than $u_{\mathrm{p,h}}$ to affect particle interfacial behavior. Therefore, only the vertical velocity component is considered for simplification. Along this direction, the vertical component of surface tension force $F_{\mathrm{ST,v}}$ on the particle could be written as [12]

$$F_{\mathrm{ST,v}} = -\pi \cdot \sigma \cdot d_{\mathrm{p}} \cdot \sin(\varphi) \cdot \sin(\varphi + \theta) \tag{3.21}$$

Based on the previous assumption, the variation in particle vertical momentum could be characterized as

$$(m_{\mathrm{p}} u_{\mathrm{p,n}} - m_{\mathrm{p}} u'_{\mathrm{p,n}}) \propto F_{\mathrm{ST,v}} \cdot \Delta t \tag{3.22}$$

Considering the extreme case of particle vertical velocity reducing to zero, the relationship in Eq. (3.22) could be further simplified as

$$m_{\mathrm{p}} u_{\mathrm{p,n}} \propto F_{\mathrm{ST,v}} \cdot t_{\mathrm{p}} \tag{3.23}$$

Assumed the particle shape to be spherical, Eq. (3.23) could be further transformed with the introduction of Eq. (3.21) as

$$\frac{1}{6}\cdot\pi\cdot d_{\mathrm{p}}^{3}\cdot\rho_{\mathrm{p}}\cdot u_{\mathrm{p,n}} \propto -\pi\cdot\sigma\cdot d_{\mathrm{p}}\cdot\sin(\varphi)\cdot\sin(\varphi+\theta)\cdot t_{\mathrm{p}} \tag{3.24}$$

The particle penetration time [81] can be substituted by

$$t_{\mathrm{p}} \propto \frac{L_{\mathrm{p}}}{u_{\mathrm{p,n}}/2} \tag{3.25}$$

The physical size of particle displacement in the interfacial process is of the same level compared to particle size. By introducing Eq. (3.25) into Eq. (3.24), a terminal interrelationship could be epitomized as

$$\frac{\rho_{\mathrm{p}}\cdot d_{\mathrm{p}}\cdot u_{\mathrm{p,n}}^{2}}{\sigma} \propto \sin(\varphi)\cdot\sin(\varphi+\theta) \tag{3.26}$$

In light of Eq. (3.26), it can be got that when the particle velocity reduces to zero at a specific time point, the terminal size of φ and θ are subject to the left term in Eq. (3.26). In general, when φ and θ are large sufficiently in the particle submerging process, the liquid surface may close, which results in the complete submergence of particles into the liquid water. Therefore, a particle Weber number We_{p} could be generalized in this work as the pivotal criterion by

$$We_{\mathrm{p}} = \frac{\rho_{\mathrm{p}}\cdot d_{\mathrm{p}}\cdot u_{\mathrm{p,n}}^{2}}{\sigma} \tag{3.27}$$

The utility of We_{p} is to indicate different particle interfacial behaviors. Despite that two or three kinds of interfacial behavior may appear reliant on particle wettability and impact conditions, only submergence and no-submergence behaviors are considered in this work for simplification. The submergence behavior refers to the condition that the particle can keep submerging in the whole interfacial process, which contributes to the shift of the particle from gas to liquid phases eventually. The no-submergence behavior means that the effect of particle inertia force is not predominant enough to counteract that of surface tension force, which results in the reverse motion of the particle. Based on this key criterion, the schematic of the interfacial penetration model could be well-delineated as shown in Fig. 3.3. It can be observed that the interfacial region has been indicated by the size of gas volume fraction α_{g}, which is given with the range between 0.9 and 0.1. When α_{g} is higher than 0.9, the position of the particle is deemed to be the gas phase. Conversely, the position with α_{g} below 0.1 is thought to be the liquid phase. The particle motion in the gas phase is governed by Eq. (3.14) and (3.15), while the particle in the liquid phase is deleted from the computational domain to reduce computational load.

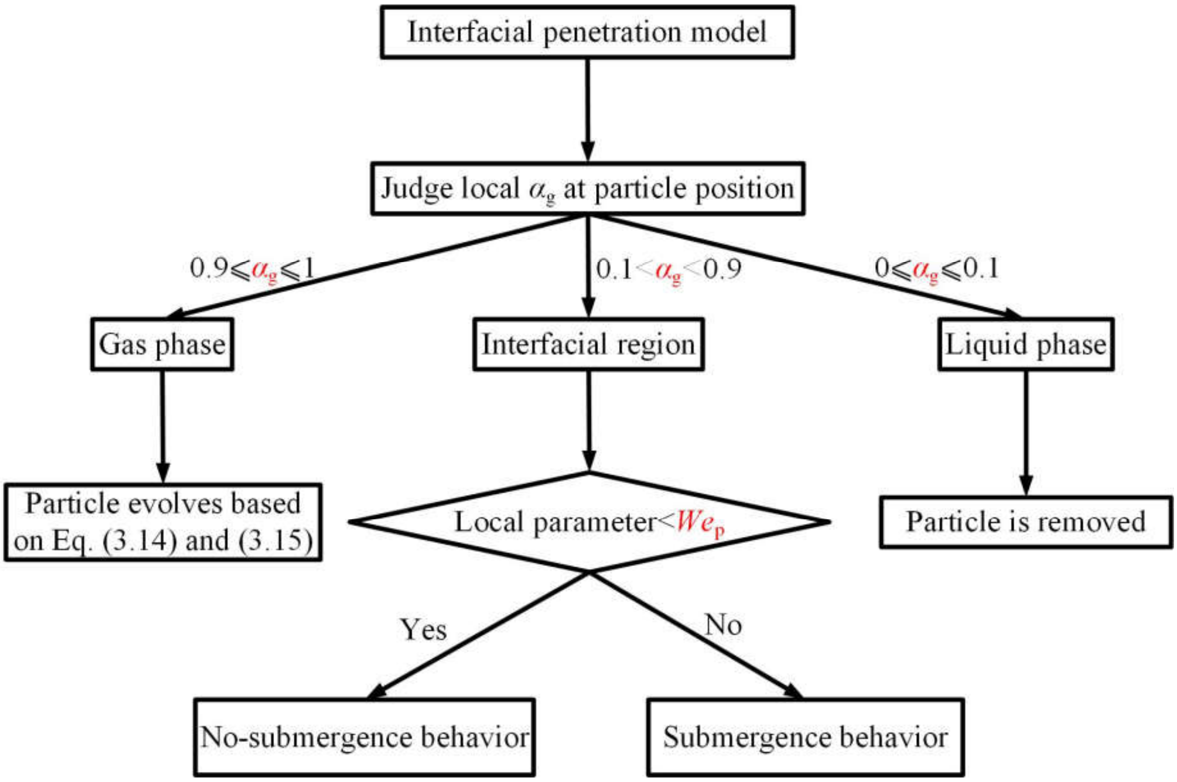

Fig. 3.3. Schematic of the interfacial penetration model.

It should also be emphasized here that in the theoretical dedication, the context can be described by a moving particle impacting the stagnant interface, while that is illustrated by the particle hitting the moving interface in the simulation. To handle the transformation from the stagnant to the moving interfaces, some reinterpretations should be made in the physical meanings of We_p from the theoretical derivation to the numerical implementation.

In the theoretical derivation, when the local parameter is higher than the critical particle Weber number, the particle is thought to be able to submerge over the whole process and the time scale is referred to as penetration time. Similarly, when it comes to the moving interface, the moving interface is thought to be a combination of numerous stagnant interfaces, which is also the fundamental basis of the VOF method. Regarding each stagnant interface, the particle Weber number is used to indicate whether the particle could keep submerging at the current timestep or not. Different from the case of a stagnant interface, the judgment should be performed at the beginning of each timestep in view of the transient variation in the interfacial normal of the interface. Whether the particle could penetrate the interface at the end is dependent on its performance on the interface at each instant.

According to the above reinterpretations, further artificial modification of particle velocity in simulation should be carried out to match the previous definition of non-submergence and submergence behaviors. At each timestep, when the no-submergence behavior appears, the particle will reverse its motion and its rebound velocity is estimated by

$$u_2 = u_{\text{interface}} + |u_1| \cdot n_{\text{interface}} \tag{3.28}$$

Since Eq. (3.28) is only an approximation of particle rebound velocity in simulation, its credibility will be checked later by the comparison of simulation results against experimental data. In terms of particle submergence behavior at each timestep, two foundational characteristics should be included, which are the particle displacement toward the outside bubble and the deceleration of particle velocity because of surface tension force. As for the first point, since the particle velocity has a vertical component opposite to the bubble interfacial normal, it could be satisfied in nature. Regarding the deceleration effect, although the surface tension force on the particle is absent in the simulation, the increasing drag force on the particle due to the increased fluid viscosity contributes to the deceleration of the particle according to Eq. (3.6) and (3.16). Since two main features have been already manifested in the simulation, no artificial modification is made to the submergence behavior for simplification.

3.4 Residence-time distribution analysis

When considering the transport of aerosols through a rising bubble, it can be conceptualized as a process from input to output. In this context, the initial aerosol number is considered as the input, while the cumulative removed aerosol number is regarded as the output. To describe this relationship, a cumulative F-curve [83, 89] can be defined as

$$F(t) = \frac{N(t)}{N_{\text{initial}}} = \int_0^t E(t)\,\mathrm{d}t \tag{3.29}$$

It can be got that as the physical time is long enough, the terminal size of $F(t)$ should be equal to one eventually, which signifies that all particles are decontaminated in the end. In terms of E-curve, it could be defined by a difference format as

$$E(t) = \frac{F(t) - F(t - \Delta t)}{\Delta t} \tag{3.30}$$

Based on Eq. (3.30), aerosol residence time and variance [90] could be defined by the summation form as

$$t = \mathrm{i} \cdot \Delta t \tag{3.31}$$

$$MRT = \sum_{\mathrm{i}=0}^{N} tE(i \cdot \Delta t)\Delta t \tag{3.32}$$

$$\sigma^2 = \sum_{i=0}^{N} (t - MRT)^2 E(i \cdot \Delta t)\Delta t \tag{3.33}$$

where MRT is aerosol mean residence time and σ^2 is the variance. MRT is similar to the mathematical expectation, while variance is to evaluate how far disperse data deviate from the mathematical expectation. In this thesis, residence-time distribution analysis will be employed to investigate the temporal decontamination behaviors of aerosols. The analysis will explore various influential factors that impact the residence-time distribution function, with the aim of identifying the key parameters that affect the aerosol mean residence time.

3.5 Numerical configuration

The case of a single bubble with internal particles rising in quiescent liquid is investigated in this work and the typical schematic is presented in Fig. 3.4. The geometry height is equal to $20d_b$, where d_b refers to bubble size. In the beginning, the bubble is assumed to be spherical and it is put along the central axis with a height $5d_b$. The cross-section of the computational domain is a square with the area equal to $5d_b \times 5d_b$.

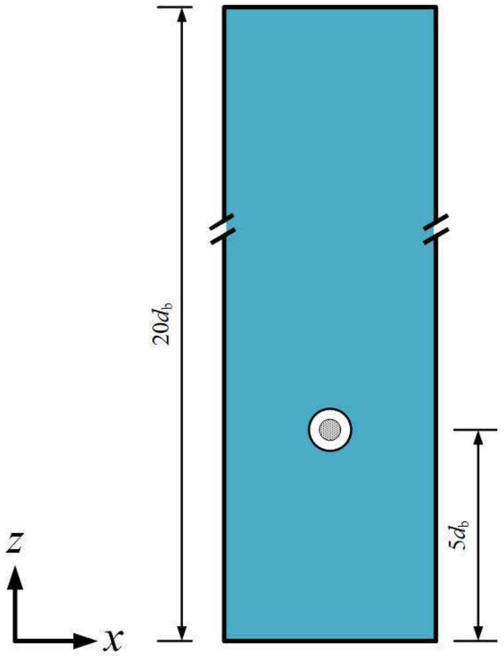

Fig. 3.4. Schematic of a bubble with internal aerosol rising in quiescent liquid.

To track the long-term bubble and aerosol behaviors, the computational domain is moving along the z direction and its velocity is set to be equal to the bubble terminal velocity roughly, which is to make sure the bubble could reach the terminal stage in the end. Except for detailed physical parameters in each sub-sections, the boundary conditions for all cases are consistent in the software OpenFOAM [14]. As for the side and bottom walls, the velocity conditions are set to no slip, whereas the so-called “pressureInletOutletVelocity” is given at the top patch. In the VOF method, the PIMPLE (Pressure Implicit with Splitting of Operator) is applied to solve the pressure-velocity coupling, while aerosol evolution is performed based on the C++ library “intermediate” inside OpenFOAM [14].

3.6 Parameter normalization and dimensionless numbers

Bubble interfacial area in this work is normalized by the surface area of a spherical bubble with the equivalent size as

$$BDF = \frac{A}{\pi d_{\mathrm{b}}^2} \tag{3.34}$$

The normalized bubble interfacial area is also termed as bubble deformation factor (*BDF*). As implied by the name, *BDF* could be utilized to delineate the deformation degree of the bubble. As *BDF* is equal to 1, it means that the present bubble shape approaches to a round shape with rather limited deformation. Otherwise, bubble deformation is remarkable with a high *BDF*.

In light of the definition in the work [64], the size of bubble rising velocity in simulation could be calculated by

$$U_{\mathrm{b}} = \frac{\sum_{x=1}^{N_{\mathrm{x}}} \sum_{y=1}^{N_{\mathrm{y}}} \sum_{z=1}^{N_z} \alpha_{\mathrm{g}} U_{\mathrm{z}}}{\sum_{x=1}^{N_{\mathrm{x}}} \sum_{y=1}^{N_{\mathrm{y}}} \sum_{z=1}^{N_z} \alpha_{\mathrm{g}}} \tag{3.35}$$

where the subscripts of x, y and z represents the spatial direction x, y and z in Fig. 3.4. U_{z} is the velocity component of each cell along z direction. $\mathrm{N_x}$, $\mathrm{N_y}$ and $\mathrm{N_z}$ is cell number of the whole computation domain along each direction.

Physical parameters in this work are normalized according to the properties of bubbles and bubble rising velocity is normalized as [24]

$$U^* = \frac{U_{\mathrm{b}}}{\sqrt{gR_{\mathrm{b}}}} \tag{3.36}$$

Analogously, the component of bubble mass centroid displacement along each direction could also be normalized as

$$x^* = \frac{x}{R}, \quad y^* = \frac{y}{R}, \quad z^* = \frac{z}{R} \tag{3.37}$$

The normalization of physical time could be written as

$$t^* = \frac{t}{\sqrt{R_\mathrm{b}/g}} \tag{3.38}$$

Two main dimensionless numbers are included in this work and the definitions are given by

$$Ga = \frac{\rho_\mathrm{l}\sqrt{gR_\mathrm{b}}R_\mathrm{b}}{\mu_\mathrm{l}} \tag{3.39}$$

$$Eo = \frac{\rho_\mathrm{l} g R_\mathrm{b}^2}{\sigma} \tag{3.40}$$

where *Ga* signifies the relative significance between gravity force and viscous force and *Eo* denotes the relative importance between gravity force and surface tension force.

To evaluate aerosol removal efficiency, aerosol decontamination factor is defined as

$$DF = \frac{N_\mathrm{initial}}{N_\mathrm{remain}} \tag{3.41}$$

4 Bubble Dynamics and Topology

In this chapter, the pivotal parameter, namely bubble three-dimensional interfacial area is calibrated and assessed against the experimental data. Several influential factors such as interfacial sharpening schemes, mesh resolution and the threshold of gas volume fraction are investigated to achieve the optimal agreement between simulation results and experimental data under the circumstance of stable bubbles. Subsequently, the specified numerical settings will be further used to analyze bubble dynamics in the air-water system. Bubble long-term behaviors and the velocity-shape dependence is particularly checked. Finally, the effort is made to correlate bubble terminal interfacial area with dimensionless numbers in the context of a wide coverage of physical properties. Since bubble breakup may occur under certain conditions, the investigation of bubble breakup will also be briefly included because it may influence the upper boundary of the proposed correlation.

4.1 Selection and validation of numerical approach

In this section, the physical properties for simulation are chosen based on Table 4.1, with the bubble size being adjustable accordingly. To examine whether the side wall distance affects bubble terminal interfacial area, Fig. 4.1 shows the temporal evolution of bubble interfacial area. On the whole, the wall effect on bubble interfacial area is rather limited for small *Ga* numbers and could be ignored.

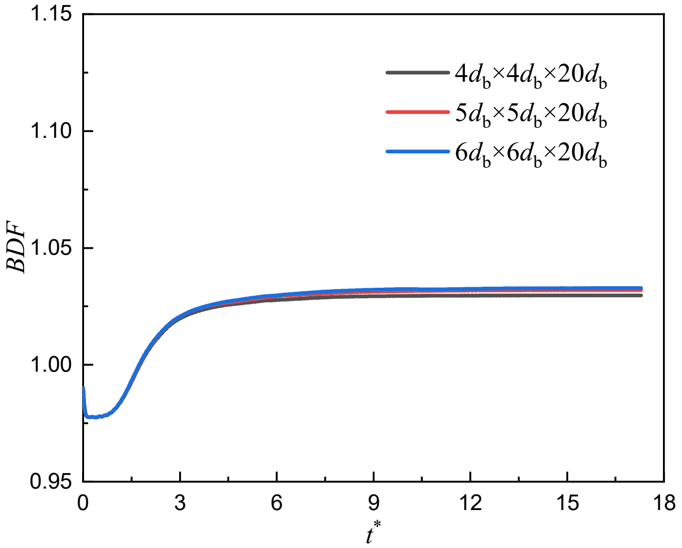

Fig. 4.1. Wall effect on bubble terminal interfacial area.

Table 4.1 Physical properties for validation.

Liquid properties	Density (kg/m^3)	Viscosity (mPa·S)	Surface tension (mN/m)
Liu et al. [91]	1206.5	63.0	67
Legendre et al. [22]	1225	80.0	62.7

Fig. 4.2 illustrates the relationship between the bubble interfacial area and mesh resolution for the isoAdvector and MULES schemes. According to Eq. (2.12), the bubble contour in the simulation is represented by a multi-face geometry. To reflect the smoothness of the multi-face geometry, the mean isoface cell number is presented in Fig. 4.2. It can be observed that an increase in the cell per diameter (*CPD*) leads to a higher mean isoface cell number, irrespective of the interfacial sharpening scheme employed. Generally, the refined mesh could ameliorate the smoothness of the isoface and affect bubble terminal interfacial area thereafter. In Fig. 4.2, when *CPD* is higher than 18, the effect of mesh resolution on bubble interfacial area could be omitted safely. Due to the limitation in computational resources, the *CPD* equal to 20 will be used in the following sections as a default condition unless it is especially elaborated. In addition to that, the selection of different interfacial schemes affects the size of bubble interfacial area remarkably. Among all cases, the utilization of isoAdvector scheme brings about a larger bubble interfacial area compared to that with MULES schemes, which may also affect other physical properties meanwhile.

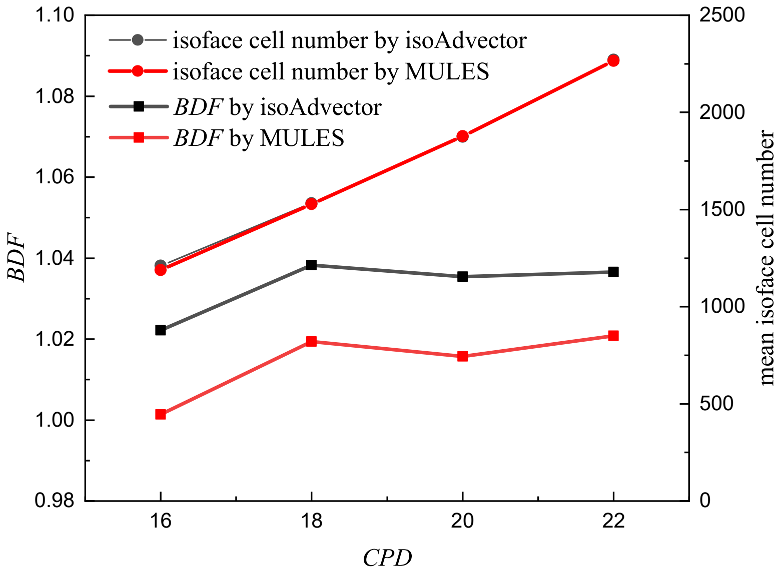

Fig. 4.2. Mesh sensitivity study of isoAdvector and MULES for a 6 mm bubble.

To thoroughly examine the influence of interfacial sharpening schemes, Fig. 4.3 and 4.4 demonstrate their impact on bubble aspect ratio and terminal velocity. In this thesis, bubble aspect ratio refers to the ratio between the major and minor axes of the bubble. In Fig. 4.3, the use of the isoAdvector scheme results in a higher bubble aspect ratio for all cases, causing a discrepancy between the simulation and experimental results for small bubbles, while exhibiting good agreement for large bubbles. Conversely, the application of the MULES scheme significantly underestimates the bubble aspect ratio for large bubbles. Given that the maximum relative errors for both schemes are generally within 10%, it can be thought that both schemes could represent bubble shape with acceptable accuracy in given conditions. As for bubble terminal velocity, it is insensitive to interfacial sharpening schemes in all cases as shown in Fig. 4.4 and both schemes could achieve a good match in contrast to experimental data.

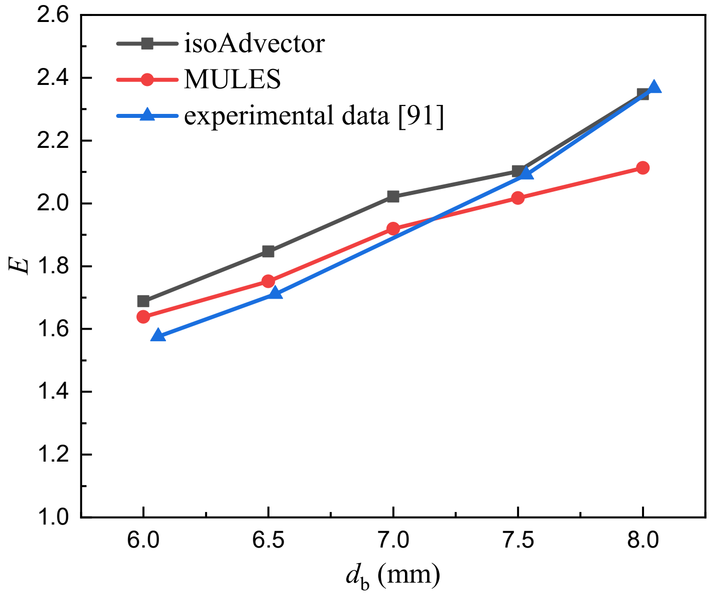

Fig. 4.3. Validation of bubble aspect ratio in simulation by experimental data.

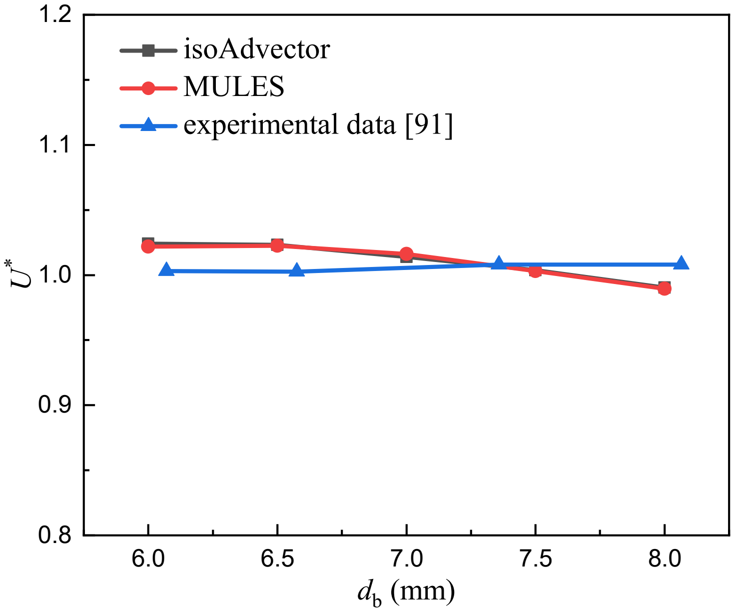

Fig. 4.4. Validation of bubble terminal velocity in simulation by experimental data.

In addition to bubble aspect ratio and terminal velocity, the following emphasis is allocated for the examination of bubble interfacial area. To check the authenticity of numerical results, the initial and terminal bubble interfacial area for isoAdvector and MULES schemes are studied accordingly. As defined previously, the initial bubble shape is set to be spherical, which means that the initial interfacial area could be calculated by $4\pi R_b^2$. Fig. 4.5 exhibits the comparison between isoAdvector and MULES schemes for the initial interfacial area. Since there exists nearly no bubble shape deformation in the very beginning, bubble interfacial area is irrelevant to the interfacial schemes in Fig. 4.5. It should be mentioned that in the initialization process, the gas volume fraction field for each cell is either 0 or 1, which introduce an interpolation error. As a consequence, the ideal agreement between simulation results and experimental data can't be realized with a specified α_g in Fig. 4.5 when bubble size is changed. Overall, the acceptable threshold of α_g could be narrowed down within the scale from 0.5 to 0.55 in light of Fig. 4.5. The evaluation of bubble terminal interfacial area is shown in Fig. 4.6. The results indicate that in addition to the threshold of α_g, the selection of interfacial sharpening scheme is also a principal factor to influence bubble interfacial area. According to Fig 4.6, it can be got that the isoface with α_g equal to 0.5 by MULES or that with α_g equal to 0.55 by isoAdvector could achieve the optimal match between numerical and experimental data in given conditions.

To check the capacity of two schemes in suppressing interfacial diffusion, a parametric study is performed by the alternation in *Ga* and *Eo* numbers. The benchmark point is selected with the condition of bubble size equal to 6 mm in Fig. 4.6, while the previously determined optimal α_g of the isoface for two schemes is also employed. The effect of *Ga* numbers on bubble interfacial area is presented in Fig. 4.7. In terms of isoAdvector, all curves descend in the beginning because of the development of the interfacial region and subsequently rise to a steady state. Nevertheless, a continuously decreasing interfacial area is found in Fig. 4.7 (b) when MULES scheme is applied, which means the adopted interfacial scheme can't fulfill a stable interfacial region under the circumstance of large *Ga* numbers. Analogously, a similar trend is also embodied in Fig. 4.8. With the decreasing *Eo* numbers, the terminal bubble shape can be guaranteed among cases with isoAdvector, whereas slightly oscillated curves are found for high *Eo* numbers with MULES. In light of the above analysis, it could be generalized that the isoAdvector scheme is more suitable than MULES scheme to calculate bubble interfacial area. Regarding the numerical approach, a *CPD* value of 20 and the isoAdvector scheme will be selected as the default settings for the subsequent analysis.

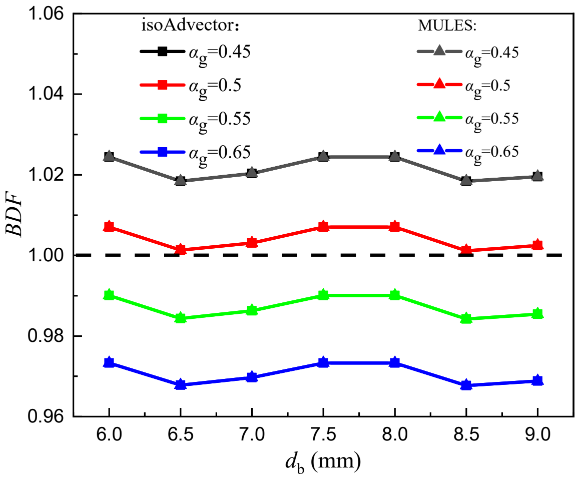

Fig. 4.5. Comparison of bubble initial interfacial area for isoAdvector and MULES.

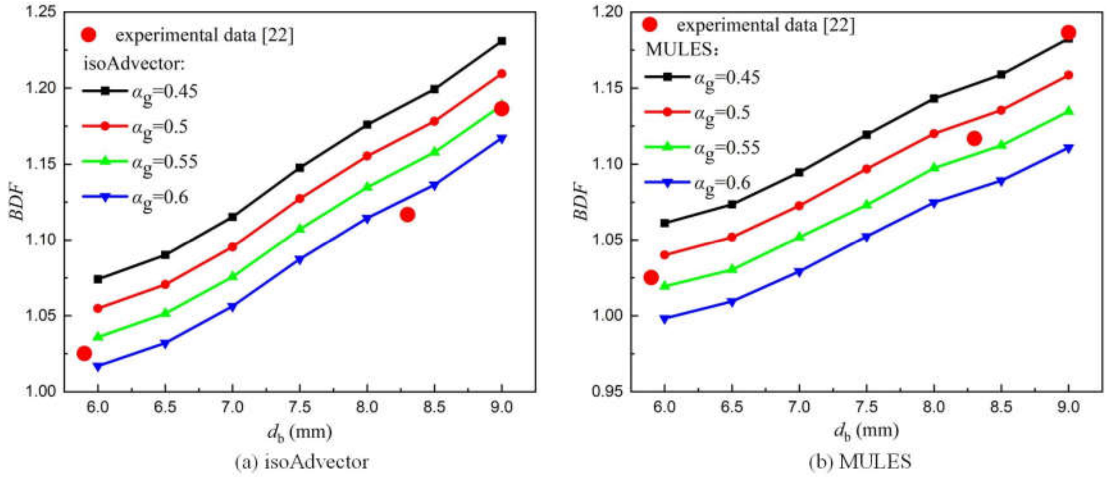

(a) isoAdvector

(b) MULES

Fig. 4.6. Comparison of bubble terminal interfacial area for isoAdvector and MULES based on experimental data.

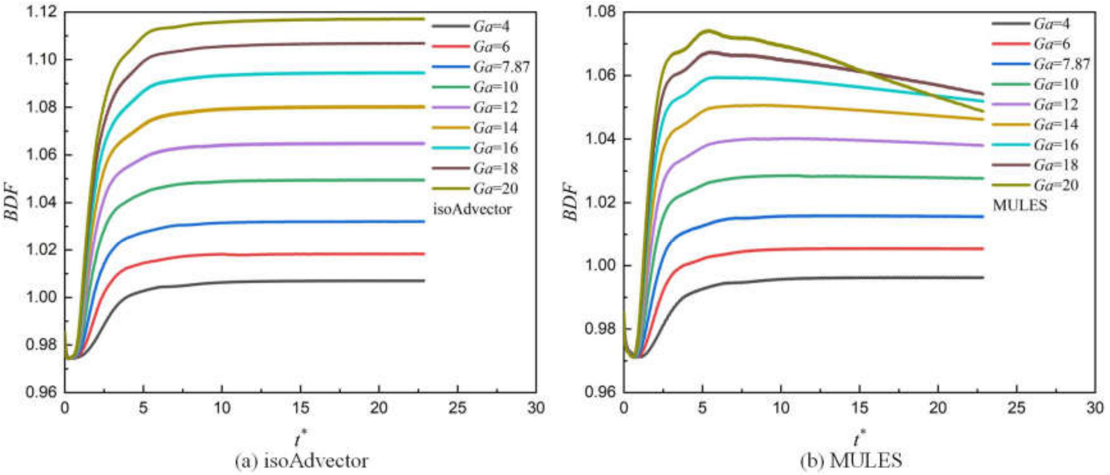

(a) isoAdvector

(b) MULES

Fig. 4.7. Effect of Galilei numbers on bubble interfacial area for isoAdvector and MULES.

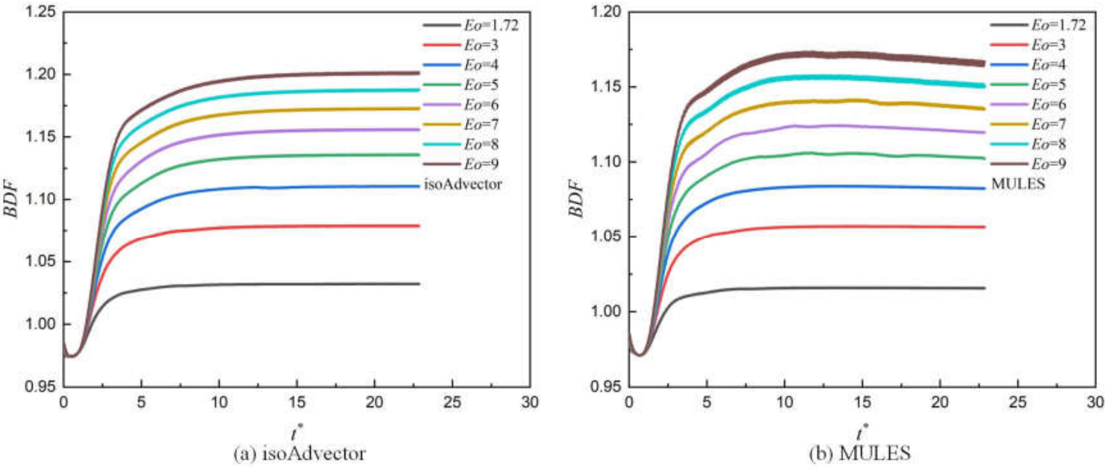

(a) isoAdvector

(b) MULES

Fig. 4.8. Effect of Eötvös numbers on bubble interfacial area for isoAdvector and MULES.

4.2 Bubble dynamics

Considering that bubble residence time in industrial applications may last a few seconds, the characteristics of bubble long-term dynamics are investigated in this section. The properties are defined in Table 4.2 and bubble size is fixed at 7 mm. Other numerical settings accord with the previous description.

Table 4.2 Physical properties in the air-water system.

Fluid properties	Density (kg/m^3)	Viscosity (mPa·S)	Surface tension (mN/m)
Air	1.225	1.789×10^{-2}	72.8
Water	1000	1	

Fig. 4.9 shows the displacement component along each direction and the projection of bubble displacement on the *x*-*y* plane. Before t^* comes to 20, both x^* and y^* remain zero and the bubble rises in a straight path. Afterwards, the periodic oscillations in the x^* and y^* happen, which implies that the bubble trajectory is helical. Regarding the vertical direction, z^* increases continuously with a nearly constant slope. When t^* is below 50, the bubble moves with sharp turns due to the development in horizontal motion. Subsequently, the bubble follows a centripetal motion approximately, which matches the properties of helical motion from a three-dimensional perspective.

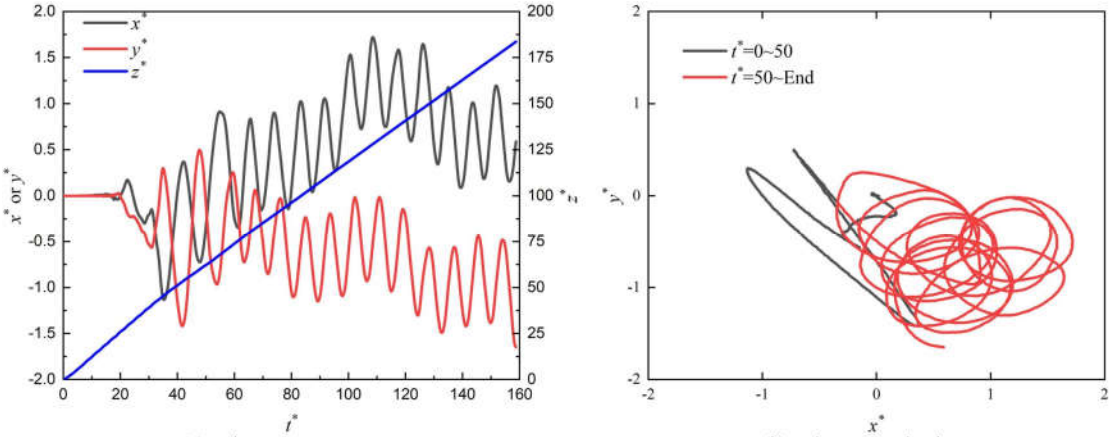

(a) trajectory component (b) trajectory projection

Fig. 4.9. Bubble trajectory component and projection with bubble size equal to 7 mm.

Fig. 4.10 shows the evolution of bubble interfacial area and rising velocity. On the whole, both curves could be characterized as two main stages, namely the damped oscillatory stage and the quasi-stable stage. Specifically, both curves oscillate to the maximum before t^* reaches 40 and then dampen progressively to the pseudo-steady status. Since both curves seem to follow a similar oscillatory pattern, the shape-velocity dependence will be especially investigated further.

To reveal bubble shape evolution and bubble motion in the quasi-stable stage, Fig. 4.11 presents the temporal bubble motion at t^* from 153.9 to 158.7. The time interval is constant and equal to 0.53 and time sequences are numbered in chronological order. Overall, bubble shape is similar at all time steps and could be treated as an ellipsoidal shape roughly. In sequence 1, bubble

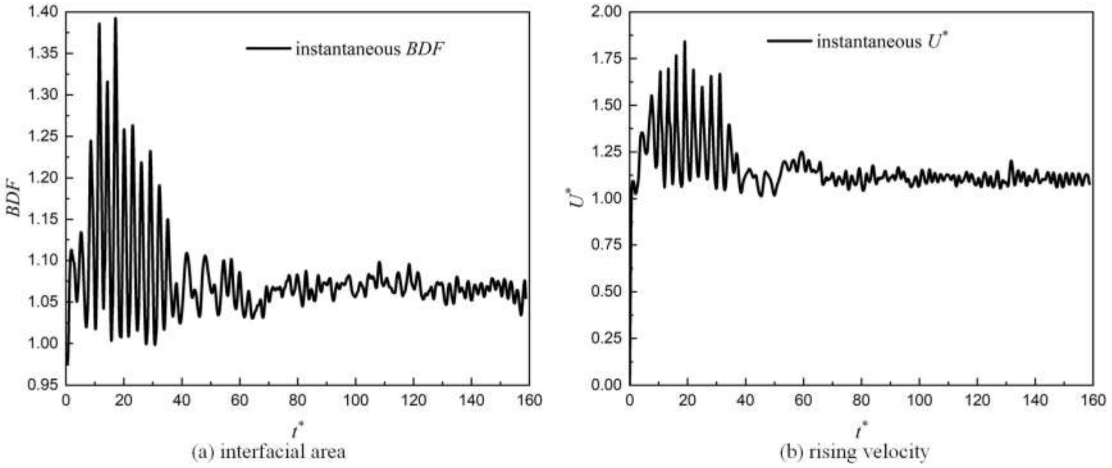

Fig. 4.10. Temporal evolution of bubble interfacial area and rising velocity with bubble size equal to 7 mm.

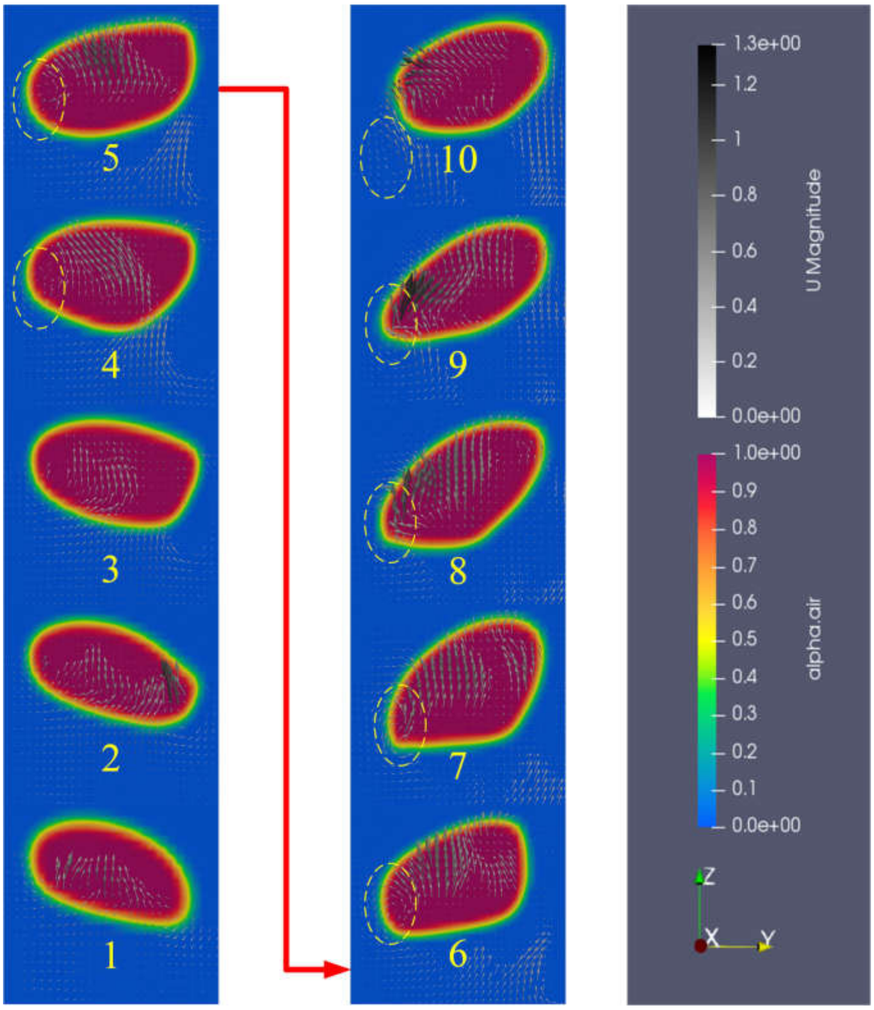

Fig. 4.11. Bubble shape evolution in the quasi-stable stage.

mass centroid locates in the right rear part. Owing to the effects of gas-liquid surface tension and imbalance of internal pressure distribution, the high-speed gas jet is observed, which points to the upper left direction in sequence 2. In the presence of the gas jet, the bubble's right part is pushed forward and bubble mass centroid deviates to the opposite side and the whole internal flow field also progressively deflects to the left. Afterwards, the internal vortex is observed in sequence 4. As the bubble's right rear interface is elevated, the pronounced bubble wake develops, which gives rise to the bubble deviation in sequence 5. In sequences 6 and 7, the internal vortex continues developing and affects bubble motion. Subsequently, the high-speed gas jet appears again and points in the right direction in sequence 8. However, the vortex comes to the bubble interface in sequence 9 and vortex shedding appears in sequence10. As a result of vortex shedding, even though the internal high-speed gas jet points to the right, the rising bubble deflects in the opposite direction. It can be concluded that the presence of vortex shedding results in the momentum transfer from gas phase to liquid phase, which affects bubble motion remarkably.

According to the previous analysis, it can be got that bubble shape evolution is highly sensitive to the bubble's internal flow field. Therefore, the velocity-shape dependence is particularly of interest, which will be checked thoroughly. As a representative case, a 6 mm bubble rising in water will be checked and other numerical settings are identical to Table 4.2. Similar to the previous long-term analysis of bubble dynamics, bubble displacement components and the projected trajectory is presented in Fig. 4.12. Although bubble size is changed, bubble motion pattern is almost the same, which means that the bubble rises straightly within a short period and then ascends in a helical manner.

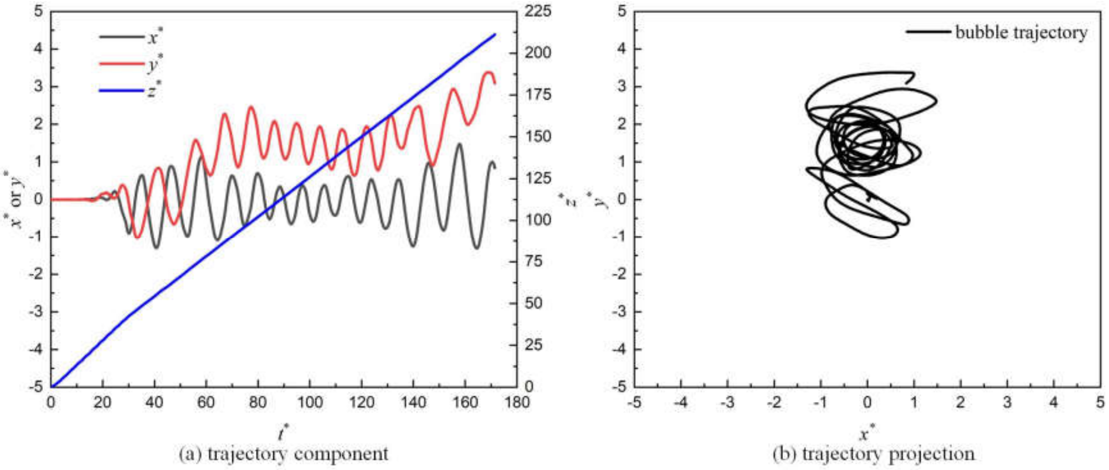

(a) trajectory component (b) trajectory projection

Fig. 4.12. Bubble trajectory component and projection with bubble size equal to 6 mm.

Fig. 4.13 presents the temporal evolution of bubble interfacial area and rising velocity. It is evident that even in the quasi-stable stage, a significant fluctuation in the temporal curves can occur with decreasing bubble size. Considering that the bubble trajectory may also impact the velocity-shape dependence, the first third of the temporal curves in Fig. 4.13 are extracted and analyzed, as depicted in Fig. 4.14. An explicit relationship is discovered, indicating that the local minima of *BDF* correspond to local maxima of velocity, and vice versa. These findings suggest that in the damped oscillatory stage, a less deformed bubble shape can result in a higher transient rising velocity.

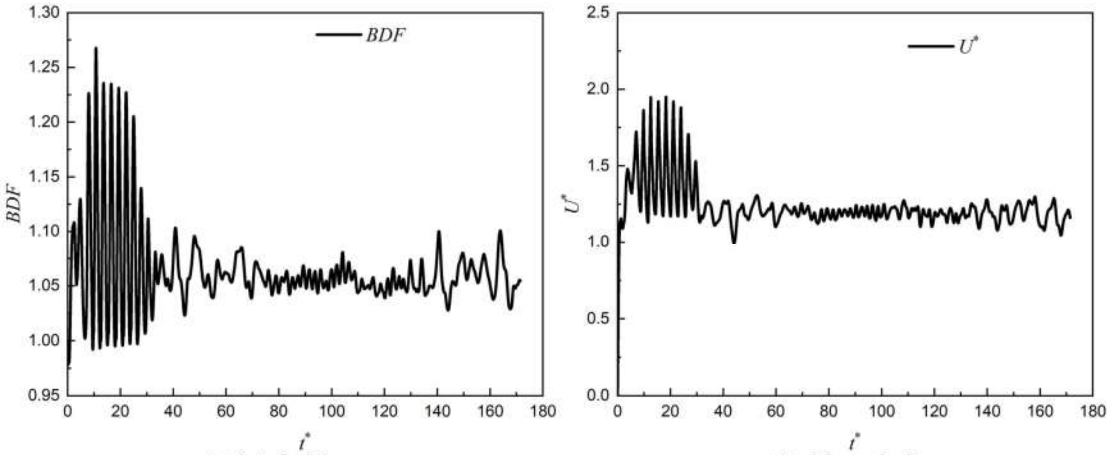

(a) interfacial area

(b) rising velocity

Fig. 4.13. Temporal evolution of bubble interfacial area and rising velocity with bubble size equal to 6 mm.

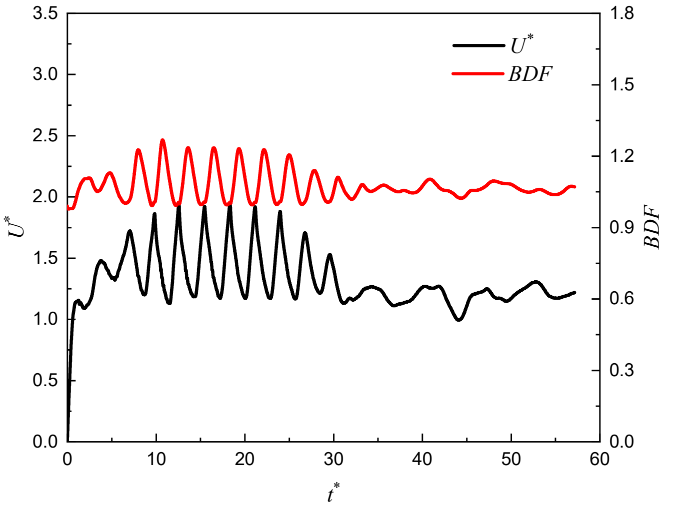

Fig. 4.14. Velocity-shape dependency in the damped oscillatory stage.

The temporal evolution of the bubble's internal flow field is illustrated in Fig. 4.15, with the corresponding time span indicated in Fig. 4.16. Consistent with the previous analysis, the bubble shapes are labeled from 1 to 10 in a sequential manner. Initially, the bubble shape appears as a flattened oblate form. In presence of a large bubble front surface contacting with liquid water, the pressure drag force on the bubble is relatively large, which thereupon results in the deceleration in bubble velocity in the time sequences from 1 to 3. Concurrently, since the bubble presents a highly deformed shape at the starting point, the large interface curvature results in a dominant surface tension force on the bubble according to Eq. (3.3), which contributes to the bubble shape relaxing to the initial round shape embodied in the time sequences from 1 to 6. Furthermore, given that the contacting area between air and water is decreased in the shape relaxation process, the bubble buoyancy force is more predominant than the drag force and consequently, the bubble accelerates and the peak comes at sequence 7. At this specific time point, the bubble presents a nearly round shape and the highest local rising velocity. After that, further shape deformation occurs, which is followed by the deceleration of bubble rising velocity in the time sequences from 8 to 10.

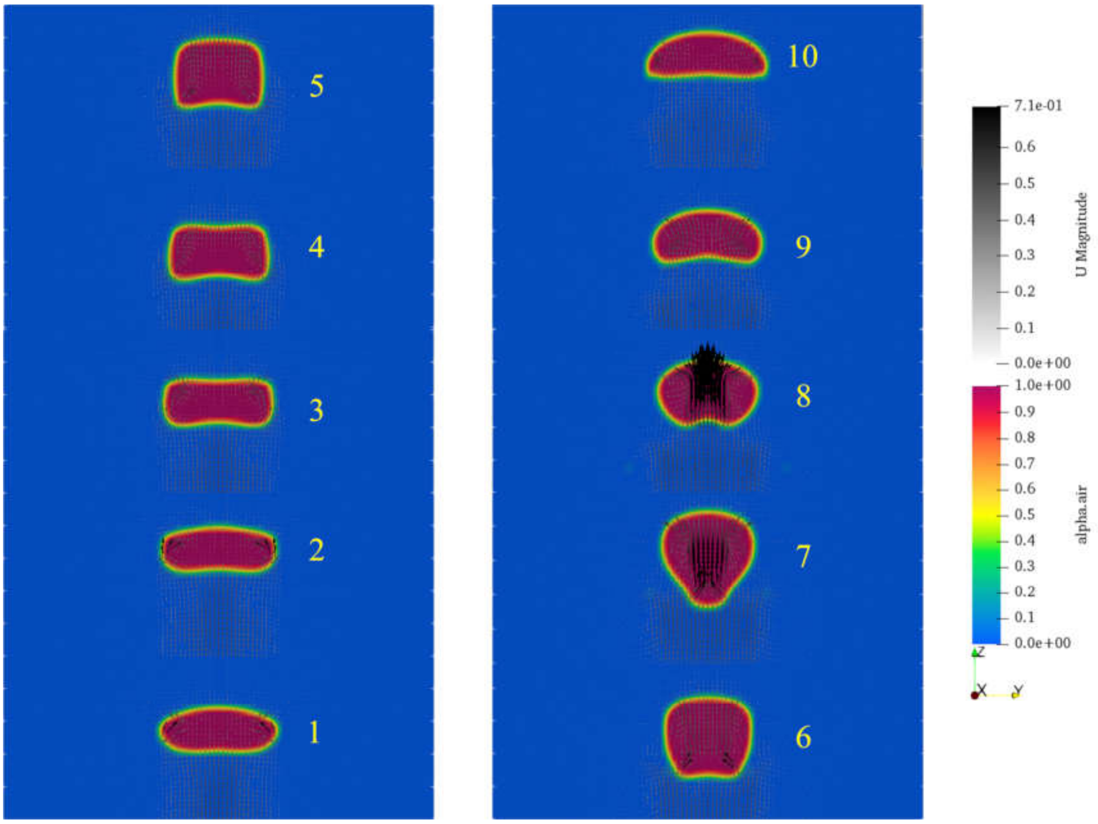

Fig. 4.15. Temporal evolution of bubble internal flow field.

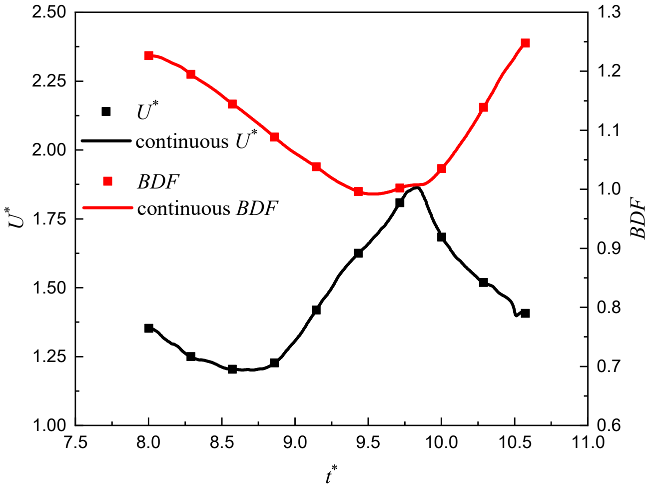

Fig. 4.16. Velocity-shape dependency for a single oscillatory period.

Nevertheless, the velocity-shape dependence observed in experimental studies [92-93] indicates that bubbles with a high aspect ratio typically exhibit a larger rising velocity. This experimental observation seems to contradict the findings from numerical simulations of this thesis. To address the discrepancy between numerical and experimental results, two key aspects need to be revisited: the definition of bubble rising velocity and the effect of bubble motion. According to the previous definition of bubble rising velocity by Eq. (3.35), bubble rising velocity is calculated by the average of bubble internal velocity field. The definition is not directly calculated by the displacement of bubble mass centroid but reflexes the intensity of bubble internal flow field, which could be characterized by a spatial-averaged value. Moreover, considering that bubble rising velocity is recorded at the time scale equal to 10^{-5} s, it could be fully treated as bubble instantaneous velocity. On the contrary, bubble rising velocity in experimental works is measured by the displacement of bubble mass centroid across two incessant images. Therefore, the time scale in this context is dependent on the frequency of high-speed cameras and the time scale is equal to 10^{-3} s ordinarily. Or rather, the experimental rising velocity is featured as a time-averaged rising velocity over a short time period. As for another important aspect, the velocity-shape dependence in Fig. 4.14 appears under the condition where the bubble rises in a straight way approximately, while that in experimental works [92-93] shows the bubble rising with a helical or zigzag path. To achieve a match in conditions between numerical and experimental works, the bubble rising velocity based on the displacement of bubble mass centroid in simulation could be rewritten as

$$U_{\text{cen}}^{*} = \frac{z_{\text{i+1}}^{*} - z_{\text{i}}^{*}}{\Delta t^{*}} \tag{4.1}$$

Since the rising bubble moves inside the three-dimensional space, the time interval is selected to be 4 ms to reduce the random noise. According to the new definition, the velocity-shape dependence is presented in Fig. 4.17. The results are in line with the finding in Fig. 4.14 and confirm the relationship between bubble shape evolution and rising velocity in the presence of a straight bubble trajectory. In particular, when the bubble follows a helical trajectory, the transient bubble rising velocity is found to correlate with bubble deformation partially, which indicate that the dependence is under the influence of bubble motion. Therefore, it can be concluded that the velocity-shape dependence is critically affected by bubble motion. A less deformed bubble shape could beget a higher transient rising velocity under the circumstance of straight bubble trajectory. Otherwise, the velocity-shape dependence is affected by bubble horizontal motion and bubble rising velocity may correlate the temporal bubble shape evolution partially with helical or zigzag bubble trajectory.

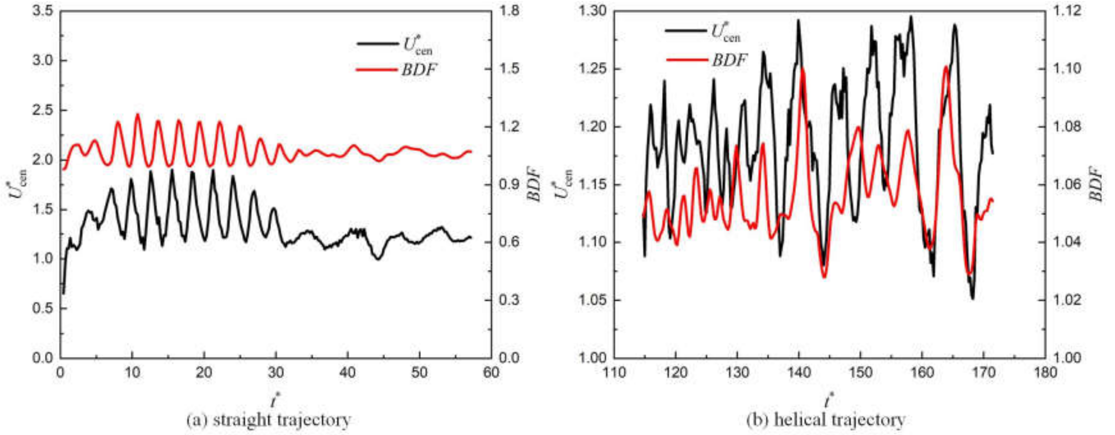

(a) straight trajectory (b) helical trajectory

Fig. 4.17. Velocity-shape dependency in the context of straight and helical trajectories.

4.3 Modeling of bubble terminal interfacial area

According to Tripathi et al. [23], the shape and behavior of bubbles can be classified using *Ga* and *Eo* numbers. These numbers divide the bubble characteristics into five regions, as shown in Fig. 4.18. The dotted line represents the boundary reported by Tripathi et al. [23], while the shaded region represents the investigation range in this thesis, specifically focusing on pool scrubbing conditions. Under pool scrubbing conditions, the rising bubbles can exhibit complex hydrodynamics, transitioning from an axisymmetric regime to an oscillatory regime, and eventually reaching the breakup regime. To establish a correlation for the shaded region in Fig. 4.18, the first step involves examining bubbles within the axisymmetric regime and developing a corresponding correlation. Subsequently, bubbles within the breakup regime are considered to create a correlation suitable for this range. Finally, an effort is made to establish a connection between these two correlations in order to provide a comprehensive description of the bubble terminal interfacial area.

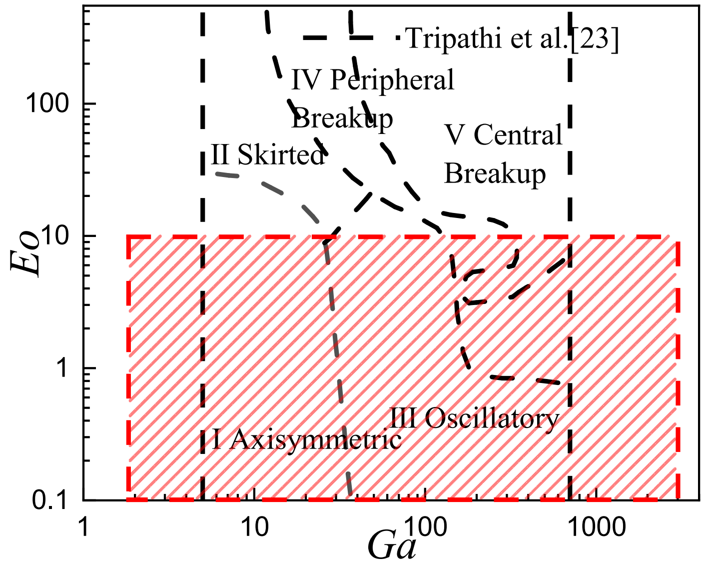

Fig. 4.18. Coverage of *Ga* and *Eo* numbers for curve fittings base on the work [23].

4.3.1 Correlation development in axisymmetric regime

According to the boundary of axissymmetric regime in Fig. 4.18, the gas-liquid surface tension and liquid viscosity in simulation are decided by the dimensionless numbers with bubble size fixed at 6 mm. The simulation time is long enough to achieve the terminal status and other settings are the same as in the previous description. Fig. 4.19 presents the dependence of bubble terminal interfacial area on *Eo* and *Ga* numbers. It can be got that both increasing *Eo* and *Ga* contribute to the increase in bubble interfacial area in a successional way, which shows a good agreement with the presented trend line.

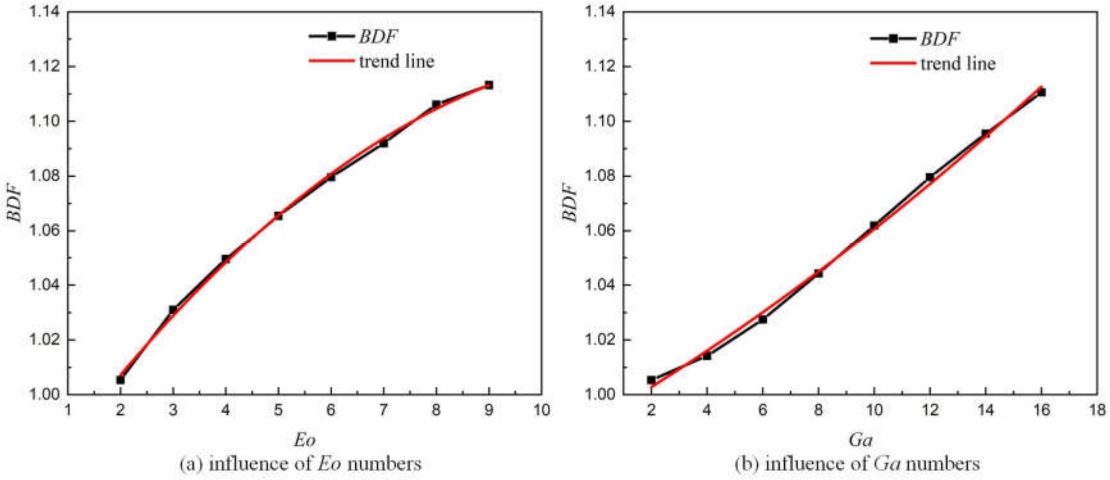

(a) influence of *Eo* numbers
(b) influence of *Ga* numbers

Fig. 4.19. Dependence of bubble interfacial area on *Eo* and *Ga* numbers.

To indicate how bubbles deform with changing *Eo* and *Ga* numbers, Fig. 4.20 shows bubble terminal shape under different conditions. Along two vertical axes, the evolution of bubble terminal shape with *Eo* or *Ga* numbers is illustrated. The starting point is decided by *Eo* and *Ga* numbers both equal to 2. It could be observed that the way how *Eo* and *Ga* numbers affect bubble deformation is dissimilar. With increasing *Eo* numbers, the bubble shape becomes more dimpled, whereas that is prone to persist in an ellipsoidal shape but flattered step by step with increasing *Ga* numbers. The difference in bubble deformation could be clarified from the perspective of force balance. As the bubble comes to terminal status, the principal balance should be an equilibrium between drag and buoyancy forces. Given that bubble size in all cases is identical, the buoyancy force is identical in the bubble rising process. As mentioned in section 2.1, the drag force on the bubble could be decomposed into the pressure drag and the viscous drag. The pressure drag is reliant on the apparent cross-section, whereas the viscous drag is dependent on liquid viscosity and the whole wetted area between two phases [56-57]. As *Eo* numbers increase slightly, the whole wetted area is increased and consequently, the viscous drag is increased. Owing to the presence of force balance, the pressure drag should be reduced in this case, which results in a decrease in the apparent cross-section. To be specific, the bubble front contour becomes curved and presents like a streamlined shape in Fig. 4.20, of which similar observation has also been certified in the experimental work [24]. In terms of increasing *Ga* numbers, even though the whole wetted area is increased, the predominant effect of decreasing liquid viscosity offsets the negative effect, which results in a decrease in viscous drag thereby. To achieve the force balance, the bubble front area is increased, which presents a progressively flatted ellipsoidal shape in Fig. 4.20.

Aside from the specified cases above, the three-dimensional distribution of bubble terminal interfacial versus *Eo* and *Ga* numbers is demonstrated in Fig. 4.21. Overall, all scattered points distribute near a smooth surface. Furthermore, if *Eo* and *Ga* numbers are small enough, the normalized bubble interfacial area approaches one approximately. For the quantitative data-fitting, a presupposed function is hypothesized as

$$BDF = 1 + k_1 \cdot Eo^{k_2} \cdot Ga^{k_3} \tag{4.2}$$

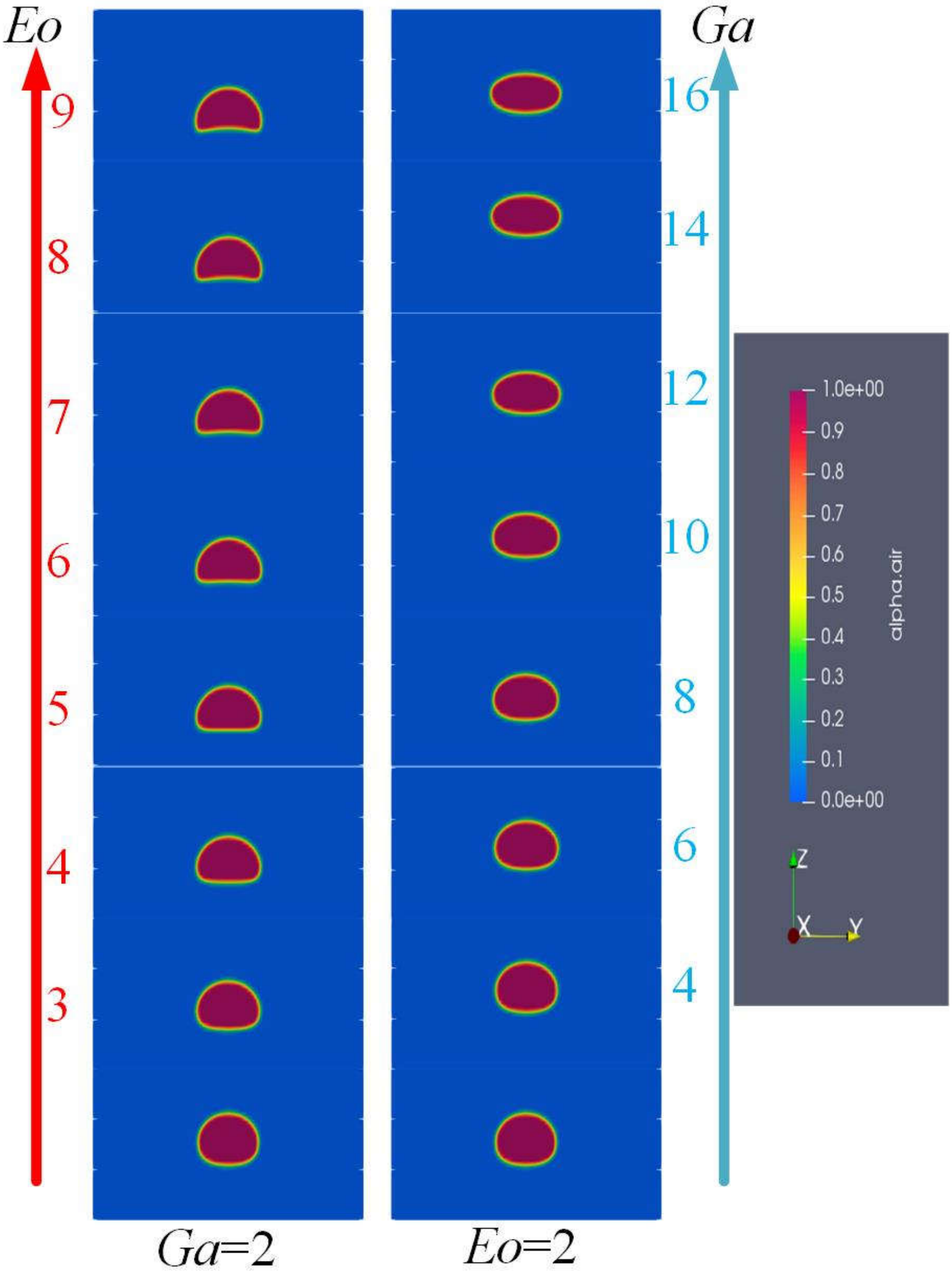

Fig. 4.20. Terminal bubble shape versus *Ga* and *Eo* numbers.

After the fitting from numerical data, an empirical correlation could be determined as

$$BDF = 1 + 0.013 \cdot Eo^{0.63} \cdot Ga^{0.65} \qquad (2 \leq Ga \leq 22, 2 \leq Eo \leq 9) \tag{4.3}$$

To assess the goodness of data-fitting, the criterion, namely *R*-squared is employed as

$$R^2 = 1 - \frac{SSE}{SST} = 1 - \frac{\sum_{\mathrm{i}=1}^{N}(y_\mathrm{i} - \hat{y}_\mathrm{i})^2}{\sum_{\mathrm{i}=1}^{N}(y_\mathrm{i} - \bar{y}_\mathrm{i})^2} \tag{4.4}$$

The calculated *R*-squared is equal to 0.961 and it indicates the present correlation could predict the calculated data precisely. Therefore, it could be summarized that under the circumstance of small *Ga* numbers, both *Eo* and *Ga* numbers could affect bubble interfacial area remarkably and the present empirical correlation could describe bubble terminal interfacial area accurately.

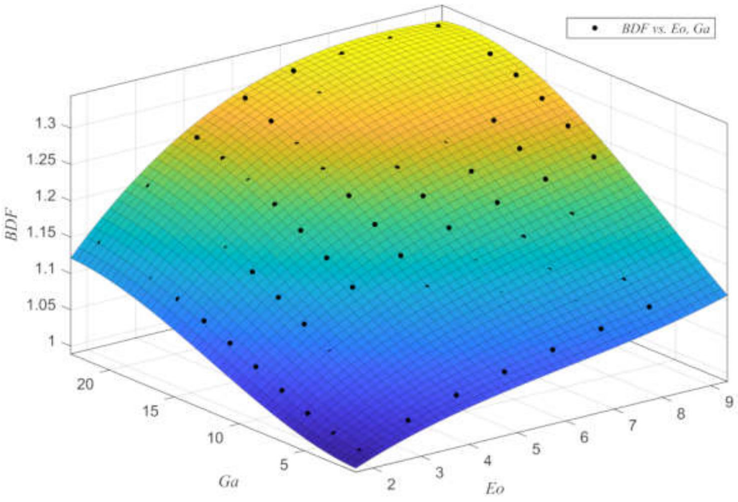

Fig. 4.21. Three-dimensional surface fitting of bubble terminal interfacial area.

4.3.2 Correlation development in oscillatory regime

The cases of bubble rising in the high *Ga* numbers system will be investigated in this section and the critical physical properties are presented in Table 4.3. Based on the combination, a total numerical data set including 48 cases will be built. To reduce the computational load, the *CPD* is adjusted to 18 and the physical time is set to 2 s. Other settings are in line with the previous descriptions. In this section, typical bubble behaviors will be classified based on dimensionless numbers and then bubble breakup dynamics will be particularly analyzed. In the end, the empirical correlation applicable to bubble terminal interfacial area in the high *Ga* numbers system will be developed.

Table 4.3 Physical properties in the high *Ga* system.

physical properties				
Bubble size (mm)	3	4	6	8
Surface tension (N/m)	0.0728	0.055	0.0364	0.0182
Viscosity (mPa·s)	1	0.5	0.25	-

4.3.2.1 Bubble hydrodynamics phenomenon

Fig. 4.22 shows three kinds of bubble behaviors under various dimensionless numbers in the simulation. The results reveal that in the presence of high *Ga* numbers, bubble behaviors could be mainly classified by *Eo* numbers. With small *Eo* numbers, bubbles show a pronounced horizontal displacement and consequently, hit the side boundary. In terms of intermediate *Eo* numbers, bubbles ascend with shape oscillation and the corresponding dynamics has been examined previously. As for large *Eo* numbers, bubbles break up. In relation to bubble impacts on side walls, the assessment of its terminal region will be conducted by extrapolating from the existing numerical data. Regarding the oscillatory bubble, the hydrodynamics have already been examined in section 4.2. The emphasis in this section will be put on bubble breakup because the presence of bubble breakup could affect the upper boundary of the oscillatory regime as indicated in Fig. 4.18.

In particular, bubble breakup dynamics differs among various *Eo* numbers in Fig. 4.22. When *Eo* is equal to 8.62, the central liquid wake penetrates the bubble in the very beginning, while the shape relaxation happens with *Eo* equal to 4.85 before the bubbles break up. Given that bubble breakup dynamics may affect the upper boundary of the developed correlation in this study more or less, the breakup phenomenon will also be elaborated further.

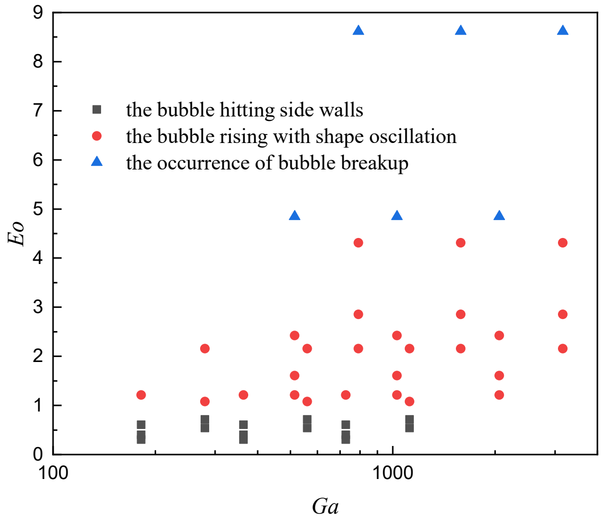

Fig. 4.22. Three observed bubble behaviors in simulation.

To examine the influence of *Eo* numbers on bubble breakup dynamics, a parametric study is conducted with varying *Eo* numbers, while keeping the bubble size fixed at 6 mm. The focus is on the bubble central part where the breakup occurs. In this analysis, the bubble central thickness, δ, is defined as the distance between the top and bottom points of the bubble along the central axis. To make the analysis dimensionless, the normalized form of the bubble central thickness can be expressed as

$$\delta^* = \frac{z_{\mathrm{top}} - z_{\mathrm{bottom}}}{d_{\mathrm{b}}} \tag{4.5}$$

Fig. 4.23 illustrates the temporal evolution of the bubble central thickness. As the bubble undergoes breakup, the central thickness gradually decreases until it reaches zero. For *Eo* equal to 6.5, the bubble ruptures almost immediately. When the *Eo* numbers are reduced from 6 to 5, there is a period of shape relaxation before the bubble eventually breaks up. However, for *Eo* numbers smaller than 4.5, the bubble does not rupture and instead rises with successive shape oscillations.

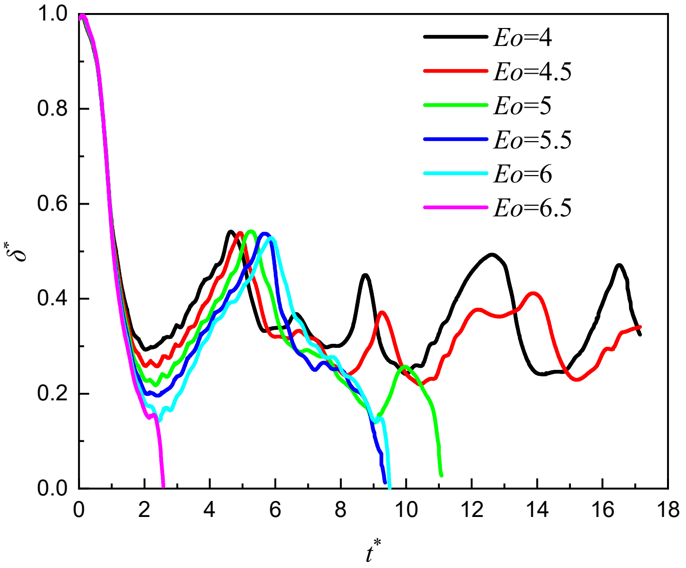

Fig. 4.23. Temporal variation in bubble central thickness.

To assess the degree of bubble deformation, the transient bubble interfacial area before bubble breakup is presented in Fig. 4.24. It is evident that increasing *Eo* numbers lead to a monotonic enhancement in the first oscillatory period of the bubble. Moreover, as the *Eo* numbers vary from 4 to 4.5, the time at which the bubble reaches its maximum deformation during the entire period also changes. Specifically, in Fig. 4.24, this time point is identified at approximately 14 for *Eo* equal to 4, and around 2.5 for *Eo* equal to 4.5. Therefore, it can be concluded that increasing *Eo* numbers not only enhance the initial deformation of the bubble but also shift the occurrence of maximum deformation earlier along the timeline.

According to the above analysis, it could be found that bubble interfacial area could be employed to indicate bubble breakup dynamics aptly because it could delineate bubble deformation accurately, which will be also applied in further analysis. Aside from that, the dependency of bubble breakup dynamics on *Eo* numbers could also be included here concisely. Under the circumstance of small *Eo* numbers, the surface tension force is predominant compared to the gravity force to resist the liquid wake penetrating the bubble. As the bubble approaches the breakup threshold, the increase in *Eo* numbers contributes to the shift of bubble maximum deformation forward to the first oscillatory period. As the bubble's initial deformation is within a certain range, the transition of predominant surface tension force to the gravity force results in the bubble shape relaxation before bubble breakup. The further increase in *Eo* numbers impairs the surface tension force critically, which fails to relax bubble shape to the initial shape in the first oscillatory period. As a consequence, the central breakup appears in the very beginning.

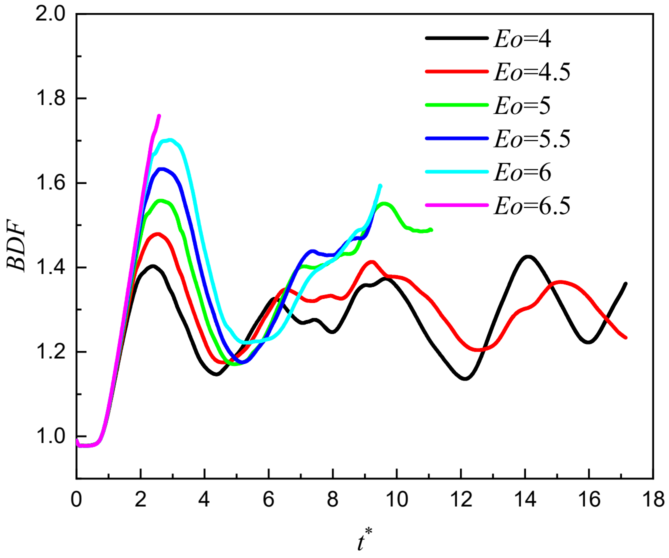

Fig. 4.24. Temporal variation in bubble interfacial area.

4.3.2.2 Bubble breakup

Since bubble interfacial area could be used as a good criterion to feature bubble breakup according to Fig. 4.23 and 4.24, a comparative study for *Eo* between 4.5 and 5 is performed. The dependency between bubble deformation fa ctor and central thickness is demonstrated in Fig. 4.25 and 4.26. The results reveal that the increase in *BDF* leads to the decreasing δ^*, which embodies an anti-phase trend in general. Notwithstanding, an in-phase dependency is also observed in Fig. 4.25 and 4.26 as t^* varies from 8 to 11. The in-phase dependency indicates a special bubble shape evolution pattern, which is that the peripheral part of the whole bubble relaxes toward the round shape, whereas the central part becomes protruding with the gradually decreased thickness.

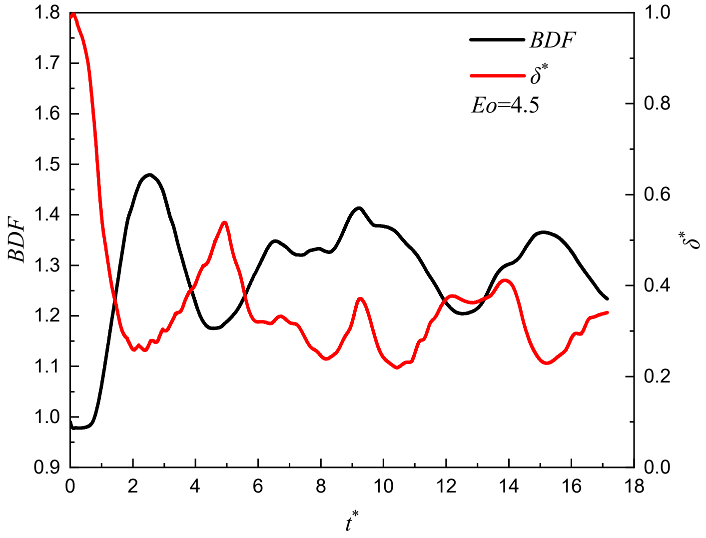

Fig. 4.25. Relationship between bubble deformation factor and central thickness with *Eo*=4.5.

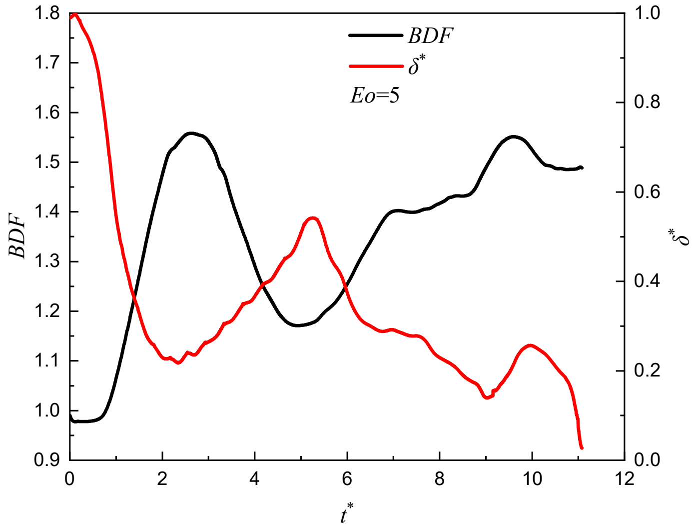

Fig. 4.26. Relationship between bubble deformation factor and central thickness with *Eo*=5.

To account for how the bubble evolves its shape, Fig. 4.27 and 4.28 shows the transient bubble shape and flow field. The temporal evolution processes between two cases are quite similar but with *Eo* equal to 5, the bubble turns out to be a more deformed shape compared to that with *Eo* equal to 4.5. In terms of both cases, the initial bubble shape is defined as spherical. When the bubble begins to rise owing to buoyancy force, bubble shape deforms followed by an increasing curvature of bottom surface. At a certain timepoint, the surface tension force on the bubble based on Eq. (3.3) is large enough to counteract the driving force from the liquid wake, which gives rise to the occurrence of bubble shape relaxation. The process could be observed at t^* from 6.29 to 9.72 in Fig. 4.27 and 4.28. In particular, given that the bubble with *Eo* equal to 5 shows a thinner shape, the bubble's bottom surface may touch the bubble's upper surface in the shape evolution process and consequently, the bubble breakup happens at t^* from 10.29 to 11.43 in Fig. 4.28. On the contrary, the bubble with *Eo* equal to 4.5 presents a less deformed shape and could rise continuously in Fig. 4.27.

In light of the above analysis, the phenomenon of shape relaxation before bubble breakup could be clarified systematically. As discussed before, with the increasing *Eo* numbers, the maximum bubble deformation of the whole rising process may be brought forward along the timeline, which is also followed by a key transition of predominant force from the surface tension force to the gravity force in bubble shape evolution. Owing to the gravity-driven effect, the liquid wake develops in a rapid manner and gives rise to a largely distorted bubble bottom surface within the first shape oscillatory period. Under the circumstance, if the surface tension force could offset the driving force from the liquid wake, bubble shape relaxation will happen. Otherwise, the bubble may break up in the beginning. In the successional bubble shape evolution process, the bubble's bottom surface may touch the bubble's upper surface at some transitional *Eo* numbers due to a highly deformed shape, which causes the bubble breakup hereafter.

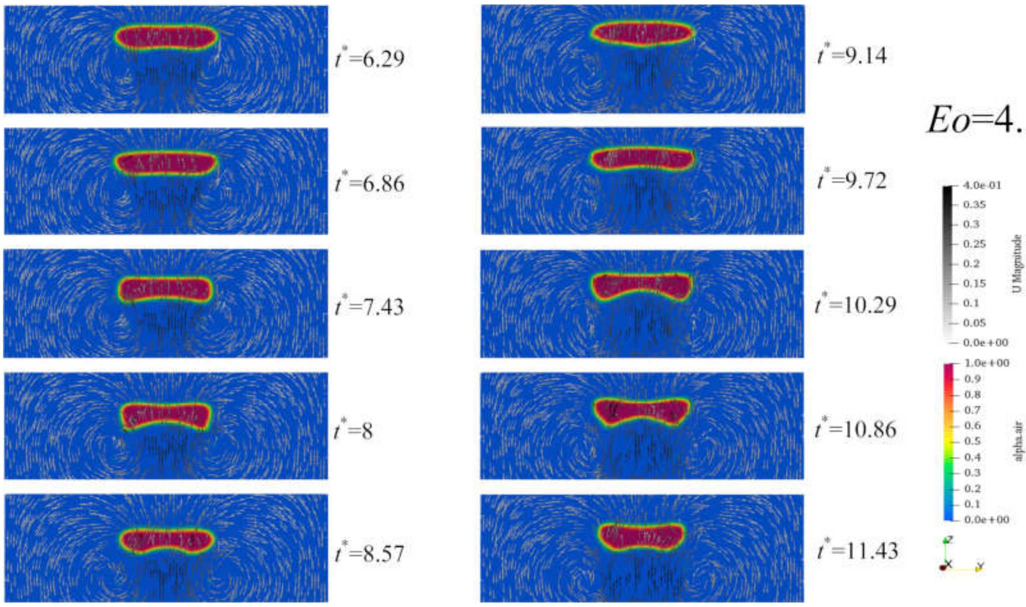

Fig. 4.27. Transient bubble shape evolution with *Eo* equal to 4.5.

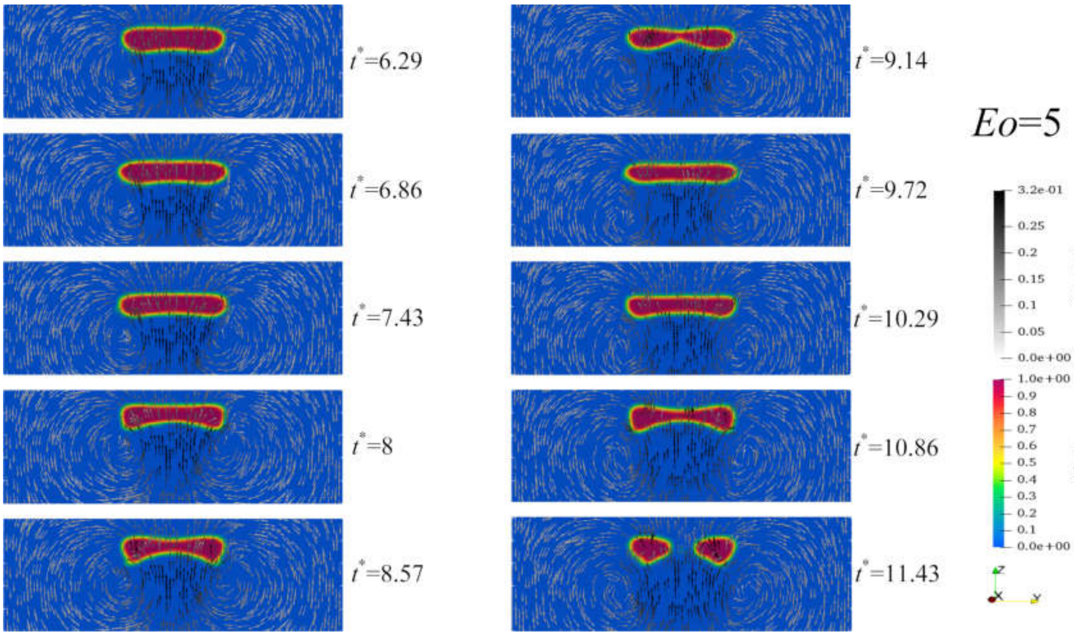

Fig. 4.28. Transient bubble shape evolution with *Eo* equal to 5.

The process of the three-dimensional bubble breakup process is exhibited in Fig. 4.29. Regarding *Eo* numbers equal to 5.5, 6 and 6.5, symmetrical breakup behaviors are observed and the bubble disintegration is accompanied by four pinch-off points. The symmetrical characteristics are in line with the previous studies [94-95]. Aside from that, an asymmetrical breakup manner is found with *Eo* equal to 5. Only one pinch-off point is present and subsequently, two unequal daughter bubbles are generated. Given that the asymmetrical breakup only appears in the context of small *Eo*, it may originate from the influence of surface tension force, which results in the imbalance of planar forces on the bubble surface.

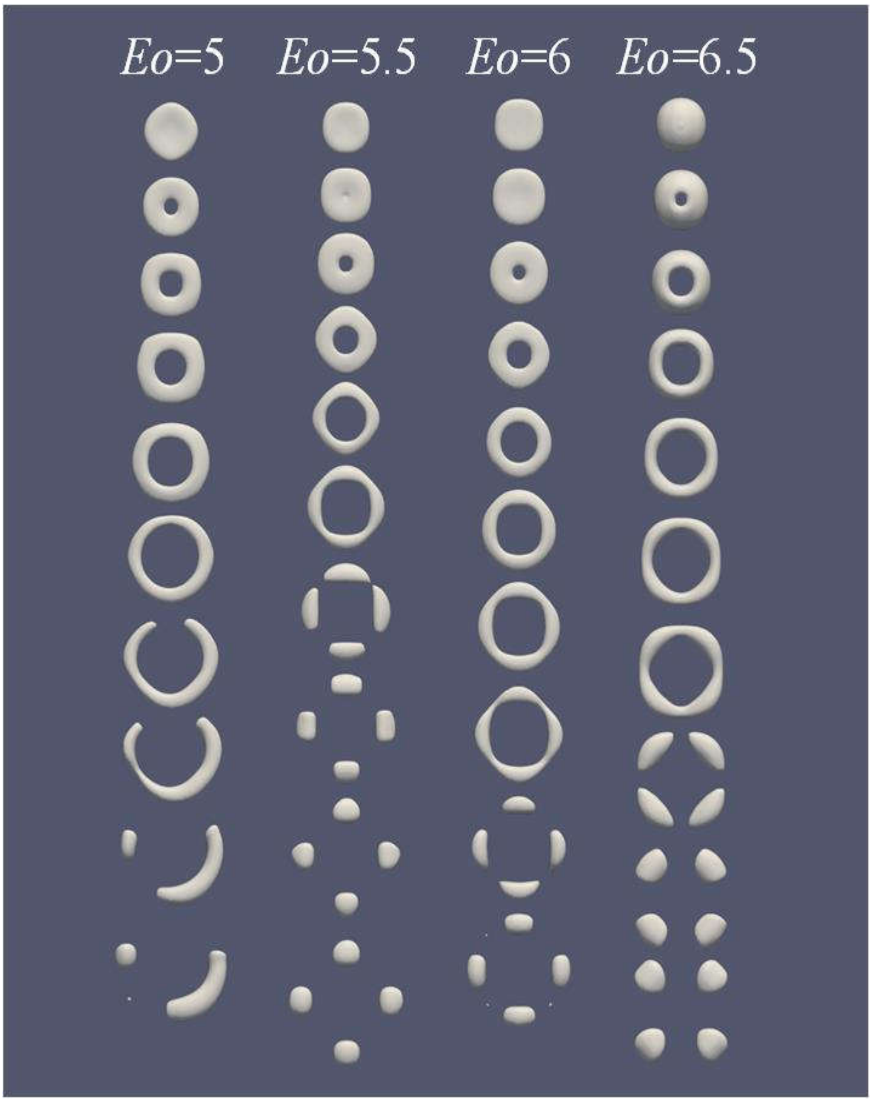

Fig. 4.29. Three-dimensional bubble breakup process.

Although bubble breakup is chiefly influenced by *Eo* numbers as indicated in Fig. 4.22, the dependency of *Ga* numbers on bubble breakup is still checked to quantify this influence. A parametric study is performed as shown in Fig. 4.30. Specifically, the increase in *Ga* numbers lowers down the breakup threshold of *Eo* numbers, which is consistent with the previous studies [23]. Based on the phase plot, a weak influence of *Ga* numbers on bubble breakup is found. The weak relationship could be interpreted by the energy dissipation by the viscous liquid. In the context of small *Ga* numbers, the portion of energy dissipation between gas and liquid phases is pretty remarkable, which deteriorates the development of liquid wake. Consequently, bubble breakup is hindered and the bubble could form a skirted shape eventually [23]. As for high *Ga* numbers in this section, since the viscous energy dissipation is rather limited, its influence on breakup dynamics is also restrained, which manifested as the weak dependence in Fig. 4.22. Aside from that, the occurrence of bubble breakup is typically followed by the bubble maximum deformation. To summarize the interrelationship thoroughly, Fig. 4.31 exhibits how bubble maximum deformation is linked to bubble breakup. Under various *Eo* numbers, two explicit thresholds of *BDF* are found to distinguish different breakup dynamics accordingly, which could be identified at 1.52 and 1.72 in given conditions, respectively. The results in Fig. 31 certify the fact that bubble three-dimensional interfacial area is a key influential factor to affect bubble breakup, which could also be used to characterize bubble breakup dynamics in a pinpoint way.

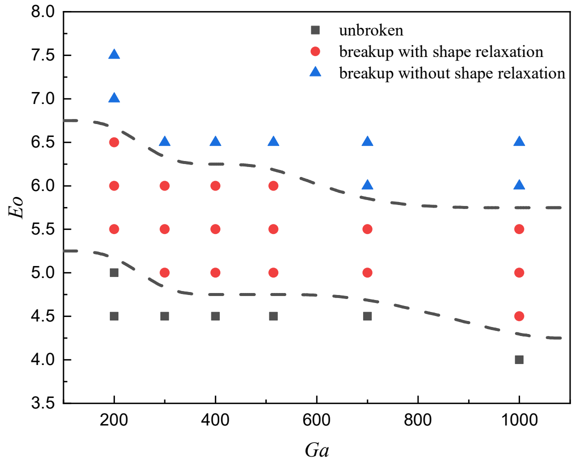

Fig. 4.30. Phase plot of bubble breakup behaviors.

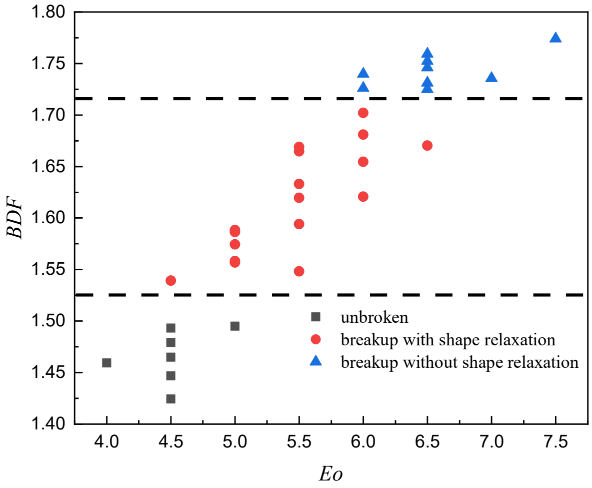

Fig. 4.31. Relationship between bubble maximum deformation and bubble breakup behaviors.

4.3.2.3 Correlation development

The time-averaged values of the bubble's terminal interfacial area under various conditions are presented in Table 4.4. Utilizing the numerical data from Table 4.4, the impact of *Ga* and *Eo* numbers on the bubble's terminal interfacial area is summarized in Fig. 4.32. It can be observed that, despite *Ga* numbers spanning a wide range from 100 to 1500, their overall influence on the bubble's terminal interfacial area is generally insignificant. Conversely, the bubble's terminal interfacial area exhibits a strong dependency on *Eo* numbers, steadily increasing as *Eo* numbers rise. Considering the findings depicted in Fig. 4.32, it is possible to presume the existence of an artificial function solely linked to *Eo* numbers for the purpose of simplification as

$$BDF = 1 + k_1 \cdot Eo^{k_2} \tag{4.6}$$

Table 4.4 Terminal interfacial area in the high *Ga* system.

d_b (mm)	*Eo*	*Ga*	*BDF*	d_b (mm)	*Eo*	*Ga*	*BDF*
3	0.3	181.87	-	6	1.21	514.39	1.07
3	0.3	363.73	-	6	1.21	1028.79	1.069
3	0.3	727.46	-	6	1.21	2057.57	1.071
3	0.4	181.87	-	6	1.6	514.39	1.091
3	0.4	363.73	-	6	1.6	1028.79	1.092
3	0.4	727.46	-	6	1.6	2057.57	1.091
3	0.61	181.87	-	6	2.42	514.39	1.136
3	0.61	363.73	-	6	2.42	1028.79	1.122
3	0.61	727.46	-	6	2.42	2057.57	1.125
3	1.21	181.87	1.071	6	4.85	514.39	×
3	1.21	363.73	1.069	6	4.85	1028.79	×
3	1.21	727.46	1.07	6	4.85	2057.57	×
4	0.54	280	-	8	2.15	791.96	1.094
4	0.54	560	-	8	2.15	1583.92	1.099
4	0.54	1120	-	8	2.15	3167.84	1.092
4	0.71	280	-	8	2.85	791.96	1.17
4	0.71	560	-	8	2.85	1583.92	1.165
4	0.71	1120	-	8	2.85	3167.84	1.182
4	1.08	280	1.062	8	4.31	791.96	1.211
4	1.08	560	1.062	8	4.31	1583.92	1.243
4	1.08	1120	1.059	8	4.31	3167.84	1.222
4	2.15	280	1.116	8	8.62	791.96	×
4	2.15	560	1.115	8	8.62	1583.92	×
4	2.15	1120	1.118	8	8.62	3167.84	×

"-" refers to the bubble hitting the side wall; "×" refers to the occurrence of bubble breakup.

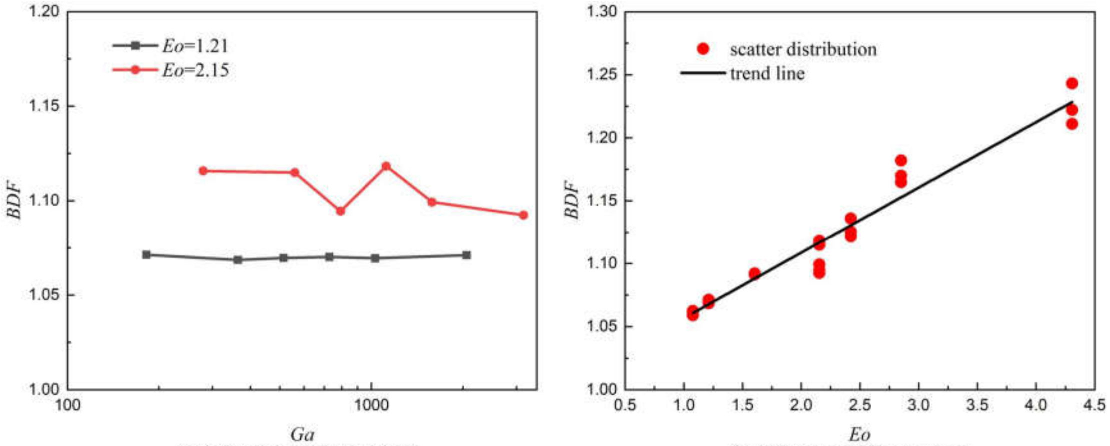

(a) influence of *Ga* numbers
(b) influence of *Eo* numbers

Fig. 4.32. Dependency of bubble terminal interfacial area on *Ga* and *Eo* numbers.

By fitting the numerical data from Table 4.4, the coefficients k_1 and k_2 are determined to be 0.056 and 0.96, respectively. When considering the applicable scale of this empirical correlation, it is important to note that the previous assumption was based on high *Ga* numbers. Therefore, the lower boundary for *Ga* numbers is suggested to be *Ga*>200, as indicated by the data in Table 4.4.

On the other hand, determining the boundary for Eo numbers is more challenging due to the weak dependence of Ga numbers on bubble breakup. However, based on the phase plot shown in Fig. 4.30, a rough approximation suggests Eo<4.5 as the condition. Taking this into account, an empirical correlation can be formulated as follows

$$BDF = 1 + 0.056 \cdot Eo^{0.96} \qquad (Ga > 200, Eo < 4.5) \tag{4.7}$$

To evaluate how good the fitness is, the previous R-squared criterion in Eq. (4.4) is employed and its size is equal to 0.951 after calculation, which indicates that the predicted data based on Eq. (4.7) could match the numerical data well.

The experimental data of bubble terminal interfacial area [63] is adopted to compare with the predicted data from Eq. (4.7) as shown in Fig. 4.33. The predicted data of intermediate bubbles in Fig. 4.33 agrees well with the experimental data, whereas a significant discordance is found for the large bubble equal to 9.6 mm roughly. The cause of the discordance may potentially originate from the infringement of the predefined axisymmetric assumption of surface area calculation in the experimental study [63]. As indicated in the study [96], the bubble loses the fore-and-aft symmetry apparently as bubble aspect ratio is higher than 2.5 in the air-water system. Notwithstanding a stereo bubble morphology is difficult to be reconstructed from experimental works, a typical 9 mm bubble with irregular and asymmetrical contour has been observed via the high-speed camera in the work [55], whose aspect ratio is larger than 2.5. Therefore, in the presence of asymmetrical characteristics, the previous assumption could be over-simplistic to calculate the surface area of large bubbles in experimental studies. Apart from that, as the bubble loses symmetry, the erratic shape deformation may affect the observed shape from different directions, which may introduce further errors in image post-processing [10, 60]. Given that two pivotal influential factors are involved for large bubbles, a large measurement uncertainty may exist in experimental works, which may result in a considerable deviation between predicative and experimental results.

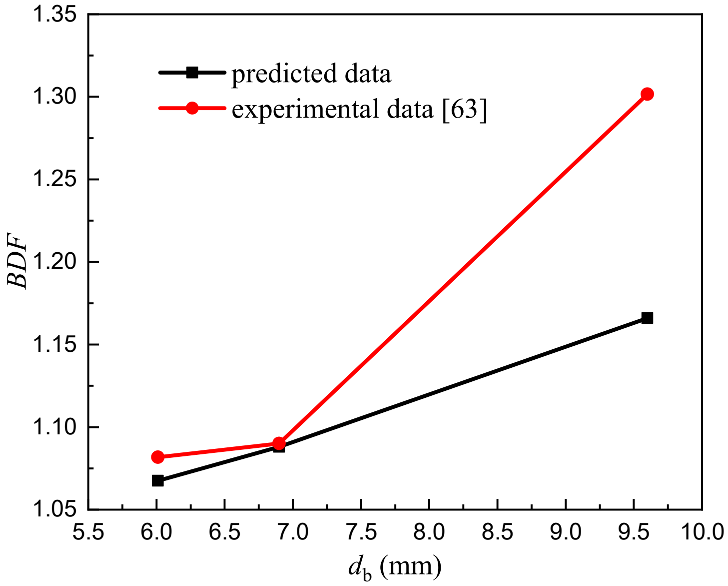

Fig. 4.33. Comparison between predicted and experimental data.

To prove the feasibility of the proposed correlation, Eq. (4.7) is compared to the previous correlation in the work [22], which could be written as

$$BDF = 1 + 0.07 \cdot (E - 1)^{7/4} \tag{4.8}$$

In Eq. (4.8), bubble aspect ratio is required for the estimation of three-dimensional interfacial area. For comparison, the experimental data [55] including bubble aspect ratio and other foundational information is selected to predict the bubble interfacial area via Eq. (4.7) and (4.8). Fig. 4.34 shows the comparison results, which reveal a dramatic underestimation by Eq. (4.8) for large bubbles. It should be emphasized here that Eq. (4.8) is developed under the circumstance of the low *Ga* system, where the bubble could maintain a symmetrical terminal shape and straight bubble path. As it is applied in the high *Ga* number system, the irregular bubble deformation deteriorates the applicability largely. On the contrary, Eq. (4.7) could manifest the correct trend that the normalized bubble interfacial area increases monotonically with the increasing bubble size. Furthermore, as surface tension goes through a slight variation due to temperature change, the measured aspect ratio could be quite different based on the work [55], which affects the predictive curve accordingly. It seems that the application of Eq. (4.8) in the high *Ga* system may present a large uncertainty because of the wobbling nature of bubbles. By contrast, the association of bubble interfacial area with gas-liquid properties seems to be a better alternative compared to bubble aspect ratio as shown in Fig. 4.34. At any rate, according to the above comparisons with experimental data and empirical correlation, the feasibility of the proposed correlation has been confirmed in the high *Ga* system except for large bubbles.

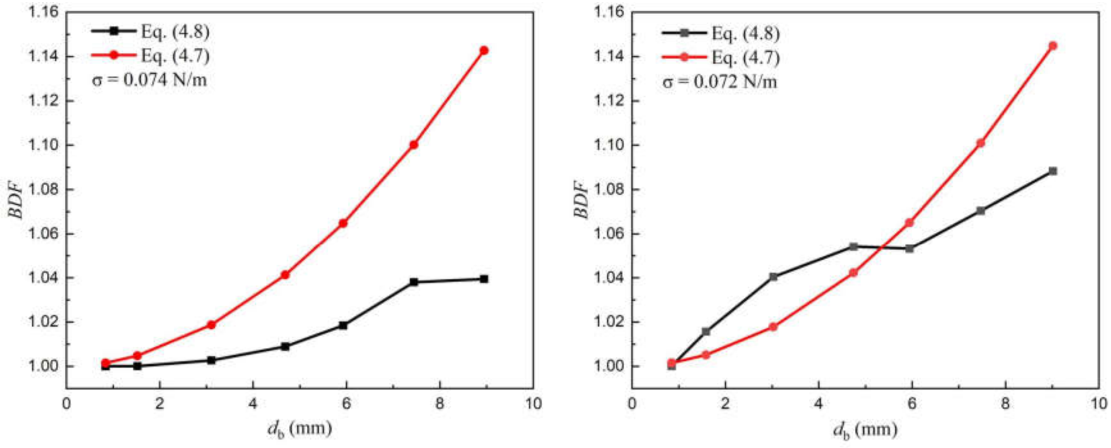

(a) water temperature 8 ℃

(b) water temperature 29 ℃

Fig. 4.34. Comparison of empirical correlations with water temperature equal to 8 and 29 °C.

4.3.3 A comprehensive description of bubble terminal interfacial area

In order to establish a connection between Eq. (4.3) and Eq. (4.7), further simulations are conducted in the transitional range of *Ga* numbers. Considering the applicable range specified in both equations, the simulations are carried out with *Ga* numbers ranging from 22 to 200 and *Eo* numbers ranging from 1 to 4. The bubble size is kept constant at 6 mm, and the simulation duration is extended to ensure that the bubble reaches a quasi-stable stage. Other settings remain the same as previously discussed. It is found that as *Eo* numbers increase, the bubble interfacial area will subsequently increase, as analyzed earlier. Therefore, the focus of this section will be on examining the influence of *Ga* numbers on the transient and terminal bubble interfacial area, as it is selected from the transitional range.

Fig. 4.35 illustrates the impact of *Ga* numbers on the transient interfacial area of bubbles. As *Ga* numbers fall within the transitional range, variations in *Ga* numbers lead to a transition from stable bubbles to unstable bubbles. Once bubbles lose their stable terminal shape, their terminal interfacial area decreases accordingly, as depicted in Fig. 4.35. These results indicate that increasing *Ga* numbers have a negative effect on the bubble interfacial area within the transitional range.

Fig. 4.36 displays the relationship between the bubble's terminal interfacial area and *Ga* numbers. The calculated data falls within the predicted range obtained from Eq. (4.3) and Eq. (4.7), which also exhibit a general decreasing trend. These results confirm the previous argument regarding the negative effect of increasing *Ga* numbers on the terminal interfacial area of bubbles within the transitional range. The overall calculated data for all cases are summarized in Table 4.5.

Similar to the form of Eq. (4.2), after the data-fitting from all available data in Table 4.5, the bubble terminal interfacial area in the given range could be presented as

$$BDF = 1 + 0.106 \cdot Eo^{0.79} \cdot Ga^{-0.07} \qquad (22 < Ga \leq 200, Eo < 4.5) \tag{4.9}$$

The calculated *R*-squared of Eq. (4.9) is equal to 0.947 and the goodness is satisfied. With the combination of Eq. (4.3), (4.7) and (4.9), a comprehensive correlation to describe bubble three-dimensional terminal interfacial area with an extensive coverage of gas-liquid properties could be determined finally as

$$BDF = \begin{cases} 1 + 0.013 \cdot Eo^{0.63} \cdot Ga^{0.65} & (2 \leq Ga \leq 22, 2 \leq Eo \leq 9) \\ 1 + 0.106 \cdot Eo^{0.79} \cdot Ga^{-0.07} & (22 < Ga \leq 200, Eo < 4.5) \\ 1 + 0.056 \cdot Eo^{0.96} & (Ga > 200, Eo < 4.5) \end{cases} \tag{4.10}$$

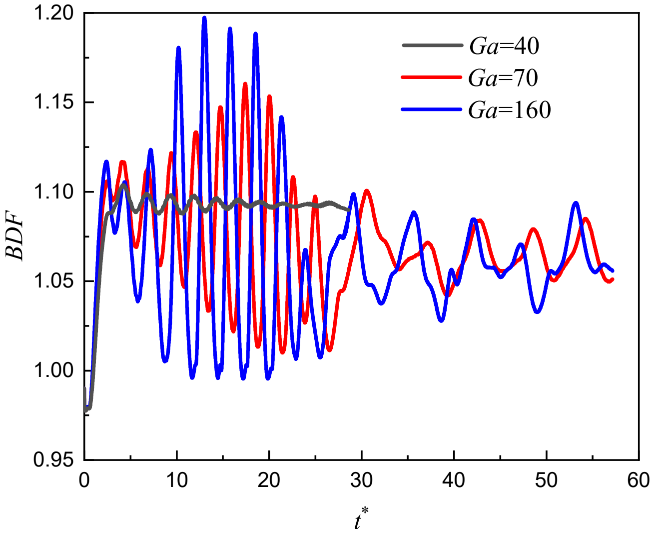

Fig. 4.35. Bubble transient interfacial area with *Eo* equal to 1.

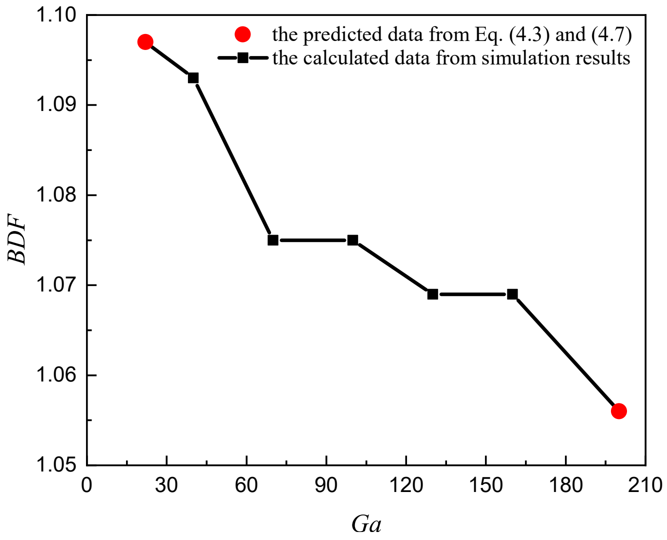

Fig. 4.36. Bubble terminal interfacial area with *Eo* equal to 1.

Table 4.5 Bubble terminal interfacial area under different conditions.

Ga	*Eo*	*BDF*	*Ga*	*Eo*	*BDF*
22	1	1.097*	100	3	1.169
22	2	1.15*	100	4	1.237
22	3	1.194*	130	1	1.069
22	4	1.232*	130	2	1.135
40	1	1.093	130	3	1.178
40	2	1.145	130	4	1.236
40	3	1.205	160	1	1.069
40	4	1.272	160	2	1.147
70	1	1.075	160	3	1.179
70	2	1.124	160	4	1.219
70	3	1.156	200	1	1.056*
70	4	1.211	200	2	1.109*
100	1	1.075	200	3	1.161*
100	2	1.135	200	4	1.212*

"*" refers to the data predicted by Eq. (4.3) or (4.7).

4.4 Conclusion

In this chapter, a comprehensive correlation is proposed to predict bubble terminal interfacial area. The methodology to extract bubble interfacial in simulation is calibrated and evaluated by experimental data at first and long-term bubble dynamics is examined thoroughly and systematically. In summary, the main conclusions are epitomized here as

(1) The interfacial sharpening scheme is a pivotal factor to affect bubble interfacial area because the attainment of terminal interfacial area requires a sharp interfacial region rigidly. In contrast with MULES scheme [85], isoAdvector scheme [86] is found to be more appropriate for the quantitative modeling of single bubble interfacial area.

(2) As for long-term bubble dynamics, the presence of vortex shedding affects the momentum transfer from gas phase to liquid phase and subsequently, influences bubble motion significantly.

When the bubble presents a wobbling motion, the temporal evolution of bubble interfacial area and rising velocity could be mainly characterized by the damped oscillatory stage and the quasi-stable stage.

(3) A velocity-shape dependence is found and affected by bubble motion critically. A less deformed bubble shape could beget a higher transient rising velocity under the circumstance of straight bubble trajectory. Otherwise, the velocity-shape dependence is influenced by bubble horizontal motion and bubble rising velocity may correlate the temporal bubble shape evolution partially with helical or zigzag bubble trajectory.

(4) With the successional evolution of Galilei numbers, a comprehensive correlation is developed based on the process of data-fitting, which could be written as

$$BDF = \begin{cases} 1 + 0.013 \cdot Eo^{0.63} \cdot Ga^{0.65} & (2 \leq Ga \leq 22, 2 \leq Eo \leq 9) \\ 1 + 0.106 \cdot Eo^{0.79} \cdot Ga^{-0.07} & (22 < Ga \leq 200, Eo < 4.5) \\ 1 + 0.056 \cdot Eo^{0.96} & (Ga > 200, Eo < 4.5) \end{cases}$$

In this correlation, bubble interfacial area is found to increase with Eötvös numbers monotonically over the whole range, whereas the effect of Galilei numbers is dependent on its physical size.

With low Galilei numbers from 2 to 22, bubbles could maintain a stable terminal shape and force balance between buoyancy force and drag force. The increase in Galilei numbers results in decreasing liquid viscosity and decreases the viscous drag accordingly. Under the circumstance of force balance, the pressure drag is increased followed by an increasing bubble front area. As a consequence, the bubble exhibits a gradually flatted ellipsoidal shape and increasing terminal interfacial area, which corresponds to the positive coefficient in the correlation.

With intermediate Galilei numbers from 22 to 200, bubbles may go through the transition from stable bubbles to unstable bubbles. Once the bubble loses a stable terminal shape, its terminal interfacial area may decrease with increasing Galilei numbers as a result of bubble shape oscillation. Therefore, the index of Galilei numbers in the correlation is negative.

With high Galilei numbers more than 200, bubble interfacial area is insensitive to Galilei numbers. As for bubble breakup, the size of Galilei numbers in this case is at least two orders larger than that of Eötvös numbers, which mitigate the effect of Galilei numbers on bubble breakup largely. Correspondingly, the linked index of the correlation is given to zero in the high Galilei system.

Additionally, bubble breakup dynamics are also checked briefly because it may partly relate to the upper boundary of the developed correlation. Bubble interfacial area is found to be an appropriate criterion to characterize bubble breakup dynamics because it could delineate three-dimensional bubble deformation accurately. As an important reference, a phase diagram is plotted to indicate the dependency of bubble breakup on Galilei and Eötvös numbers, which contribute to the determination of the upper boundary eventually.

5 Particle Motion inside Bubbles

In this chapter, we calibrate and evaluate the developed interfacial penetration model using the experimental data of aerosol decontamination with a single bubble [25]. Once the authenticity of the model is confirmed, we examine the motion of particles in the gas phase and conduct a parametric study to identify influential factors in the particle interfacial process. We then investigate the impact of bubble dynamics on aerosol transport behaviors and delve into particle deposition mechanisms. Furthermore, we introduce a residence-time distribution analysis for the aerosol decontamination process, exploring relevant parameters comprehensively. Based on these findings, we investigated aerosol mean residence time accordingly.

5.1 Validation of interfacial penetration model based on experimental data

As discussed previously, the interfacial penetration model is derived from the theoretical analysis and thus the threshold of We_p criterion should be calibrated based on the experimental data. Particularly, most priori experimental studies [26, 32, 34] reported the condition of aerosol decontamination under the circumstance of bubbly flow. Nevertheless, it is widely recognized that the bubble will accelerate in the wake of the leading bubble [97-99], which will introduce additional complexity and uncertainty in the analysis of both bubble dynamics and aerosol decontamination. Moreover, the external flow force could also be one of the crucial factors to affect aerosol transport through the rising bubble as indicated by Friedlander et al. [100]. Therefore, the single bubble scrubbing aerosol experiment [25] is selected as the key benchmark experiment in this work. Since the experimental method [25] is largely different from that in previous studies and not widely recognized at present, the detailed experimental procedure is introduced systematically for better comprehension.

The general experimental setup [25] is illustrated in Fig. 5.1. As shown in Fig 5.1 (a), the vessel dimensions are 0.34×0.34×1.5 m^3, and a syringe connected to an L-shaped nozzle is positioned at the bottom of the vessel for injecting aerosol-laden gas into the liquid. The experiment is conducted under conditions of a relatively slow flow rate, ensuring the rise of a single bubble in quiescent water. Upon reaching the liquid surface, the bubble ruptures, and the remaining aerosols are captured by a sampling nozzle for subsequent analysis using an aerosol spectrometer.

Notwithstanding the outlet aerosol concentration could be got via the aerosol spectrometer, the inlet concentration of the initial bubble remains indeterminate. Given that the inlet aerosol concentration couldn't be measured explicitly, the luminance information of the initial bubble is recorded by the high-speed camera to attain the inlet aerosol concentration in an implicit way as shown in Fig. 5.1 (b). Two typical images at the moment of bubbles detaching the nozzle are presented in Fig. 5.1 (b), which also indicates that the inclusion of aerosol inside the bubble tends to low down the luminance compared to the bubble without aerosol because of the scattering of backlight via the aerosol [25]. Through the dependency, the relationship between aerosol concentration and normalized luminance is exhibited in Fig. 5.1 (c), whereby the aerosol decontamination and initial aerosol size distribution could be measured.

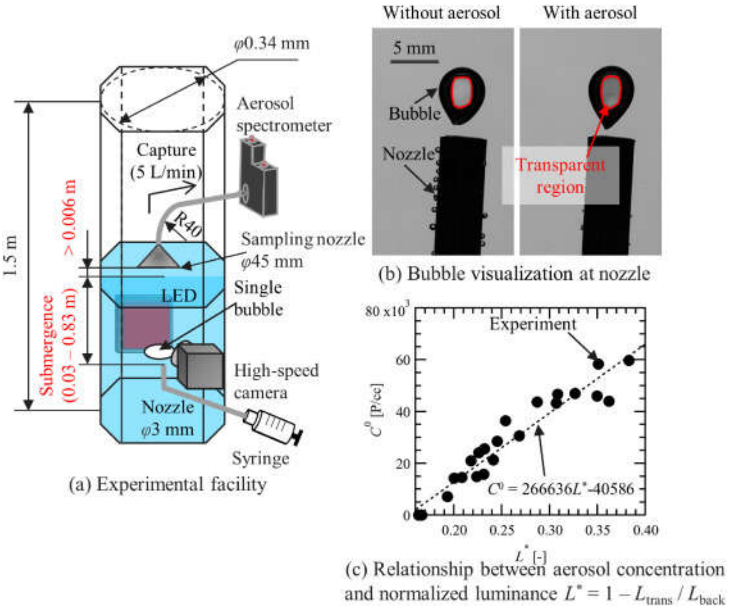

(a) Experimental facility

(b) Bubble visualization at nozzle

(c) Relationship between aerosol concentration and normalized luminance $L^* = 1 - L_{\text{trans}} / L_{\text{back}}$

Fig. 5.1. Experimental setup of the single bubble experiment by Fujiwara et al. [25].

In terms of the calibration of the interfacial penetration model, bubble size is set to be 5 mm and initial bubble shape is assumed to be spherical according to Fig. 5.1 (b). The initial aerosol number is defined as 4000 according to the experiment [25]. Given that there exists aerosol size distribution in the experiment [25], particle size distribution in simulation is set accordingly as shown in Fig. 5.2.

For comparison, we also considered the criterion used in previous studies. Wang et al. [12] used particle impact velocity as a criterion to determine different particle interfacial behaviors when a single particle hits the stagnant interface. They found that this criterion's threshold varies only when the particle size crosses several microns. According to Fig. 5.2, since the particle size distribution falls within one micron, we selected this criterion to test its applicability in more complex conditions, such as the bubble scrubbing process. Additionally, we included a condition called as fast removal, where no criterion was applied for comparison. Fig. 5.3 shows the comparison results of different interfacial criteria. In the case of fast removal in Fig. 5.3 (a), the aerosol is decontaminated rapidly, which significantly deviates from the experimental observation [25]. By contrast, when the velocity criterion or particle Weber criterion is applied, a conditional agreement is observed, with the threshold values of $u_{\text{p,n}}$=0.21 m/s or We_{p}=3×10^{-4} approximately.

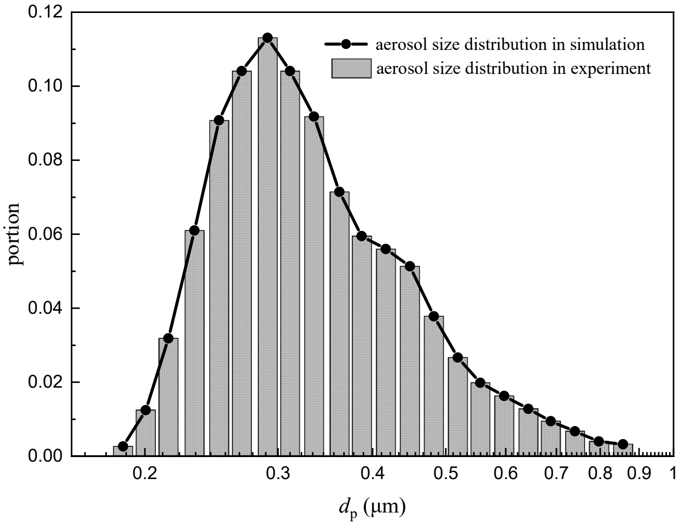

Fig. 5.2. Aerosol size distribution in experiment [25] and in simulation.

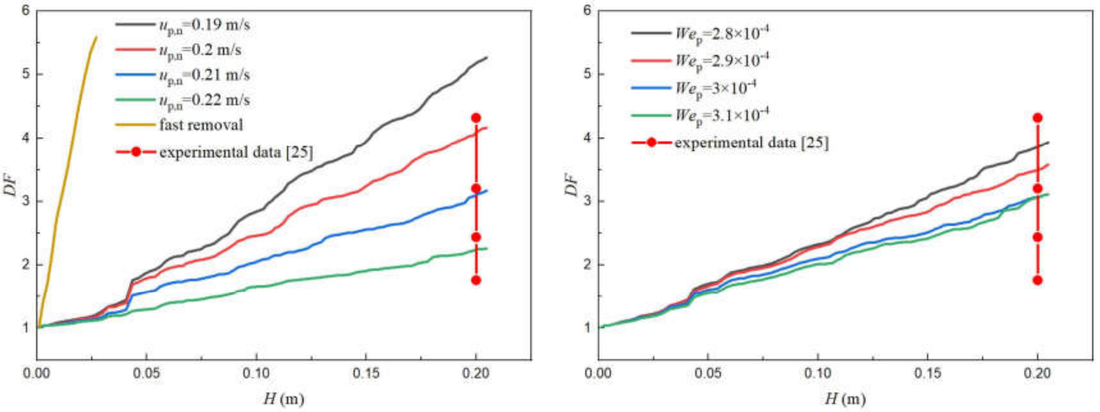

(a) other interfacial criteria

(b) particle Weber number

Fig. 5.3. Comparison of different criteria based on the benchmark data.

The analysis of the aerosol size distribution in these two cases is presented in Fig. 5.4. Despite the similar terminal decontamination factor observed between the two cases in Fig. 5.3, the resulting terminal aerosol size distributions are noticeably different. When considering the $u_{p,n}$ criterion, the terminal aerosol size distribution remains similar to the initial aerosol size distribution. Conversely, a significant alteration is observed when using the We_p criterion. It is well-known that during the process of aerosol-laden gas through a liquid pool, larger aerosol particles are effectively removed, while smaller aerosol particles may be released into the environment. This pool scrubbing process leads to a considerable variation in the aerosol size distribution at the outlet. Under pool scrubbing conditions, the We_p criterion proves to be a better criterion compared to the $u_{p,n}$ criterion, aligning with experimental findings from a qualitative standpoint.

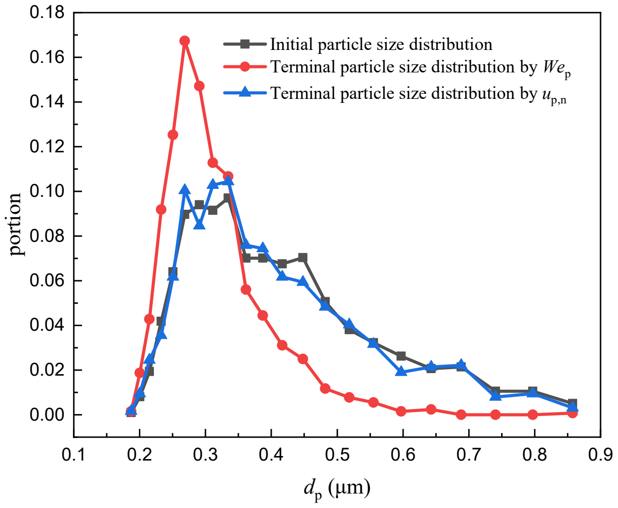

Fig. 5.4. Comparison of aerosol size distribution in the beginning and at the end.

Further quantitative examination is carried out for the We_p criterion. Since the calibration of the threshold is performed based on aerosol decontamination factor, the agreement between simulation results and experimental data is checked at higher submergence in Fig. 5.5 (a). When the simulation time is extended, the calibrated threshold based on liquid height 0.2 m could also predict the *DF* at liquid height 0.4 m accurately, which proves the feasibility of the present method. Aside from that, numerous experimental works [26, 33, 101] observed that the *DF* follows an exponential trend versus liquid height and the tendency is checked as shown in Fig. 5.5 (b). In terms of long-term aerosol removal, the *DF* matches well with the previous experimental finding. The comparison of aerosol size distribution at different liquid height is exhibited in Fig. 5.6. On the whole, a good agreement is presented but a slight deviation still exist when aerosol size is between 0.3 and 0.6 μm, which may originate from the disadvantage in predicting particle rebound velocity based on Eq. (3.28). In general, it can be concluded that the present interfacial model could be used to investigate submicron particle transport inside rising bubbles, which agrees well with experimental data from both qualitative and quantitative aspects.

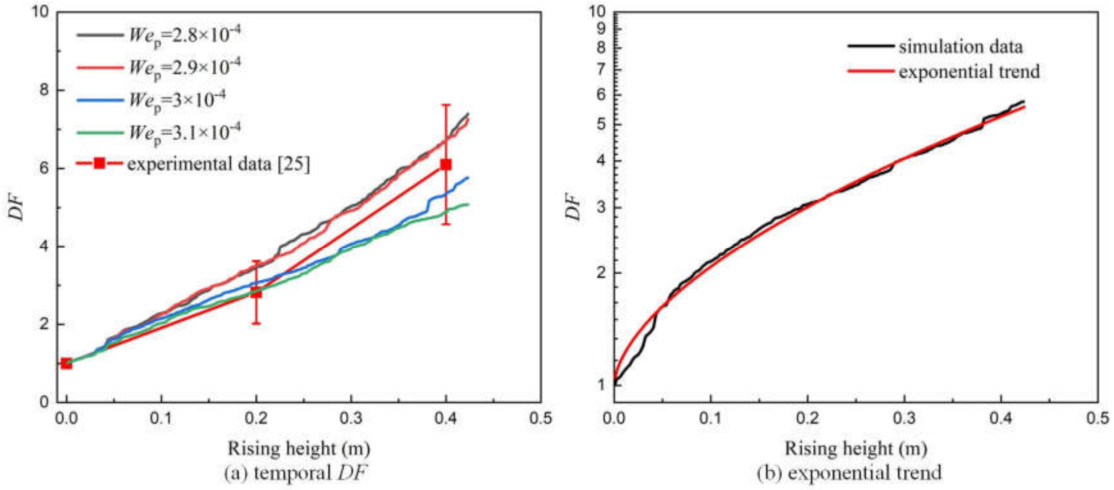

(a) temporal *DF*

(b) exponential trend

Fig. 5.5. Transient decontamination factor and exponential trend versus bubble rising height based on the benchmark data.

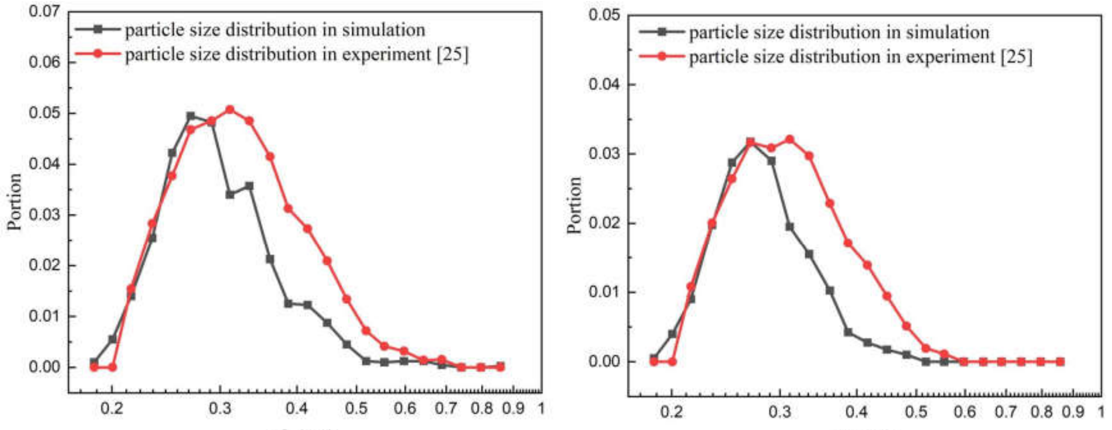

(a) rising height 0.2 m

(b) rising height 0.4 m

Fig. 5.6. Comparison of aerosol size distribution at different bubble rising heights based on the benchmark data.

In terms of the temporal aerosol removal, a notable peak in removal is observed in Fig. 5.3 when the bubble rising height ranges from 0.025 to 0.05 m. To investigate the characteristics of this pronounced removal, the temporal evolution of the bubble with internal aerosol is illustrated in Fig. 5.7. The black dots represent individual particles distributed throughout the entire inner space of the rising bubble. Within the specified time span in Fig. 5.7, the bubble undergoes a slight deformation in shape, while the particles exhibit overall movement throughout the entire inner space.

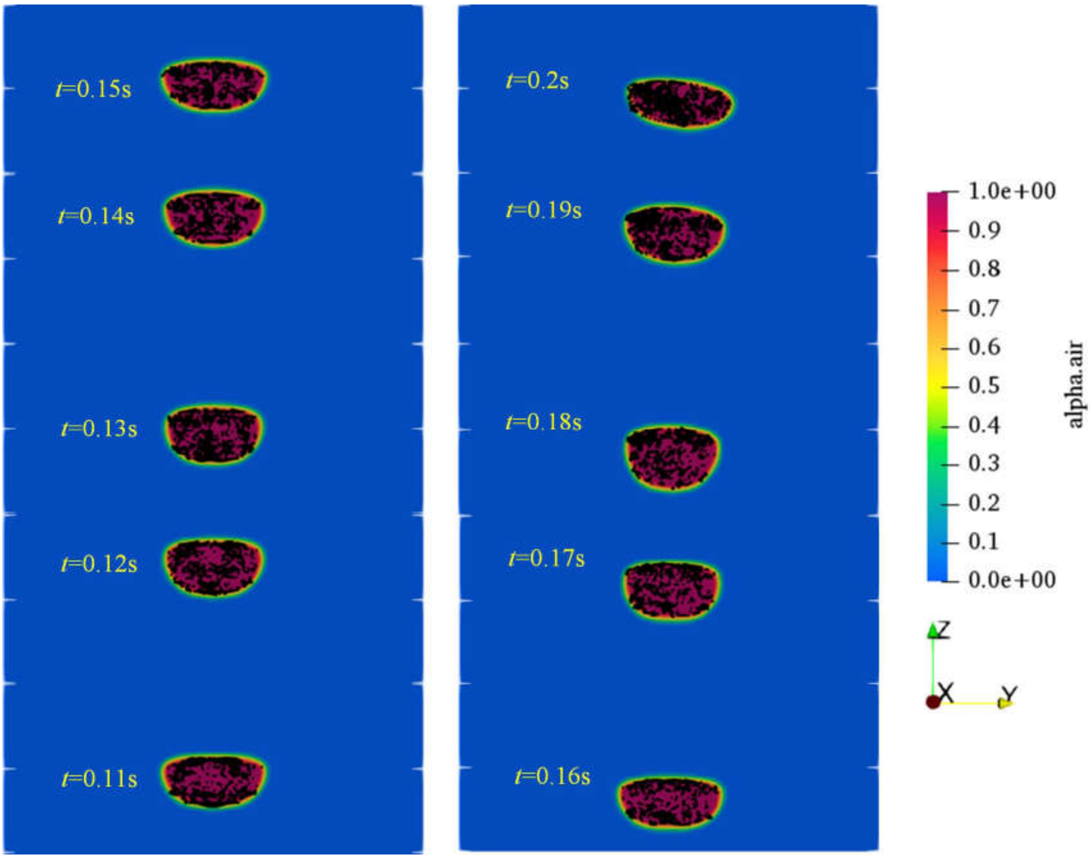

Fig. 5.7. Temporal evolution of aerosol motion inside the rising bubble.

Since lots of particles are included in Fig. 5.7, the relative particle removal position is of interest, which is compared with the transient height of bubble mass centroid. By this way, the removal position of particles at bubble upper surface and bottom surface could be indicated. Fig. 5.8 (a) shows the particle removal position at the moment of t equal to 0.17 s. it can be got that particle removed at the bottom surface is much more significant than that at the upper surface, which could be thought to be the effect of gravity force on the particle. Fig. 5.8 (b) shows the particle removal position corresponding to the time range in Fig. 5.7, where considerable particles are decontaminated through the bubble bottom surface similar to Fig. 5.8 (a). Therefore, it can be inferred that as particles move inside the bubble, the density difference between particle and gas could result in the high possibility of particles contacting the bubble's bottom surface, which could be removed accordingly.

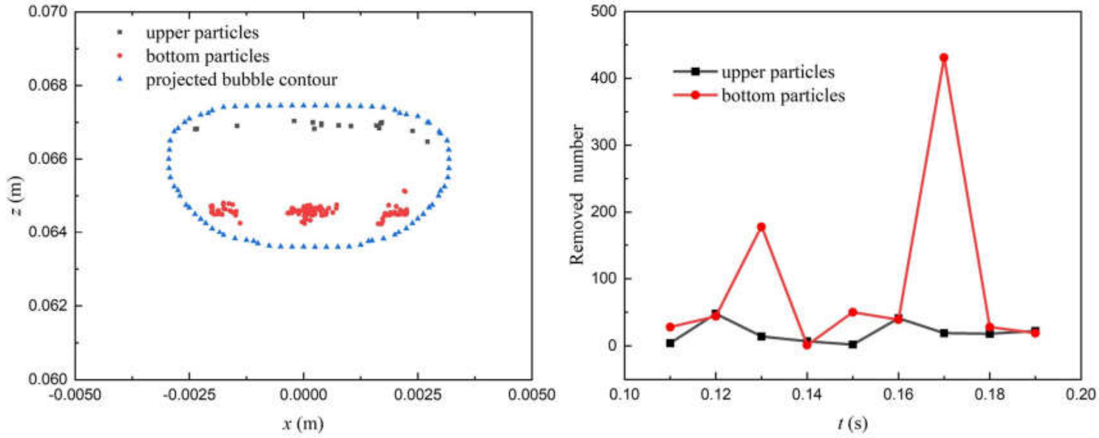

(a) t=0.17 s (b) temporal removal

Fig. 5.8. Spatial position and temporal removal on bubble surface.

5.2 Analysis of aerosol trajectory in the gas phase

When considering the presence of swarm bubbles within the liquid pool, the movement of aerosol particles inside the bubble becomes significant as it influences the residence time of each particle. Since the numerous parameters are involved in the aerosol decontamination process, it is important to provide a preliminary statement regarding the parameter range for the subsequent sections. In this thesis, the size range of the rising bubble is constrained to the previously selected range of the developed correlation, specifically 4 mm $\leq d_b \leq$ 8 mm. Regarding particle density, its value depends on the composition of fission products, as mentioned previously [35]. To define a condition for particle density, we refer to the investigated range of particle density in previous works [37, 52] and set a condition of 1000 kg/m^3 $\leq \rho_p \leq$ 9000 kg/m^3 for this thesis. In terms of particle size, Li et al. [34] reported that the injected aerosol particle size into the liquid pool is generally smaller than 2 μm. Charvet et al. [33] identified that particles within the size range of 0.1 to 1 μm could exhibit low scrubbing efficiency. Based on these findings, the investigated range for particle size in this thesis is defined as 0.05 μm $\leq d_p \leq$ 2 μm. Regarding other properties, we aim to investigate them over a wide range to encompass the potential conditions occurring in the pool scrubbing process.

In this section, bubble size is set to 7 mm and the air-water properties at room temperature equal to 20 °C are applied. Bubble initial height is equal to 0.03 m and other settings are the same as the previous descriptions. Particle size is 1 μm and particle density is equal to 8800 kg/m^3.The initial particle position is presented in Table 5.1 and particles are numbered from 1 to 5. Given that the investigated emphasis is to check aerosol trajectory in the gas phase, the previously developed interfacial penetration model is deactivated in this section merely. When the gas volume fraction at the local particle position is higher than 0.1, the particle is removed from the computational domain.

To indicate aerosol motion, particle displacement is disintegrated into the component along the horizontal and vertical directions respectively. The normalized particle horizontal and vertical displacement can be calculated as follow

$$L_{\mathrm{xy}}^{*} = \sqrt{\frac{x_{\mathrm{p}}^{2} + y_{\mathrm{p}}^{2}}{R_{\mathrm{b}}^{2}}}, \qquad L_{\mathrm{z}}^{*} = \frac{z_{\mathrm{p}}}{R_{\mathrm{b}}} \tag{5.1}$$

Table 5.1 Initial particle position.

Particle	*x* (m)	*y* (m)	*z* (m)
1	0	-0.0005	0.03
2	0	0.0005	0.03
3	0.0005	0	0.03
4	-0.0005	0	0.03
5	0	0	0.03

Fig. 5.9 (a) illustrates the horizontal displacement of particles. For particles 1 to 4, their horizontal displacement initially increases, followed by a slight decrease. Subsequently, their displacement increases once more until removal. This pattern suggests a reciprocating motion along the horizontal direction, which is also the basis of aerosol internal circulation. In contrast, particle 5 exhibits a distinct pattern with a consistently increasing horizontal displacement. This disparity indicates that the motion of aerosol within the rising bubble is largely influenced by its initial position.

In terms of the vertical direction, Fig. 5.9 (b) compares the particle displacement with the centroid of the bubble mass. In the case of all particles, their initial displacement from t^* 0 to 5 is greater than that of the transient bubble mass centroid. This is attributed to the effect exerted by the initial internal gas jet, pushing all particles upwards. Subsequently, all particles tend to remain in the lower portion of the rising bubble due to the significant density difference between the particles and the gas.

As indicated in the work [54], micron particles follow the gas streamline closely inside the rising bubble. To investigate the followability of aerosol motion along the gas streamline, the turning angle is considered, which calculates the deflection of transient velocity from the current timestep *t* to the next time step *t*+Δ*t*. Moreover, the intersection angle is defined as the angle between particle velocity vector and local gas velocity vector.

According to these definitions, the temporal turning angle and intersection angle are presented in Fig. 5.10. Although particle velocity follows the streamline velocity at most timesteps in Fig. 5.10 (a), an obvious deviation appears when the local gas streamline deviates its direction significantly, which consequently results in the angle difference between the particle velocity and local gas velocity. It could also be inferred that as the gas streamline presents a large deviation in direction, the micron particles may not able to follow it closely. Regarding the intersection angle for all particles, notwithstanding bubble shape and flow field are symmetrical in the beginning as discussed in section 4.3, a difference between different particles still exists, which may result from the Brownian force on the aerosol motion in Eq. (3.14).

Fig. 5.11 illustrates the aerosol internal circulation inside the rising bubble. Since these particles are added into the flow field in a three-dimensional manner, only three particles are observed in Fig. 5.11. The images are numbered from 1 to 10 in chronological order. In the beginning, all particles are pushed upward due to the dominant gas jet from 1 to 4. Following the temporal evolution of bubble shape, the bubble internal flow field is also changed accordingly. When particles come to the upper surface, they will follow the gas streamline to move downward at the time sequences from 6 to 10, which forms a kind of internal circulation. Based on Fig. 5.11, it can be concluded that as for aerosol motion in the gas phases, aerosol internal circulation is affected by temporal bubble shape oscillation, which results in the variation in bubble internal field to affect aerosol motion thereby.

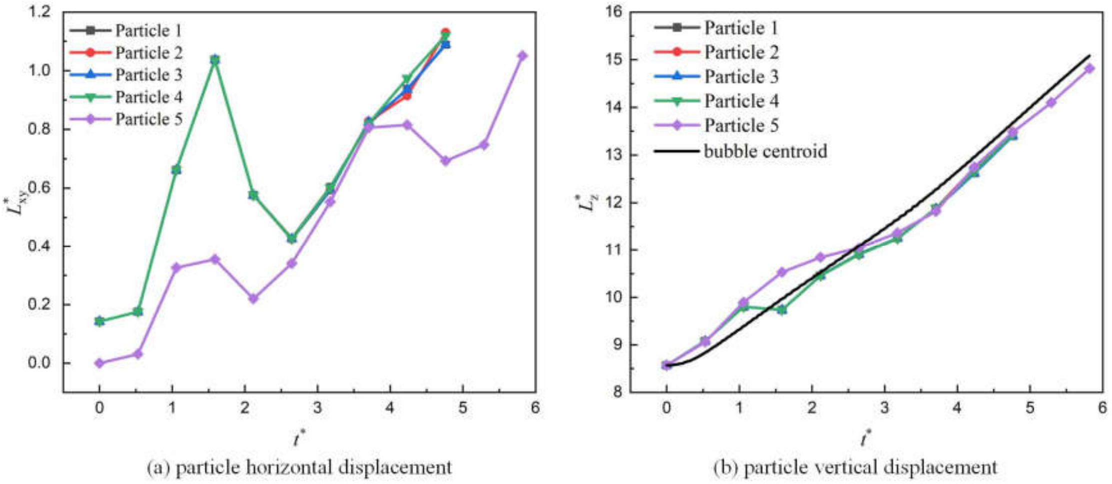

(a) particle horizontal displacement (b) particle vertical displacement

Fig. 5.9. Temporal particle horizontal and vertical displacement.

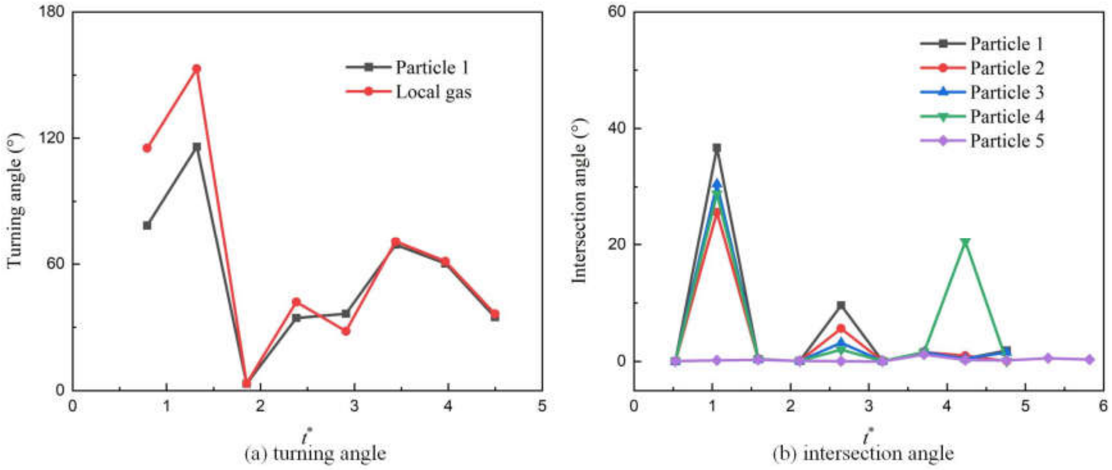

(a) turning angle (b) intersection angle

Fig. 5.10. Temporal particle turning and intersection angle.

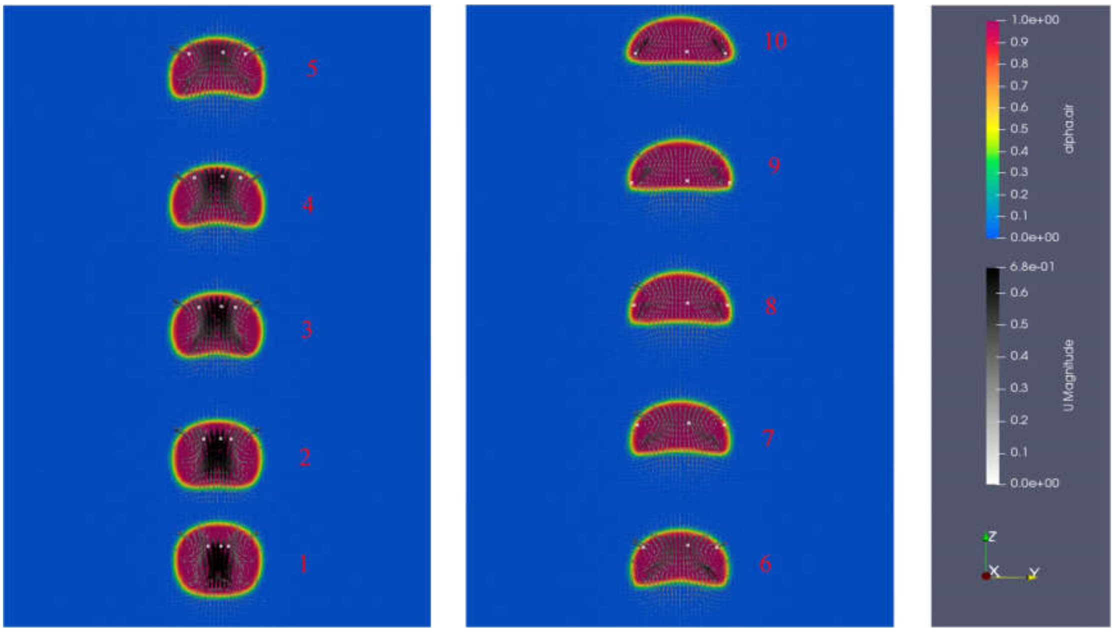

Fig. 5.11. Temporal evolution of aerosol internal circulation.

5.3 Parametric study of principal influential factors based on We_p criterion

In this section, the principal influential factors to affect aerosol interfacial transport process are checked. According to Eq. (3.27), it can be got that particle size, density and gas-liquid surface tension coefficient are the dominant parameters. Therefore, a parametric study will be performed to check the influence of these factors. A general summarization of physical properties is presented in Table 5.2 unless the parametric study is performed for the specific parameter.

Table 5.2 Physical properties of parametric studies for aerosol transport.

Physical properties in simulation			
bubble size (mm)	5	liquid viscosity(kg/m·s)	10^{-3}
gas density (kg/m^3)	1.225	particle size (μm)	0.4
gas viscosity (kg/m·s)	1.79×10^{-5}	particle density (kg/m^3)	4000
surface tension (N/m)	0.0728	particle number	4000
liquid density (kg/m^3)	1000		

5.3.1 Influence of particle size and density

Fig 5.12 exhibits the influence of particle size on aerosol decontamination. When particle size changes from 0.1 to 0.4 μm, an apparent difference is found, which could be attributed to both effects of the increasing number of impact particles and the enhanced capability of particles penetrating the interface. With the increase in particle size, the gradually predominant inertia effect will result in the deviation between particle velocity and local gas velocity close to the interface. As a consequence, the portion of particles impacting the interface is increased by reason of inertial impaction [45]. Aside from that, the particle could penetrate the interface with an increasing probability in light of the definition of particle Weber number. Therefore, the presence of twofold effects leads to a large discrepancy in aerosol decontamination in Fig. 5.12.

In given conditions, the temporal evolution of particle spatial removal position is presented in Fig. 5.13 for two different particle size. With d_p equal to 0.05 μm, several removal peaks are found at specific time points, whereas a notable initial removal is found for d_p equal to 0.8 μm. The results imply that for the removal of small particles, the removal peak is highly dependent on the time-dependent shape oscillation and flow field evolution. By contrast, the decontamination of large particles is relatively insensitive to the flow field because of the dominant effect of particle inertia.

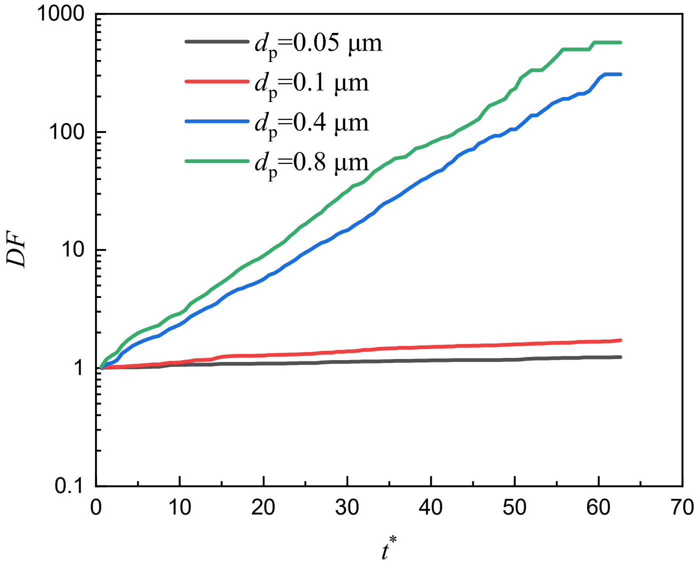

Fig. 5.12. Parametric study of particle size effect on aerosol transport.

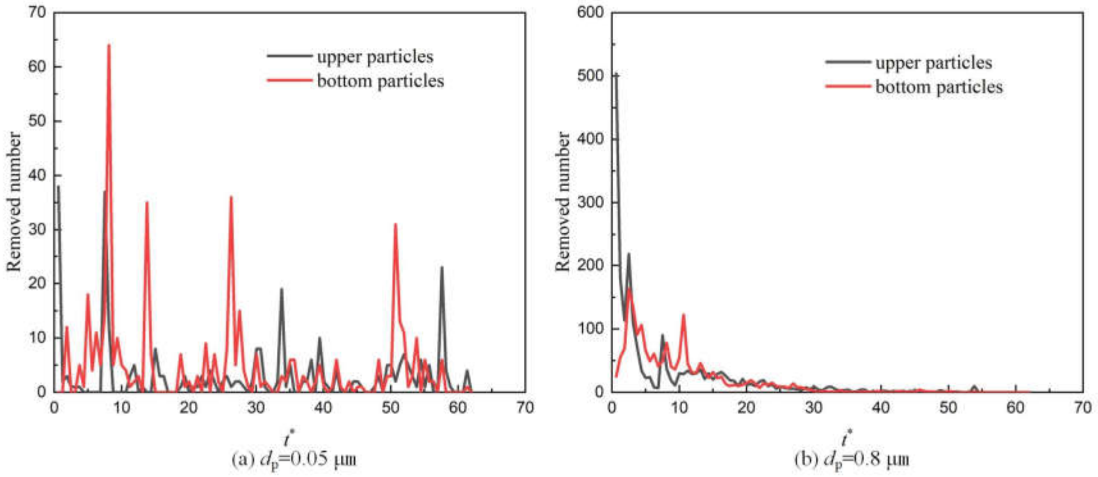

(a) d_p=0.05 μm (b) d_p=0.8 μm

Fig. 5.13. Comparison of particle size effect on aerosol removal position.

Similar to particle size, the influence of particle density on aerosol decontamination could also be ascribed to particle inertia and the detailed dependency is presented in Fig. 5.14. It can be seen that as particle density changes from 1000 to 4000 kg/m^3, a similar gap in the decontamination efficiency is also found similar to the result in Fig. 5.13, which is also an embodiment of particle inertia effects.

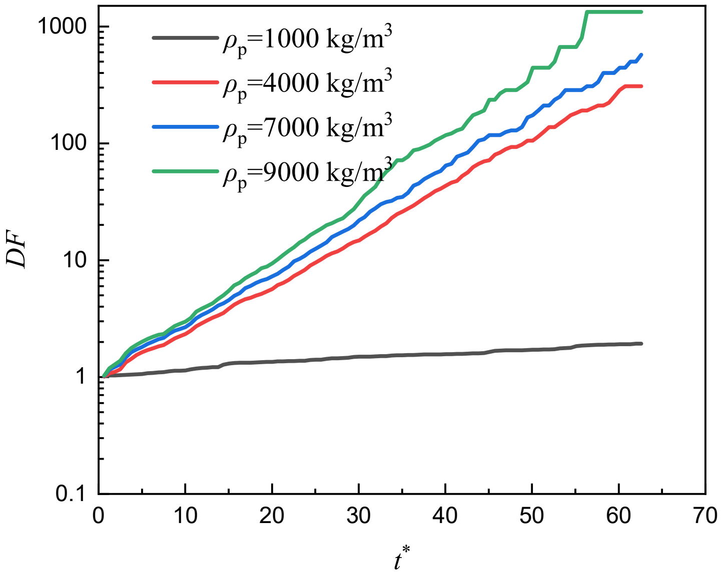

Fig. 5.14. Parametric study of particle density effect on aerosol transport.

5.3.2 Influence of gas-liquid surface tension

Different from particle size and density, the variation in gas-liquid surface tension will change bubble internal flow field. Fig. 5.15 shows the influence of gas-liquid surface tension on bubble rising height. With the decrease in surface tension, bubble rising height is slightly decreased in Fig. 5.15 as a result of decreased rising velocity, which also implies that the bubble internal flow is weakened in this context.

Fig. 5.16 presents the dependency of aerosol decontamination on gas-liquid surface tension. As surface tension decrease from 0.0728 to 0.055 N/m, a monotonous decrease in decontamination factor is presented. Nevertheless, the decontamination factor is increased with surface tension equal to 0.0364 N/m. The overall trend could be explained by a competitive mechanism between weakened internal flow and enhanced penetration capacity. In the context of a weakened internal flow, the circulation of aerosol particles within the bubble is compromised, which in turn affects the probability of particle-interface encounters. Additionally, the presence of decreased surface tension further enhances the capability of particles to penetrate the interface due to the impaired surface tension force. Therefore, since the bilateral effects of surface tension on aerosol decontamination exist, a non-monotonous dependency is exhibited in Fig. 5.16.

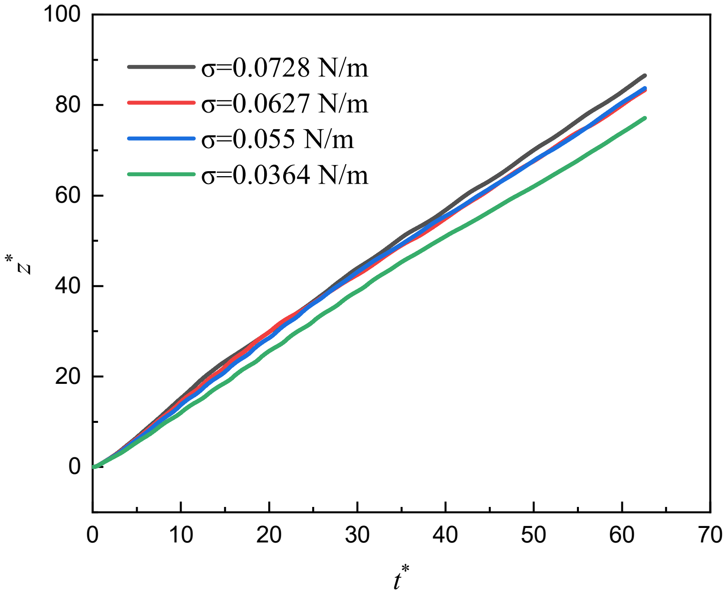

Fig. 5.15. Bubble rising height with different gas-liquid surface tension coefficients.

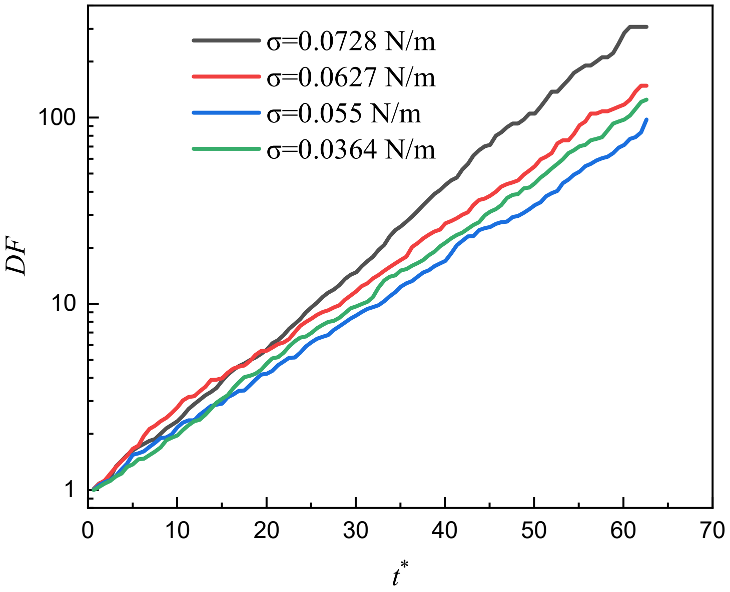

Fig. 5.16. Parametric study of gas-liquid surface tension effect on aerosol transport.

5.4 Influence of *Eo* and *Ga* numbers on aerosol transport behavior

According to Fig. 5.16, it can be got that the change in bubble dynamics may bring about a complex change in aerosol decontamination. To check the effect in detail, the influence of bubble dynamics on aerosol transport behavior in this section is summarized mainly by Eötvös and Galilei numbers because these two dimensionless numbers dominate single bubble dynamics according to the discussion in section 4.

Aside from that, the aerosol transport process in this section is investigated from a discrete viewpoint by reason of the presence of particle interfacial behavior. Specifically, the process of particle transport from gaseous bubbles to liquid water is divided into three subprocesses in order, which is the approach of particles on the bubble surface (the approaching process), the impact of particles on the bubble surface (the impacting process), and the moving of particles inside liquid water (the decontamination process). The approaching process and the impacting process are particularly checked further due to their significance. The numerical settings are identical to the previous sections and the summarization of physical properties is presented in Table 5.3. As the parametric study is performed on surface tension, the defaulted liquid viscosity is set to 10^{-3} kg/m·s. In the other case, the defaulted surface tension is fixed at 0.0728 N/m.

Table 5.3 Physical properties of changeful bubble dynamics in simulation.

physical properties			
bubble size (mm)	6	liquid viscosity(kg/m·s)	calculated by *Ga*
gas density (kg/m^3)	1.225	particle size (μm)	0.3
gas viscosity (kg/m·s)	1.79×10^{-5}	particle density (kg/m^3)	1500
surface tension (N/m)	calculated by *Eo*	particle number	8000
liquid density (kg/m^3)	1000		

5.4.1 Influence of *Eo* numbers

In this part, the size of Galilei number is fxed at 514. Fig. 5.17 displays the variation in terminal decontamination factor with Eötvös numbers. In alignment with the results in Fig. 5.16, a clear non-monotonic dependency is presented with the increasing Eötvös numbers. In particular, the aerosol decontamination is largely ameliorated with *Eo* equal to 3.5 compared to that with *Eo* equal to 0.5, which implies that the reduction in surface tension could benefit aerosol decontamination considerably because of the impaired surface tension force on the aerosol. However, the direct addition of surfactant to the liquid pool may obtain the converse effect according to the particle collection experiment by Koch et al. [38]. In effect, the contradiction could be explained by the change in aerosol internal circulation. The presence of surfactants gives rise to the retardation of the gas-liquid interface, which also result in the complete cessation of bubble internal flow to affect the particle-interface counter significantly [38]. Therefore, it can be got that both the approaching process and the impacting process are crucial for aerosol decontamination process.

In terms of the approaching process, aerosol deposition velocity is especially considered. According to the direction of interfacial normal in Fig. 3.2, as the vertical component of particle velocity is opposite to the direction of interfacial normal, the vertical component is defined as the deposition velocity, which could be written as

$$u^*_{\mathrm{deposition}} = \frac{u_{\mathrm{p,n}}}{\sqrt{gR_{\mathrm{b}}}} \tag{5.2}$$

After the summarization of all timesteps, the total particle count could be got as shown in Fig. 5.18. As *Eo* numbers change from 0.8 to 3.5, the change in particle counts seems to be limited for the given particle. However, a notable change in particle velocity distribution appears and the size of $u^*_{\mathrm{deposition}}$ where the profile peak locates also varies from 1.17 to 2.04. On the whole, with increasing *Eo* numbers, the resultant influence on particle-interface encounter probability is slight but particle deposition velocity is deteriorated significantly. It should be indicated here that the deposition velocity of micron aerosol particle is largely subject to the local gas velocity because of the ultra-small size of aerosol particle. Therefore, the shift in profile peak in Fig. 5.18 also means that the increase in *Eo* numbers could result in a weakened internal flow, which decreases particle velocity thereby.

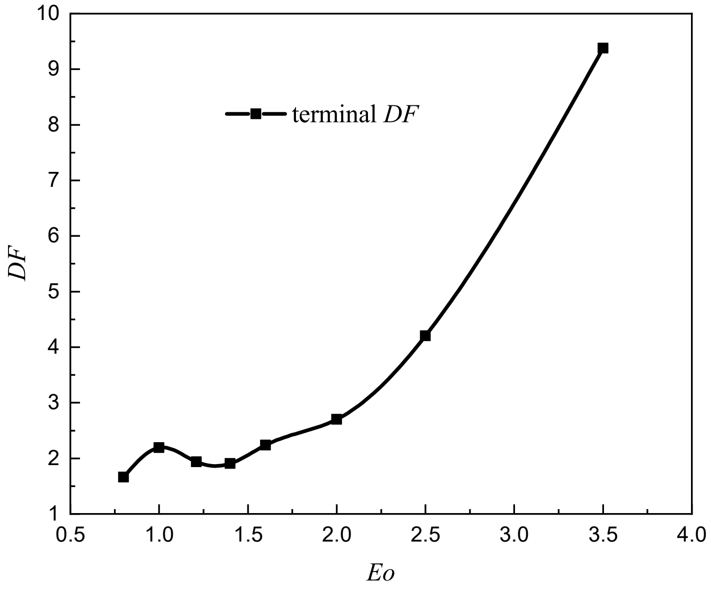

Fig. 5.17. Variation in terminal decontamination factor with Eötvös numbers.

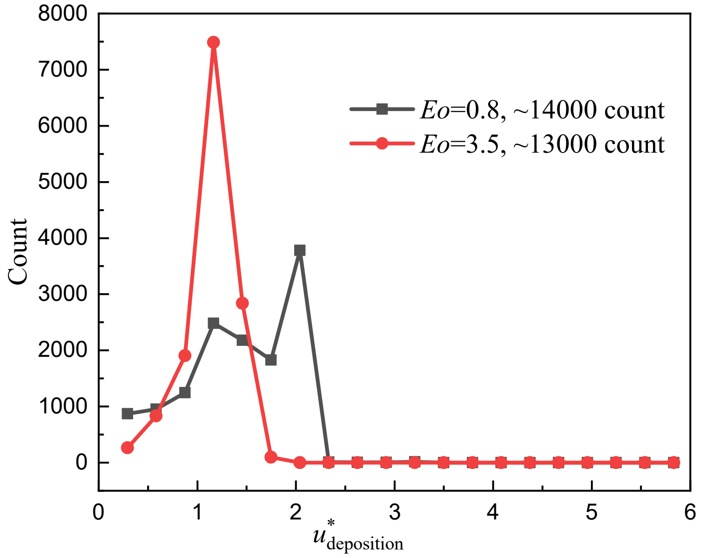

Fig. 5.18. Influence of Eötvös numbers on aerosol velocity distribution.

As for the impacting process, aerosol removal distribution is considered. Specifically, the angle of particle removed position compared to bubble mass centroid is calculated. At each timestep, the transient bubble mass centroid is treated as the origin, whereby an *x*-*z* plane in Fig. 3.4 could be built based on the origin. From a recorded timestep t to the next recorded timestep $t+\Delta t$, a part of particles may get removed from the computational domain. The particle positions at timestep t are defined at the removed position and the removal angle is calculated accordingly. Obviously, the size of Δt may affect the calculation of aerosol removal angle. The decrease in Δt could give rise to a high accuracy but the load in data storage will also increase dramatically. Δt is selected at 0.01 s in this work and a sensitivity study is performed to quantify its effect on the removal angle as shown in Fig. 5.19. It can be observed that a good convergence is achieved among three curves and Δt equal to 0.01 is found to be appropriate to be used to assess aerosol removal distribution, which will be further used as a default in this work.

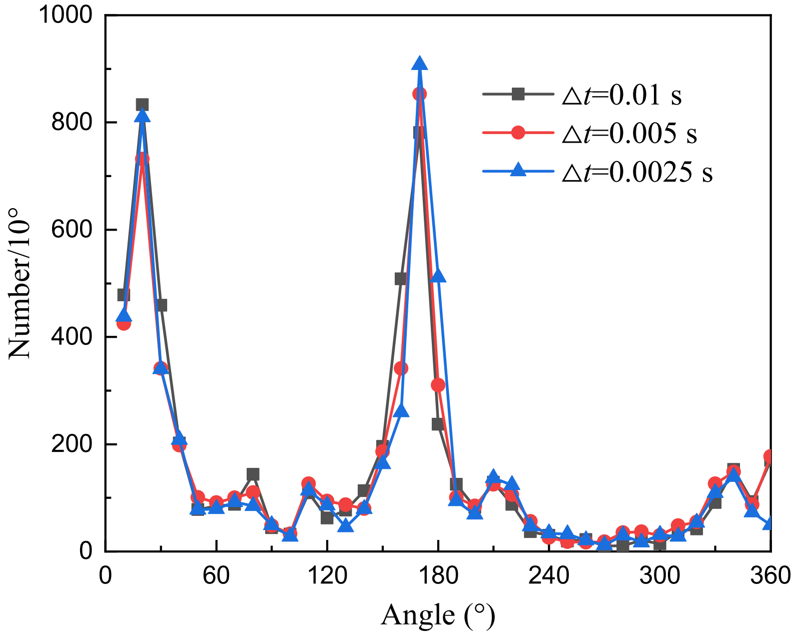

Fig. 5.19. Sensitivity study of the influence of timestep on aerosol removal distribution.

Fig. 5.20 presents a comparison of the aerosol removal distribution with different *Eo* numbers. When *Eo* is equal to 0.8, particles are generally removed across the entire bubble surface. In contrast, with *Eo* equal to 3.5, particles tend to be removed within two specific ranges: from 0° to 30° and from 150° to 180°. Since the removal of particles occurs in a three-dimensional manner, it can be inferred that a significant number of particles are likely to be removed due to their impact on the bubble lateral surface when *Eo* is equal to 3.5. This difference in Fig. 5.20 can be attributed to the influence of surface tension force on particle rebound in the simulation.

As the bubble ascends in the water, the bubble will go through successive shape oscillation as analyzed in section 4. Owing to the influence of bubble deformation, the internal flow field will present a time-dependent evolution, which results in aerosol internal circulation as shown in Fig. 5.11. The crucial discordance appears when the particle moves downwards as shown in Fig. 5.21. With *Eo* equal to 3.5, the particle follows the gas streamline to move close to the bubble surface in stage I. Subsequently, the particle deviates from the gas streamline to hit the bubble surface by reason of particle inertia in stage II. In the context of small surface tension, the particle is easy to pass the interface and gets removed thereby in stage III. Given most particles are removed from stage I to III, it can be got that centrifugal deposition [7] is the dominant removal mechanism, while the effect of gravity sediment is limited.

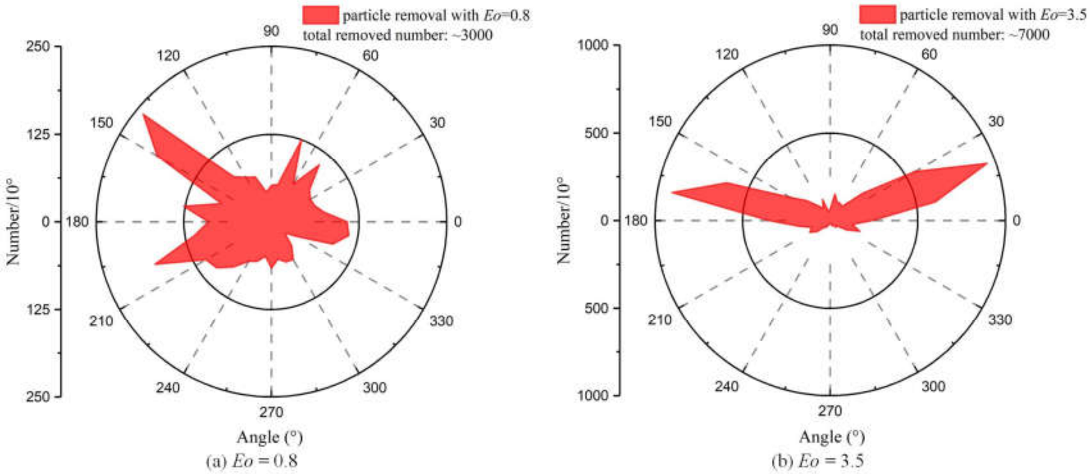

(a) $Eo = 0.8$ (b) $Eo = 3.5$

Fig. 5.20. Influence of Eötvös numbers on aerosol removal distribution.

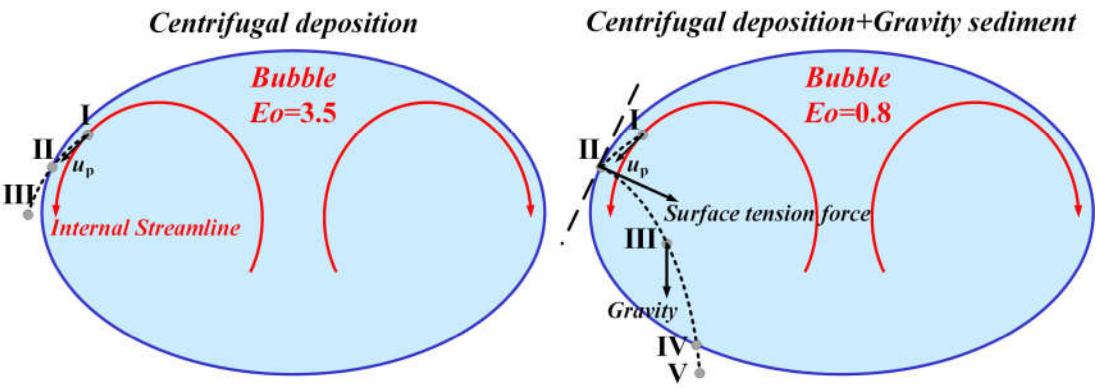

Fig. 5.21. Mechanism of how ultrafine aerosol deposits on the bubble surface affected by gas-liquid surface tension.

In the context of *Eo* equal to 0.8, when the particle deviates the internal streamline to hit the bubble surface from stage I to stage II, the considerable surface tension force will resist the particle from penetrating the interface. As a consequence, the particle will reverse its motion and return to the gas phase in stage III. Due to the cumulative influence of particle gravity, the particle is prone to impact the bubble bottom surface with a high impact velocity in stage IV and get decontaminated in stage V. As a result of twofold influences from surface tension force and gravity force, numerous particles are removed at the spatial position close to the gravity direction, which also suggests that both centrifugal deposition and gravity sediment exert significant influences on aerosol transport as *Eo* numbers are sufficiently small.

The progressive transition of aerosol removal distribution with different *Eo* numbers is presented in Fig. 5.22. In conformity with Fig. 5.21, the increase in *Eo* numbers brings about the increasing portion of particles removed at the bubble lateral surface, which signifies the gradually predominant centrifugal deposition. In light of the above analysis, it can be concluded that the increasing *Eo* numbers give rise to the weakened internal flow in the approaching process and the impaired surface tension force in the impacting process. In particular, aerosol removal mechanism is also changed with *Eo* numbers. Under the circumstance of small *Eo* numbers, both centrifugal deposition and gravity sediment exert significant effects on aerosol decontamination, whereas centrifugal deposition is dominant with large *Eo* numbers.

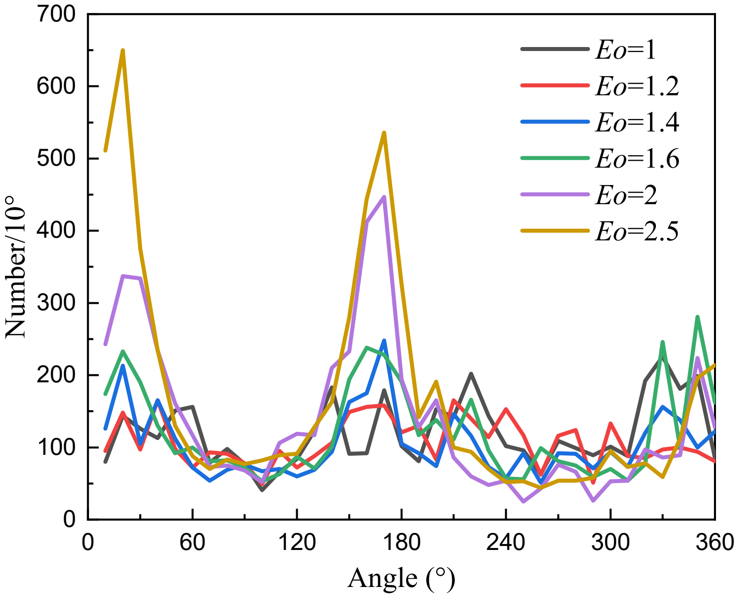

Fig. 5.22. Dependency of aerosol removal distribution on changing Eötvös numbers.

5.4.2 Influence of *Ga* numbers

As for all cases, the size of *Eo* is equal to 1.2 in this section. Fig. 5.23 shows the influence of *Ga* numbers on aerosol decontamination. With the increasing *Ga* numbers, the decontamination factor rises monotonically, which implies that the increasing liquid viscosity is detrimental to aerosol decontamination. It should be mentioned that in the single particle impacting the gas-liquid interface experiment [13], the increase in liquid viscosity impedes the particle from penetrating the interface, which could be attributed to the increased resistance force from the surrounding fluid with the increasing viscosity. Despite the trend in Fig. 5.23 agrees with the experimental finding [13], the approaching process should be specially checked because the variation in liquid viscosity affects bubble shape oscillation to influence the approaching process.

In the approaching process, aerosol deposition velocity distribution is presented in Fig. 5.24. It can be observed that albeit the deposition velocity where the profile peak locates is not changed, a noteworthy difference exists as to particle counts. The decreasing *Ga* numbers give rise to a pronounced drop in particle counts, which is due to the reduction in the amplitude of bubble shape oscillation. According to the previous analysis in Section 4, bubble shape oscillation is largely affected by *Ga* numbers. The oscillatory amplitude with *Ga* equal to 2057 is much higher than that with *Ga* equal to 42 because an increasing portion of bubble potential energy is dissipated into the liquid with high viscosity. In the presence of a less oscillatory interface, the probability of particle-interface encounter is affected critically as revealed in Fig. 5.24.

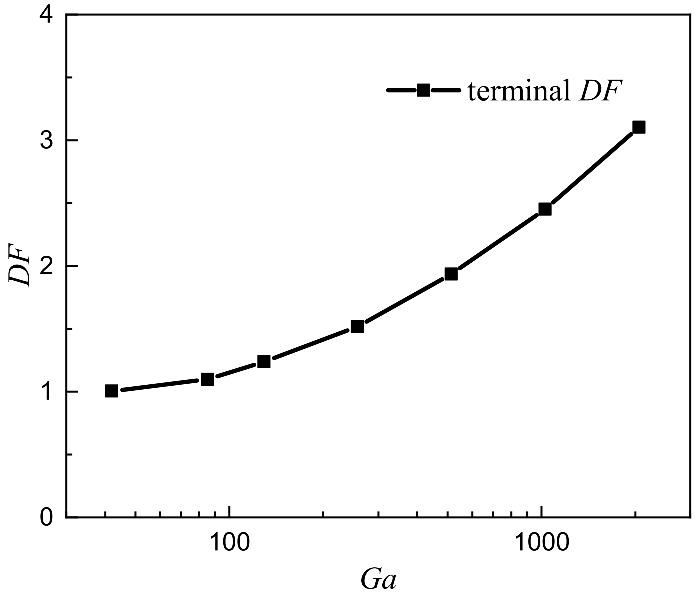

Fig. 5.23. Variation in terminal decontamination factor with Galilei numbers.

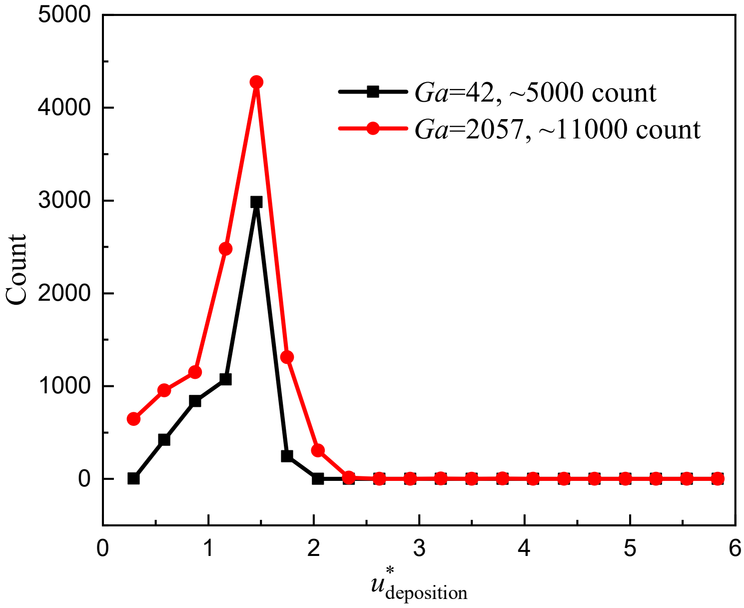

Fig. 5.24. Influence of Galilei numbers on aerosol velocity distribution.

Fig. 5.25 shows a comparison of aerosol removal distribution with different *Ga* numbers. For both cases in Fig. 5.25, particles are removed over the whole bubble surface. However, under the circumstance of *Ga* equal to 42, only a few particles are removed, which implies that the trapping effect of bubble interface on moving particles is significant. The trapping effect here means the influence of hydrodynamics force on the particle to prevent the particle from penetrating the interface. Or rather, the viscous drag on moving particles is magnified in the interfacial region with increasing *Ga* numbers. As illustrated in section 3, the resolved fluid properties from VOF method are passed into the LPT frame to evolve aerosol motion. In the interfacial region, the fluid properties are got from the weighted average based on gas volume fraction. As a consequence, as the particle displacement toward the outside of the bubble is increased, the corresponding viscous drag is also increased remarkably, which obstructs particles passing through the interface as shown in Fig. 5.25 (a).

To examine whether there exists a dependency of aerosol removal mechanism on liquid viscosity, aerosol removal at the bubble upper and bottom surface is considered as shown in Fig. 5.26. It can be got that aerosol spatial removal position is insensitive to *Ga* numbers, which suggests that aerosol removal mechanism is independent of liquid viscosity. Therefore, it could be summarized that the decreasing *Ga* numbers bring about the dampened bubble shape oscillation in the approaching process and the escalated viscous drag in the impacting process. Under the circumstance of the dampened shape oscillation, the probability of particle-interface encounter is deteriorated critically. The escalated viscous drag prevents the particle from penetrating the interface and the general trend in simulation agrees with the previous experimental finding [13]. Different from surface tension, liquid viscosity is found to be independent of aerosol removal mechanism generally.

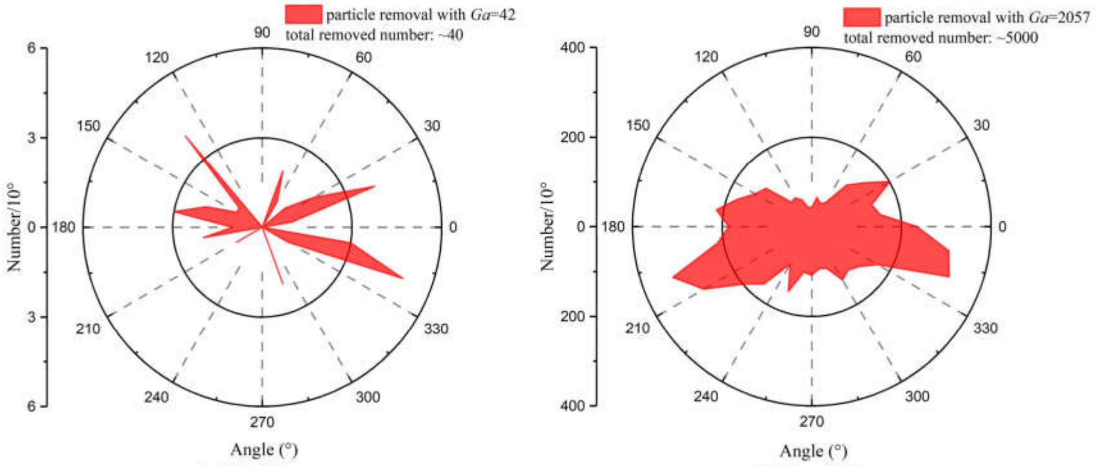

(a) *Ga*=52 (b) *Ga* = 2057

Fig. 5.25. Influence of Galilei numbers on aerosol removal distribution.

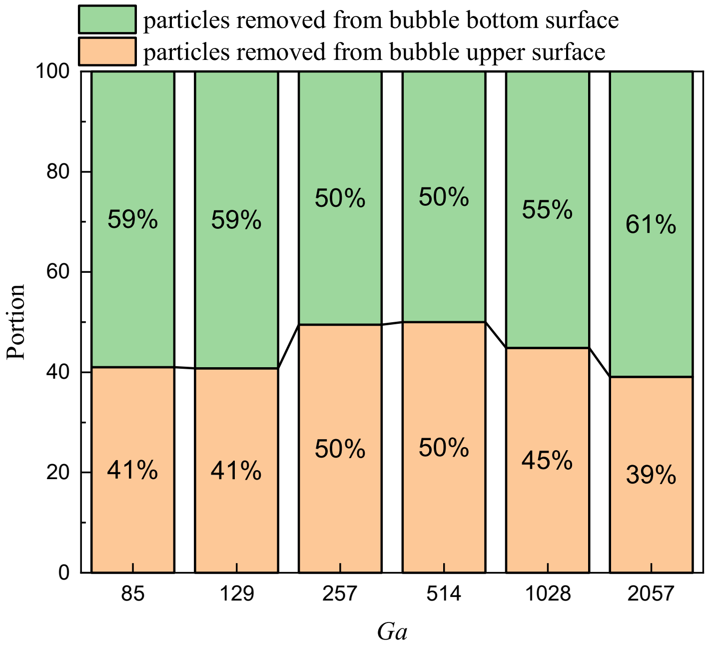

Fig. 5.26. Dependency of aerosol removal distribution on changing Galilei numbers.

5.5 Aerosol residence time

According to the previous analysis, it can be got that particle size and surface tension could affect the profile of aerosol residence time significantly, which will be checked in this section. After that, aerosol residence time under the circumstance of terminal flow field will also be examined.

5.5.1 Investigation of aerosol residence-time distribution

The numerical settings in this section are in alignment with that in the previous section. Different-sized particles are chosen as variables, while their residence time is explored with varying surface tension coefficients. A summary of physical properties is presented in Table 5.4.

Table 5.4 Physical properties applied in simulation.

physical properties			
bubble size (mm)	6	liquid viscosity(kg/m·s)	10^{-3}
gas density (kg/m^3)	1.225	particle size (μm)	0.1 ~ 2
gas viscosity (kg/m·s)	1.79×10^{-5}	particle density (kg/m^3)	1500
surface tension (N/m)	0.07 or 0.03	particle number	8000
liquid density (kg/m^3)	1000		

According to previous definitions, the temporal evolution of E-curves with high surface tension is presented in Fig. 5.27. The profile shapes change with the variation in aerosol size. In terms of d_p equal to 0.1 and 0.2 μm, the temporal removal is generally insensitive to bubble internal flow, which is also accompanied by the continuous oscillations in E-curves. Regarding d_p equal to 0.3 μm, a considerable removed portion is found for t^* from 15 to 35, which is because of the remarkable bubble shape oscillation as indicated before. The further increase in aerosol size brings about the shift of profile peaks to the beginning. Meanwhile, the oscillation in E-curves also disappears with the increasing aerosol size gradually, which means that if the aerosol size is large enough, the temporal aerosol removal behavior is independent of bubble internal flow because of dominant inertia effects.

Fig. 5.28 shows residence-time distribution function with low surface tension. As surface tension is changed, the resultant difference in temporal removal behaviors seems remarkable. Regarding d_p equal to 0.1 μm, aerosol decontamination is centralized for t^* from 10 to 25 related to bubble shape oscillation. Subsequently, particle removal is rather limited in the gentle flow field even though the bubble could present a more deformed terminal shape. In comparison to the results in Fig. 5.27, it can be got that as aerosol size is decreased to 0.1 μm, aerosol decontamination is dominant by the strength of internal flow because of the high followability of small aerosol along gas streamline. As for d_p from 0.2 to 2 μm, the evolution pattern of E-curves is similar to the previous pattern in Fig. 5.27.

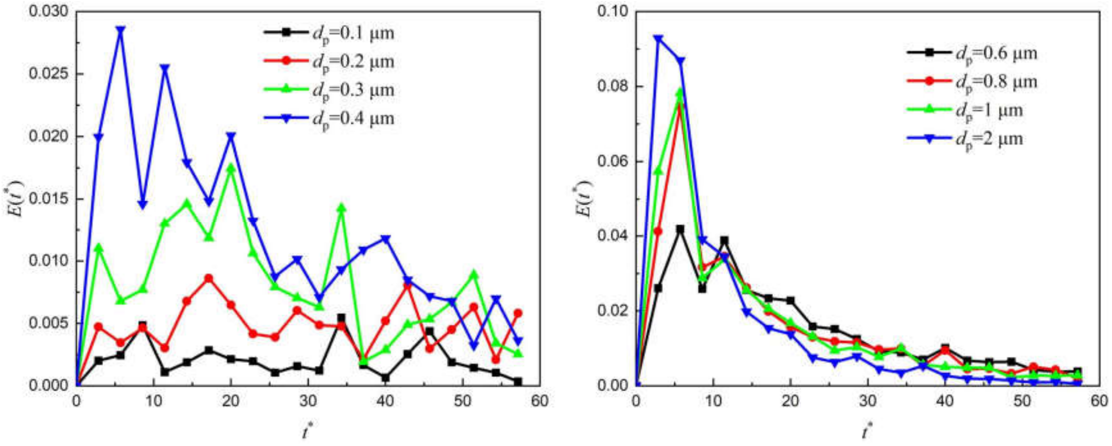

Fig. 5.27. Temporal evolution of aerosol residence-time distribution function with high surface tension.

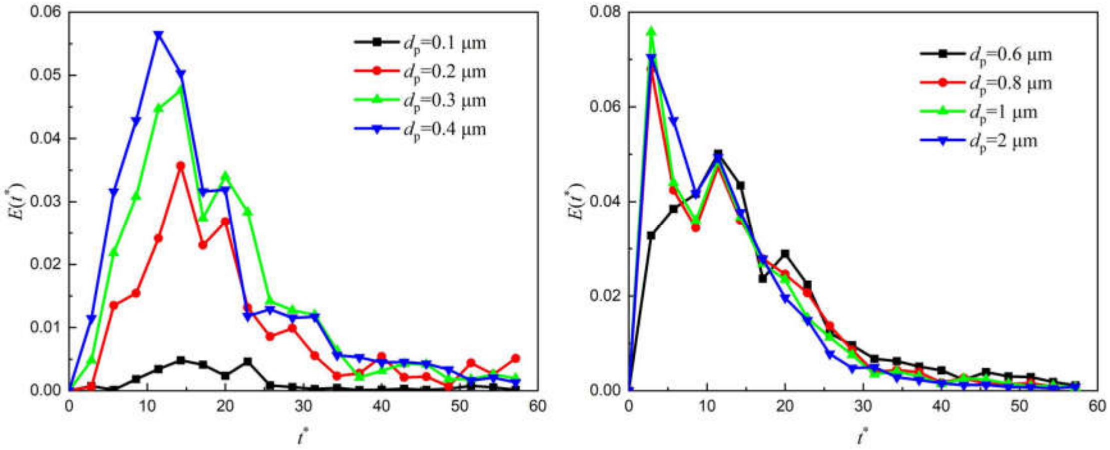

Fig. 5.28. Temporal evolution of aerosol residence-time distribution function with low surface tension.

In terms of most *E*-curves in Fig. 5.27 and 5.28, the sharp increase in the beginning could be attributed to the dispersion of aerosol particles inside the bubble. After the full development of aerosol internal circulation of aerosol particles inside the bubble, most *E*-curves generally follow a continuous decreasing trend. Therefore, the consideration of *E*-curve characteristics is carried out after the temporal profile reaches its peak. In effect, the influential factors in aerosol decontamination process could be classified into two aspects. The chief aspect is related to constant physical properties including aerosol number, aerosol size, and gas-liquid properties and so on. The effect of constant physical properties could result in an exponential trend of *DF*, which has been widely observed in experimental observations [26, 33, 101]. In ideal cases, if aerosol decontamination process is merely subject to aerosol number, it should suffice the form of decay function rigidly. Apart from that, the subordinate aspect is linked to transient flow properties, such as bubble shape oscillation, the strength of internal flow and liquid flow turbulence and so on. Thanks to transient flow properties, albeit the bubble comes to the terminal stage, it could still decontaminate ultrafine particles continuously, which is manifested as long tails of *E*-curves in Fig. 5.27 and 5.28. For simplification, it could be assumed that after the profile comes to its peak, its distribution follows an exponential distribution as

$$E(t) = k_1 e^{-k_2 t} \tag{5.3}$$

In this case, the extrapolation of E-curve could be performed based on Eq. (5.3). Aerosol mean residence time and variance could be calculated as shown in Fig. 5.29. For both cases, aerosol mean residence time decreases with the increase in aerosol size. In particular, the variance with high surface tension is higher than that with low surface tension, which also means that aerosol with high surface tension could spread more widely along the timeline compared to that with low surface tension.

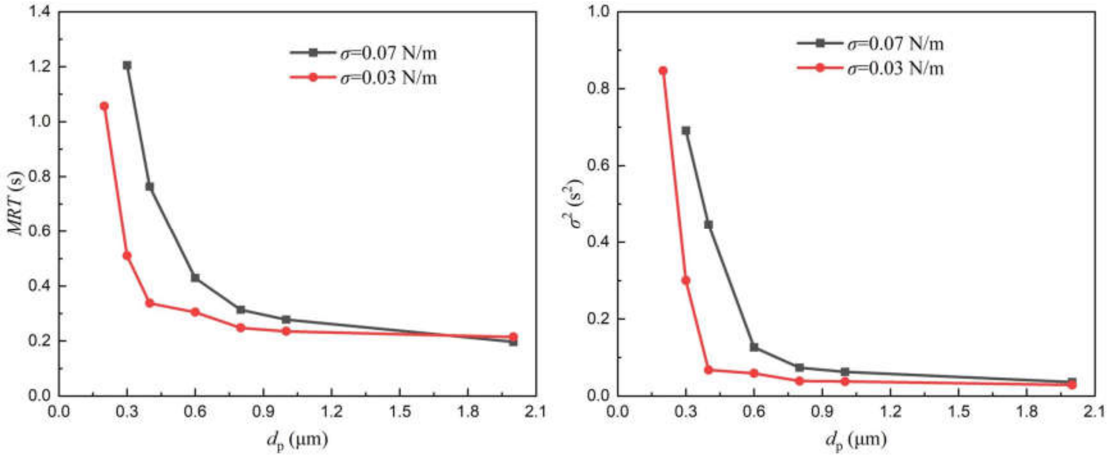

Fig. 5.29. Aerosol mean residence time and variance with various sized particles.

5.5.2 Investigation of aerosol mean residence time

The investigation of aerosol mean residence time within bubble swarm region will be carried out in this section. It is thought that as bubbles rise within the swarm region, most bubbles come to a quasi-stable region, where bubbles could generally keep a constant rising velocity with a terminal internal flow field. Similarly, as the bubble reaches the terminal status in simulation, particles are injected into the bubble in this section, where particles will move under the circumstance of terminal internal flow field. To be specific, the cases of bubbles without particles are simulated from 0 to 1 s to make sure the bubble comes to the terminal status and then particles are injected at the physical time of 1 s. Three variables including bubble size, particle size and surface tension coefficients are changed as presented in Table 5.5, whereas other physical properties are consistent with the previous section. Overall, a numerical data matrix including 29 cases is performed for the modeling of aerosol mean residence time, where the dependency of residence time on bubble size, surface tension and particle size will be explored further.

In the context of terminal flow field, the dependency of aerosol decontamination on bubble size, particle size and surface tension is presented in Fig. 5.30. It can be seen that the influence of bubble size and particle size on aerosol decontamination is monotonic, while the effect of surface tension is non-monotonic. Although particles move within the terminal flow field, the dependency is consistent with the case of particles injected at the beginning of an initially spherical bubble. A typical case of E-curve is shown in Fig. 5.31, where the physical time starts from the onset of particle injection for simplification. In the context of terminal flow field, particles are spreading over the whole bubble in the beginning and then follow a nearly exponential decay, which is also accompanied by a long tail. The general characteristics are the same as the previous analysis in Fig. 5.27 and 5.28.

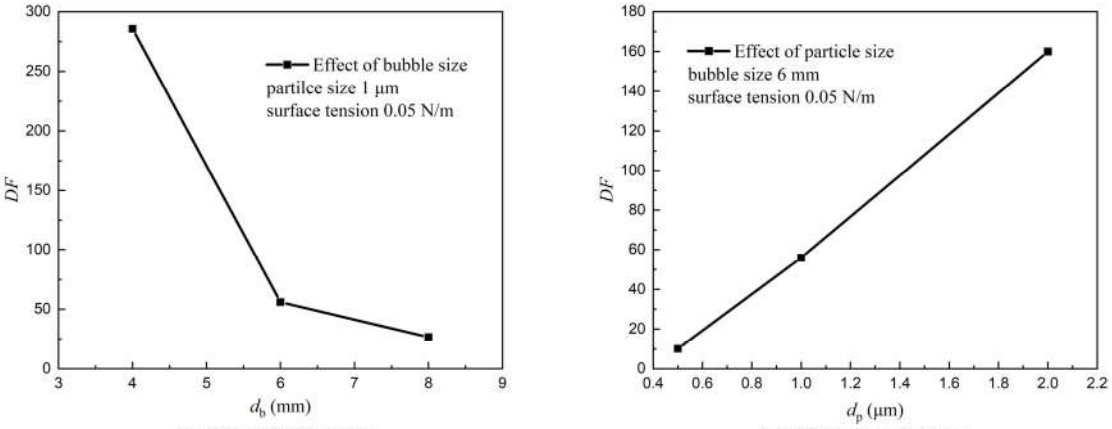

(a) Effect of bubble size (b) Effect of particle size

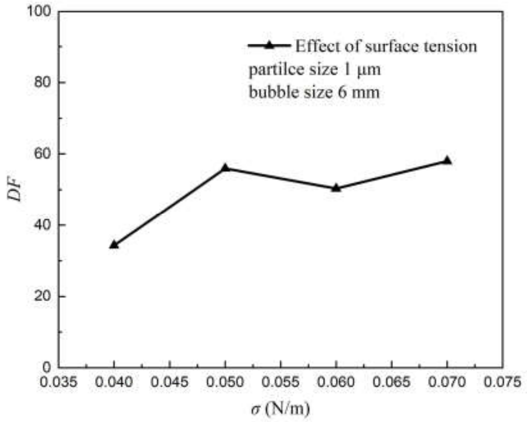

(c) Effect of surface tension

Fig. 5.30. Dependency of aerosol decontamination on bubble size, particle size and surface tension in the context of terminal flow field.

Table 5.5 Investigated cases for aerosol mean residence time.

d_b (mm)	σ (N/m)	d_p (μm)	d_b (mm)	σ (N/m)	d_p (μm)
4	0.03	0.5	6	0.06	0.5
4	0.03	1	6	0.06	1
4	0.03	2	6	0.06	2
4	0.05	0.5	6	0.07	0.4
4	0.05	1	6	0.07	0.5
4	0.05	2	6	0.07	0.6
6	0.04	0.4	6	0.07	1
6	0.04	0.5	6	0.07	2
6	0.04	1	8	0.05	0.5
6	0.04	2	8	0.05	1
6	0.05	0.4	8	0.05	2
6	0.05	0.5	8	0.1	0.5
6	0.05	1	8	0.1	1
6	0.05	2	8	0.1	2
6	0.06	0.4			

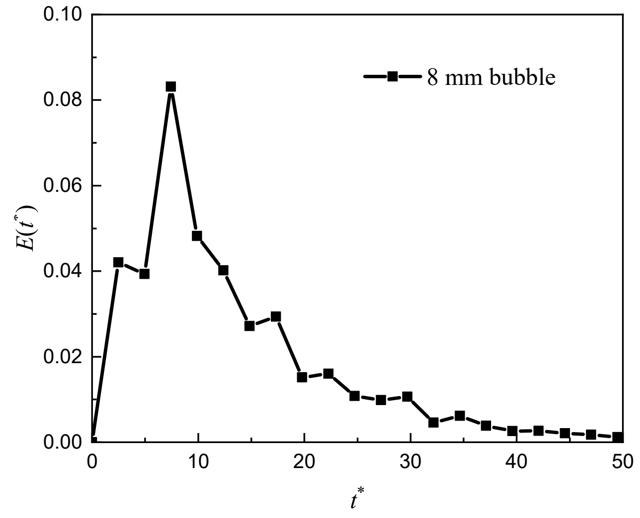

Fig. 5.31. Evolution of *E*-curve in the context of terminal flow field.

Fig. 5.32 shows the effect of bubble size, particle size and surface tension on aerosol mean residence time. In alignment with Fig. 5.30, aerosol mean residence time shows the same dependency as that of *DF* on influential factors. Obviously, the presence of a non-monotonic relationship brings about considerable difficulty in the analysis of aerosol mean residence time, which should be dealt with carefully.

To summarize the main influential factors to affect aerosol mean residence time, we revisited aerosol decontamination process. As discussed before, aerosol decontamination could be divided into the approaching process and the impacting process, separately. Although both processes are significant for aerosol decontamination, there exists a so-called progressive relationship from the approaching process to the impacting process. In other words, although the influential factors acting in the approaching process could affect the probability of particle-interface encounter and particle normal impact velocity, the direct process related to aerosol decontamination should be the impacting process for each particle. In this case, aerosol mean residence time should be tightly connected to the decontamination performance of single particle individually. As mentioned before, whether a particle could be decontaminated is largely subject to We_p criterion. Therefore, we refer to the definition of We_p and assumed a parameter, namely $\rho_p d_p/\sigma$ as the key parameter to check its relationship with aerosol mean residence time, where this parameter stands for the relative strength between particle inertia and the surface tension force on the particle. The dependency of aerosol mean residence time on this parameter is presented in Fig. 5.33. The results reveal that as $\rho_p d_p/\sigma$ is higher than 0.02, particles are decontaminated promptly and aerosol mean residence time could be estimated by a constant value approximately irrespective of bubble size. In this context, particle inertia could be dominant enough to overcome the influence of surface tension force, which results in a small aerosol mean residence time in general. Correspondingly, the effect of bubble size on aerosol decontamination is rather limited. By contrast, when $\rho_p d_p/\sigma$ is below 0.02, the difference in bubble size could lead to a deviation in aerosol mean residence time, but most scatter points could still be approached by a smooth curve in general as shown in Fig. 5.33. The results also indicate that even though the reduction in bubble size could enhance aerosol decontamination to a certain degree under the circumstance of small particle inertia, the effect of surface tension force could be predominant to prolong aerosol mean residence time significantly.

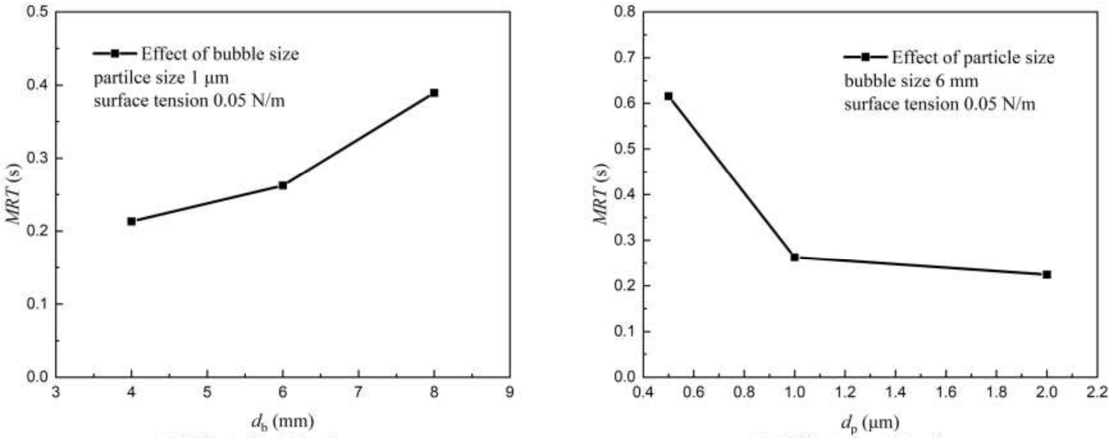

(a) Effect of bubble size

(b) Effect of particle size

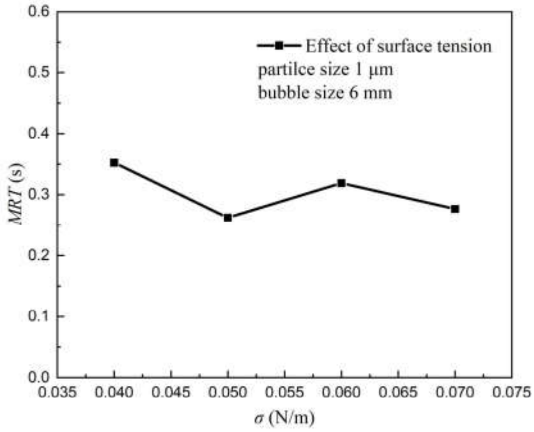

(c) Effect of surface tension

Fig. 5.32. Dependency of aerosol mean residence time on bubble size, particle size and surface tension in the context of terminal flow field.

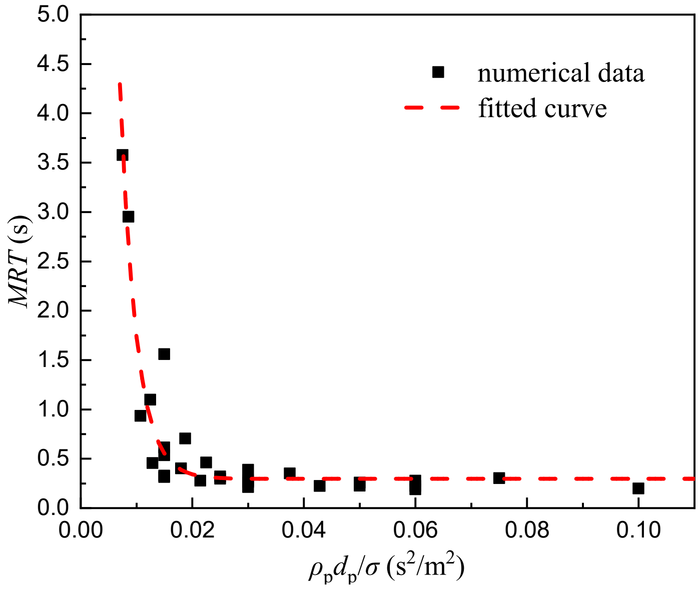

Fig. 5.33. Distribution of aerosol mean residence time.

5.6 Conclusion

In this chapter, the fundamental process of aerosol transport through a rising bubble is investigated systematically and thoroughly. The developed interfacial penetration model is calibrated and evaluated by the benchmark data in the single bubble decontamination experiment. The residence-time distribution analysis is introduced into aerosol decontamination process to examine the temporal removal behavior at first, where the characteristics is analyzed accordingly. In sum, the main conclusions are generalized here as

(1) With the introduction of interfacial penetration model, the simulation results agree well with the experimental data from both quantitative and qualitative aspects, which has confirmed the feasibility of the present model. Through parametric studies, the present model is also proved to be workable under the circumstance of changeful bubble dynamics.

(2) Aerosol motion in the gas phase is examined and aerosol internal circulation is visualized. As the gas streamline presents a large deviation in direction, the micron particles may not able to follow it closely. Aerosol internal circulation is affected by temporal bubble shape oscillation, which results in the variation in bubble internal field to affect aerosol motion thereby.

(3) Parametric studies of influential factors in the aerosol interfacial process are investigated. The influence of aerosol size and density could be attributed to the variation in aerosol inertia. The dependency of aerosol decontamination factors on surface tension coefficients is non-monotonic, which is explained by a competitive mechanism between weakened internal flow and enhanced penetration capacity.

(4) Implication of bubble dynamics on aerosol transport behavior is investigated by considering Eötvös and Galilei numbers. The increasing Eo numbers give rise to the weakened internal flow in the approaching process and the impaired surface tension force in the impacting process. The decreasing Ga numbers bring about the dampened bubble shape oscillation in the approaching process and the escalated viscous drag in the impacting process. Aerosol removal mechanism is found to be dependent on surface tension but insensitive to liquid viscosity.

(5) Irrespective of the bubble internal flow field, the profile of aerosol residence time could follow a nearly exponential decay after the initial development, whose shape is affected considerably by aerosol size and surface tension. A key parameter, namely $\rho_\mathrm{p} d_\mathrm{p}/\sigma$ is applied to characterize aerosol decontamination process within bubble swarm zone under pool scrubbing conditions, which is found to affect aerosol mean residence time critically.

6 Conclusion and Outlook

The present works focus on the fundamental process of a single bubble rising in quiescent liquid with internal aerosol transport. Regarding that, two essential aspects are of particular interest, which are bubble interfacial area and aerosol residence time. It is found that bubble interfacial area is a good criterion in simulation to describe time-dependent bubble deformation due to its three-dimensional property. With the utilization of bubble transient interfacial area, the velocity-shape dependency, bubble shape oscillation and bubble breakup are well-characterized. Bubble terminal interfacial area is deemed to be mainly dependent on Galilei and Eötvös numbers. To obtain bubble terminal interfacial area, the curve fitting is performed based on the numerical data set. Consequently, a comprehensive correlation is developed with the continuous variation in Galilei numbers, whose feasibility is also confirmed by the comparison with the previous experimental data and correlation.

In terms of particle interfacial behavior, its effect on aerosol decontamination process is included via the developed interfacial penetration model. Owing to the existence of particle interfacial behavior, aerosol decontamination process is understood by the approaching process and the impacting process separately, wherein both bubble dynamics and aerosol properties could affect these two processes remarkably. Residence-time distribution analysis is introduced into aerosol decontamination process, where the characteristics is analyzed accordingly. In sum, the most important conclusions in this thesis are summarized here as follows

(1) Regarding long-term bubble dynamics, the presence of vortex shedding affects the momentum transfer from gas phase to liquid phase and subsequently, influences bubble motion significantly. The velocity-shape dependence is found and affected by bubble motion critically. A less deformed bubble shape could beget a higher transient rising velocity under the circumstance of straight bubble trajectory. Otherwise, the velocity-shape dependence is influenced by bubble horizontal motion and bubble rising velocity may correlate the temporal bubble shape evolution partially with helical or zigzag bubble trajectory.

(2) With the continuous evolution in Galilei numbers, a comprehensive correlation is developed based on the process of data fitting, which could be written as

$$BDF = \begin{cases} 1 + 0.013 \cdot Eo^{0.63} \cdot Ga^{0.65} & (2 \le Ga \le 22, 2 \le Eo \le 9) \\ 1 + 0.106 \cdot Eo^{0.79} \cdot Ga^{-0.07} & (22 < Ga \le 200, Eo < 4.5) \\ 1 + 0.056 \cdot Eo^{0.96} & (Ga > 200, Eo < 4.5) \end{cases}$$

With the increase in small Galilei numbers to a certain size, the terminal bubble shape may shift from a stable bubble to a slightly oscillatory bubble, which could decrease terminal interfacial area because of the oscillation behaviors. When Galilei numbers are increased further, bubble terminal interfacial area is only subject to Eötvös numbers and independent of Galilei numbers.

(3) The proposed interfacial penetration model is found to be tenable. with the introduction of the present model, the simulation results agree well with the experimental data from both quantitative and qualitative aspects. Through systematical parametric studies, the present model is also proved to be workable under the circumstance of changeful bubble dynamics.

(4) As for aerosol decontamination factor, the influence of aerosol size and density could be attributed to the variation in aerosol inertia. The dependency of aerosol decontamination factors on surface tension coefficients is non-monotonic, which is explained by a competitive mechanism between weakened internal flow and enhanced penetration capacity. The increase in liquid viscosity deteriorates aerosol decontamination gradually. Aerosol removal mechanism is found to be dependent on surface tension but insensitive to liquid viscosity.

(5) In terms of aerosol residence time, a key parameter, namely $\rho_p d_p/\sigma$ is applied to characterize aerosol decontamination process within bubble swarm zone under pool scrubbing conditions, which is found to affect aerosol mean residence time critically.

With respect to the outlook in the future, the following points will be focused on:

(1) The effect of bubble interaction on aerosol decontamination factor will be checked. It is well known that a trailing bubble will accelerate in the wake of the leading bubble. The wake acceleration effect could also enhance the strength of internal flow of the trailing bubble, which could benefit aerosol decontamination thereby.

(2) According to the present analysis of aerosol mean residence time, the modeling of aeosol decontamination factor within bubble swarm zone under pool scrubbing conditions will be carried out in the future.

Bibliography

[1] Y.J. Zeng, C.P. Hale, G.F. Hewitt, S.P. Walker, Flow and heat transfer in pressurized water reactor reflood, Multiph. Sci. Technol. 22 (2010) 279-370.

[2] D. Sun, Numerical study on particle decontamination from spherical bubbles in scrubbing pools by using Eulerian–Lagrangian method, Powder Technol. 393 (2021) 692-704.

[3] C. Berna, A. Escrivá, J.L. Muñoz-Cobo, L.E. Herranz, Enhancement of the SPARC90 code to pool scrubbing events under jet injection regime, Nucl. Eng. Des. 300 (2016) 563-577.

[4] S. Gupta, L.E. Herranz, L.S. Lebel, M. Sonnenkalb, M. Pellegrini, C. Marchetto, Y. Maruyama, A. Dehbi, D. Suckow, T. Kärkelä, Integration of pool scrubbing research to enhance Source-Term calculations (IPRESCA) project–Overview and first results, Nucl. Eng. Des. 404 (2023) 112189.

[5] A.T. Wassel, A.F. Milis, D.C. Bugby, Analysis of radionuclide retention in water pools, Nucl. Eng. Des. 90.1 (1985) 87-104.

[6] S.A. Ramsdale, G. Salih, H.G. Friederichs, BUSCA-JUN91 reference manual. No. PSI--95-05. Paul Scherrer Inst. (PSI), 1995.

[7] P.C. Owczarski, K.W. Burk, SPARC-90: A code for calculating fission product capture in suppression pools, NUREG/CR-5765, (1991) 57–65.

[8] L.E. Herranz, R. Iglesias, J. Fontanet, Mitigation of source term in suppression pools: Large uncertainties in predictability, Ann. Nucl. Energy 120 (2018) 509-515.

[9] K. Lunde, R.J. Perkins, Shape Oscillations of Rising Bubbles, Appl. Sci. Res. 58 (1997) 387-408.

[10] G. Brenn, V. Kolobaric, F. Durst, Shape oscillations and path transition of bubbles rising in a model bubble column, Chem. Eng. Sci. 61 (2006) 3795-3805.

[11] Y. Abea, K. Fujiwara, S. Saito, T. Yuasa, A. Kaneko, Bubble dynamics with aerosol during pool scrubbing, Nucl. Eng. Des. 337 (2018) 96-107.

[12] A. Wang, Q. Song, Q. Yao, Behavior of hydrophobic micron particles impacting on droplet surface, Atmos. Environ. 115 (2015) 1–8.

[13] S.J. Zhu, R.Z. Liu, T. Wang, Y.J. Niu, H.F. Lu, X.L. Chen, Impact Behavior of Hydrophilic Micron Particles on a Planar Gas–Liquid Interface, Langmuir 35.47 (2019) 15017-15028.

[14] H.G. Weller, G. Tabor, H. Jasak, C. Fureby, A tensorial approach to computational continuum mechanics using object-oriented techniques, Compu. Phys. 12 (6) (1998) 620–631.

[15] F.N. Peebles, Studies on the motion of gas bubbles in liquid. Chem. Eng. Prog. 49 (2) (1953) 88–97.

[16] Z.K. Mei, X. Cheng, Modeling of interfacial area for single deformed bubble based on VOF method, Nucl. Eng. Des. 395 (2022) 111864.

[17] Z.K. Mei, X. Cheng, CFD simulation of instantaneous shape oscillation with rising velocity fluctuation for single bubble rising in water, Ann. Nucl. Energy 174 (2022) 109153.

[18] Z.K. Mei, X. Cheng, Parametric study of aerosol deposition on gas bubble surface based on CFD method, Proceedings of the 13th International Topical Meeting on Nuclear Reactor Thermal-Hydraulics Operation and Safety (NUTHOS-13), September 6-8, 2022.

[19] Z.K. Mei, X. Cheng, Impact of bubble dynamics on aerosol transport based on CFD analysis, Prog. Nucl. Energy 161 (2023) 104723.

[20] L. Gamet, M. Scala, J. Roenby, H. Scheufler, J.L. Pierson, Validation of volume-of-fluid OpenFOAM® isoAdvector solvers using single bubble benchmarks, Comput. Fluids 213 (2020) 104722.

[21] J. Hua, J.F. Stene, P. Lin, Numerical simulation of 3D bubbles rising in viscous liquids using a front tracking method, J. Comput. Phys. 227 (6) (2008) 3358–3382.

[22] D. Legendre, R. Zenit, J.R. Velez-Cordero, On the deformation of gas bubbles in liquids, Phys. Fluids. 24 (2012) 043303.

[23] M.K. Tripathi, K.C. Sahu, R. Govindarajan, Dynamics of an initially spherical bubble rising in quiescent liquid, Nat. Commun 6.1 (2015) 1-9.

[24] D.M. Sharaf, A.R. Premlata, M.K. Tripathi, B. Karri, K.C. Sahu, Shapes and paths of an air bubble rising in quiescent liquids, Phys. Fluids. 29 (2017) 122104.

[25] K. Fujiwara, K. Yoshida, A. Kaneko, Y. Abe, Experimental and numerical investigations of aerosol transportation phenomena from single bubbles, Int. J. Heat Mass Transf. 195 (2022) 123160.

[26] A. Dehbi, D. Suckow, S. Guentay, Aerosol retention in low-subcooling pools under realistic accident conditions, Nucl. Eng. Des. 203 (2-3) (2001) 229–241.

[27] L.E. Herranz, C. Lopez, J. Penalva, Investigation on jet scrubbing in nuclear reactor accidents: From experimental data to an empirical correlation, Prog. Nucl. Energy 107 (2018) 72-82.

[28] J. Yoon, Y.H. Kim, Y.H. Jeong, Observation of the jet transition at a single vertical nozzle under pool scrubbing conditions, Ann. Nucl. Energy 171 (2022) 109041.

[29] M. Farhat, P. Nerisson, L. Cantrel, M. Chinaud, O. Vauquelin, Hydrodynamic aspects of aerosols pool scrubbing, Chem. Eng. Res. Des 191 (2023) 646-657.

[30] H. Diao, Y.M. Zhou, H.F. Gu, Y.Z. Li, C.X. Yan, Experimental study on the scrubbing efficiency of aerosols contained in horizontal and vertically downward submerged gas jet, Prog. Nucl. Energy 126 (2020) 103406.

[31] A. Dehbi, D. Suckow, S. Guentay, The effect of liquid temperature on pool scrubbing of aerosols, J. Aerosol Sci. 28 (1997) S707-S708.

[32] Y.Z. Li, K. Shi, Z. Sun, H. Gu, Y. Zhou, Preliminary experimental investigation on the filtration performance of submicron insoluble aerosol in a bubble column, Front. Energy Res. 96 (2019).

[33] A. Charvet, N. Bardin-Monnier, D. Thomas, Can bubble columns be an alternative to fibrous filters for nanoparticles collection?, J. Hazard. Mater. 195 (2011) 432-439.

[34] Y.Z. Li, Z. Sun, H. Gu, Y. Zhou, Deposition characteristic of micro-nano soluble aerosol under bubble scrubbing condition, Ann. Nucl. Energy 133 (2019) 881–888.

[35] Z.K. Mei, F.L. Kong, X. Cheng, Modeling of submicron particle transport based on VOF-LPT method, Chem. Eng. Sci. 264 (2022): 118168.

[36] K. Fujiwara, W. Kikuchi, Y. Nakamura, S. Saito, T. Yuasa, A. Kaneko, Y. Abe, Experimental Study of Aerosol Behavior During Pool Scrubbing: Part 1—Visualization Measurement of Aerosol Particle in a Single Rising Bubble, International Conference on Nuclear Engineering. Vol. 51487. American Society of Mechanical Engineers, 2018.

[37] K. Fujiwara, W. Kikuchi. Y. Nakamura, T. Yuasa, S. Saito, A. Kaneko, Y. Abe, Experimental study of single-bubble behavior containing aerosol during pool scrubbing, Nucl. Eng. Des. 348 (2019) 159-168.

[38] D. Koch, A. P. Weber, Separation of gas-borne nanoparticles in bubble columns, J. Aerosol Sci. 53 (2012): 61-75.

[39] Y.Z. Li, Q.C. Ma, Z.N. Sun, H.F. Gu, Y.M. Zhou, K.Y. Shi, Study on calculation method of soluble aerosol removal efficiency under high humidity condition, Front. Energy Res. 7 (2019) 26.

[40] Y.Z. Li, Y.M. Zhou, Z.N. Sun, H.F. Gu, Q.C. Ma, H. Diao, Analysis of hygroscopic growth properties of soluble aerosol under severe nuclear accidents conditions, Prog. Nucl. Energy 127 (2020) 103464.

[41] H.M. Sun, S. Macida, Y. Sibamoto, Y. Okagaki, T. Yonomoto, Experimental investigation on dependence of decontamination factor on aerosol number concentration in pool scrubbing under normal temperature and pressure, International Conference on Nuclear Engineering. Vol. 51487. American Society of Mechanical Engineers, 2018.

[42] H.M. Sun, Y. Sibamoto, Y. Okagaki, T. Yonomoto, Experimental investigation of decontamination factor dependence on aerosol concentration in pool scrubbing, Sci. Technol. Nucl. Install. 2019 (2019) 1–15.

[43] Y.Y. Xu, J. Deng, Z.Q. Zou, G.M. Jiang, X.L. Wu, Experimental study on aerosol behavior in water pool scrubbing under severe accident conditions, International Journal of Advanced Nuclear Reactor Design and Technology 2 (2020) 111-116.

[44] Y.H. Kim, Y.H. Jeong, Preliminary aerosol concentration effect modeling in pool scrubbing code, Transactions of the Korean Nuclear Society Virtual Spring Meeting July 9-10, 2020.

[45] N.A. Fuchs, The Mechanics of Aerosols, Pergamon Press, 1964.

[46] L.W. He, Y.X. Li, Y. Zhou, S. Chen, L.L. Tong, X.W. Cao, Investigation on aerosol pool scrubbing model during severe accidents, Front. Energy Res. 9 (2021) 691419.

[47] T.S. Laker, S.M. Ghiaasiaan, Monte-Carlo simulation of aerosol transport in rising spherical bubbles with internal circulation, J. Aerosol Sci. 35 (4) (2004) 473-488.

[48] K. Motegi, Y. Sibamoto, Y. Kukita, Nonuniform particle distribution and interference between removal mechanisms during unsteady aerosol deposition from a rising spherical bubble, J. Nucl. Sci. Technol, 59 (8) (2022) 1037-1046.

[49] D. Sun, Particle decontamination from elliptical bubbles in scrubbing pools simulated using Eulerian–Lagrangian method, Powder Technol. 397 (2022) 117003.

[50] K. Motegi, Y. Sibamoto, Y. Kukita, Scalability of inertial particle deposition in bubbles with internal circulation, Ann. Nucl. Energy 184 (2023) 109679.

[51] M.J.M. Hill, VI. On a spherical vortex, Philos. Trans. Royal Soc. A 185 (1894) 213–245.

[52] M.K. Akbar, S.M. Ghiaasiaan, Monte Carlo simulation of aerosol transport in rising gas bubbles undergoing shape deformation, J. Aerosol Sci. 37 (6) (2006) 735–749.

[53] I. Mirzaee, M. Song, M. Charmchi, H. Sun, A microfluidics-based on-chip impinger for airborne particle collection, Lab Chip, 16 (12) (2016) 2254-2264.

[54] W. Pan, X. Chen, G. Dai, F. Wang, Enhanced effect of bubble deformation on internal particle transport, Ind. Eng. Chem. Res. 59 (2) (2020) 905–918.

[55] L. Liu, H. Yan, G. Zhao, Experimental studies on the shape and motion of air bubbles in viscous liquids, Exp. Therm. Fluid Sci. 62 (2015) 109-121.

[56] M. Rastello, J.L. Marié, M. Lance, Drag and lift forces on clean spherical and ellipsoidal bubbles in a solid-body rotating flow, J. Fluid Mech. 682 (2011) 434-459.

[57] D.W. Moore, The velocity of rise of distorted gas bubbles in a liquid of small viscosity, J. Fluid Mech. 23 (1965) 749-766.

[58] A. Tomiyama, H. Tamai, I. Zun, S. Hosokawa, Transverse migration of single bubbles in simple shear flows, Chem. Eng. Sci. 57 (2002a) 1849-1858.

[59] J. Vries, S. Luther, D. Lohse, Induced bubble shape oscillations and their impact on the rise velocity, Eur. Phys. J. B 29 (2002), 503-509.

[60] A. Tomiyama, G.P. Celata, S. Hosokawa, S. Yoshida, Terminal velocity of single bubbles in surface tension force dominant regime, Int. J. Multiph. Flow 28 (9) (2002) 1497–1519.

[61] X. Yan, Y.M. Zhou, H. Diao, H.F. Gu, Y.Z. Li, Development of mathematical model for aerosol deposition under jet condition, Ann. Nucl. Energy 142 (2020) 107394.

[62] Y.C. Bian, F. Dong, W.D. Zhang, H.Y. Wang, C. Tan, Z.Q. Zhang, 3D reconstruction of single rising bubble in water using digital image processing and characteristic matrix, Particuology 11.2 (2013) 170-183.

[63] J.M. Wen, Q.N. Sun, Z.N. Sun, H.F. Gu, An improved image processing technique for determination of volume and surface area of rising bubble, Int. J. Multiph. Flow 104 (2018) 294-306.

[64] F. Özkan, A. Wenka, E. Hansjosten, P. Peter, Numerical investigation of interfacial mass transfer in two phase flows using the VOF method, Eng. Appl. Comput. Fluid Mech. 10 (2015) 100-110.

[65] G.Y. Soh, G.H. Yeoh, V. Timchenko, An algorithm to calculate interfacial area for multiphase mass transfer through the volume-of-fluid method, Int. J. Heat Mass Transf. 100 (2016) 573-581.

[66] B. Lalanne, S. Tanguy, F. Risso, Effect of rising motion on the damped shape oscillations of drops and bubbles, Phys. Fluids. 25 (2013) 112107.

[67] W.X. Chen, C.X. Huang, P.B. Wei, S.L. Song, B.B. Qiu, Q.B. Zhao, J.J. Yan, Numerical simulation of underwater air bubble formation under rolling conditions, Ann. Nucl. Energy 143 (2020) 107451.

[68] Q.C. Ma, Y.M. Zhou, H.F. Gu, Z.N. Sun, L.J. Li, X.P. Cui, Experimental research on aerosol deposition phenomenon in single-sized rising bubble, Prog. Nucl. Energy 154 (2022) 104456.

[69] D. Jacquemain, Status report on filtered containment venting, Organisation for Economic Co-operation and Development/Nuclear Energy Agency/Committee on the Safety of Nuclear Installations, Paris, France/Boulogne-Billancourt, France, Report No. NEA/CSNI 7 (2014).

[70] J. Pich, W. Schütz, On the theory of particle deposition in rising gas bubbles: the absorption minimum, J. Aerosol Sci. 22 (3) (1991) 267-272.

[71] R.M. Davies, G.I. Taylor, The mechanics of large bubbles rising through extended liquids and through liquids in tubes, Proceedings of the Royal Society of London. Series A. Mathematical and Physical Sciences, 200 (1062) (1950) 375-390.

[72] C.A. Galeano-Rios, R. R. Cimpeanu, I.A. Bauman, A. MacEwen, P.A. Milewski, D.M. Harris, Capillary-scale solid rebounds: experiments, modelling and simulations, J. Fluid Mech. 912 (2021) A17.

[73] D.-G. Lee, H.-Y. Kim, Impact of a superhydrophobic sphere onto water, Langmuir 24 (1) (2008) 142–145.

[74] D. Liu, Q. He, G.M. Evans, Penetration behaviour of individual hydrophilic particle at a gas–liquid interface, Adv. Powder Technol. 21.4 (2010) 401-411.

[75] J.M. Aristoff, J.W.M. Bush, Water entry of small hydrophobic spheres, J. Fluid Mech. 619 (2009) 45-78.

[76] A. Wang, Q. Song, B. Ji, Q. Yao, In-situ observation of hydrophobic micron particle impaction on liquid surface, Powder Technol. 311 (2017) 408–415.

[77] B.Q. Ji, Q. Song, Q. Yao, Numerical study of hydrophobic micron particle's impaction on liquid surface, Phys. Fluids 29 (2017) 77102.

[78] B.Q. Ji, Q. Song, K. Shi, J.H. Liu, Q. Yao, Oblique impact of microspheres on the surface of quiescent liquid, J. Fluid Mech. 900 (2020) A17.

[79] B.Q. Ji, Z.Z. Tang, Q. Song, Oblique impact dynamics of micron particles onto a liquid surface, Phys. Rev. Fluids 5.11 (2020) 114006.

[80] S. Zhu, C. Zhao, J. Lin, W. Zhang, Y. Sheng, X. Chen, Impact behavior of hydrophilic microparticles on the particle-laden interface, Chem. Eng. Sci. 227 (2020) 115913.

[81] S.J. Zhu, R.Z. Liu, T. Wang, Y.J. Niu, H.-F. Lu, X.L. Chen, Penetration time of hydrophilic micron particles impacting into an unconfined planar gas-liquid interface, Chem. Eng. Sci. 193 (2019) 282–297.

[82] S.J. Zhu, C.X. Zhao, H.F. Lu, X.L. Chen, Influence of surfactant on the penetration time of hydrophilic microparticles impacting into the gas–liquid interface at low impact velocities, Chem. Eng. Res. Des. 160 (2020) 383-394.

[83] H.S. Fogler, Elements of Chemical Reaction, 2020.

[84] J. Brackbill, D. Kothe, C. Zemach, A continuum method for modeling surface tension, J. Comput. Phys. 100 (2) (1992) 335–354.

[85] S.S. Deshpande, L. Anumolu, M.F. Trujillo, Evaluating the performance of the two-phase flow solver interFoam, Comput. Sci. Discov. 5 (1) (2012) 014016.

[86] J. Roenby, H. Bredmose, H. Jasak, A computational method for sharp interface advection, R. Soc. Open Sci. 3 (11) (2016): 160405, doi: 10.1098/rsos.160405.

[87] A. Li, G. Ahmadi, Dispersion and deposition of spherical particles from point sources in a turbulent channel flow, Aerosol Sci. Technol. 16 (4) (1992) 209–226.

[88] H. Ounis, G. Ahmadi, J.B. McLaughlin, Brownian diffusion of submicrometer particles in the viscous sublayer, J. Colloid Interface Sci. 143 (1) (1991) 266–277.

[89] W. Dolshanskiy, A. Stepanyuk, E. Arian, W. Pauer, Residence time distribution and micromixing efficiency of a dynamic inline rotor–stator mixer, Chem. Eng. J. 451 (2023) 138555.

[90] A.E. Rodrigues, Residence time distribution (RTD) revisited, Chem. Eng. Sci. 230 (2021) 116188.

[91] L. Liu, H.J Yan, G.J. Zhao, J.C. Zhuang, Experimental studies on the terminal velocity of air bubbles in water and glycerol aqueous solution, Exp. Therm. Fluid Sci. 78 (2016) 254-265.

[92] W. Kracht, J.A. Finch, Effect of frother on initial bubble shape and velocity, Int. J. Miner. Process. 94 (2010) 115-120.

[93] M. Maldonado, J.J. Quinn, C.O. Gomez, J.A. Finch, An experimental study examining the relationship between bubble shape and rise velocity, Chem. Eng. Sci. 98 (2013) 7-11.

[94] Y.W. Cao, M.J. Rafael, Numerical investigation of central breakup of large bubble induced by liquid jet, Phys. Fluids 32.3 (2020) 033302.

[95] Y.W. Cao, M.J. Rafael, Numerical study of the central breakup behaviors of a large bubble rising in quiescent liquid, Chem. Eng. Sci. 225 (2020) 115804.
[96] F, Bernardo, D. Legendre, Mass or heat transfer from spheroidal gas bubbles rising through a stationary liquid, Chem. Eng. Sci. 65.23 (2010) 6296-6309.
[97] Y. Zhao, H. Yang, L.S. Fan, Numerical simulation of bubble interactions using an adaptive lattice Boltzmann method, Chem. Eng. Sci. 66.14 (2011) 3441-3451.
[98] M. Gumulya, R.P. Utikar, G.M. Evans, J.B. Joshi, V. Pareek, Interaction of bubbles rising inline in quiescent liquid, Chem. Eng. Sci. 166 (2017) 1-10.
[99] A. Senapati, G. Singh, R. Lakkaraju, Numerical simulations of an inline rising unequal-sized bubble pair in a liquid column, Chem. Eng. Sci. 208 (2019) 115159.
[100] S.K. Friedlander, W.H. Marlow, Smoke, Dust and Haze: Fundamentals of Aerosol Behavior, Phys. Today 30 (1977) 58–59.
[101] L.E. Herranz, V. Peyrés, J. Polo, M.J. Escudero, M.M. Espigares, J. López-Jiménez, Experimental and analytical study on pool scrubbing under jet injection regime, Nucl. Technol. 120.2 (1997) 95-109.

List of Publications

Zhongkai Mei, Fanli Kong, Xu Cheng, Modeling of submicron particle transport based on VOF-LPT method, Chem. Eng. Sci. 264 (2022) 118168.

Zhongkai Mei, Xu Cheng, CFD simulation of instantaneous shape oscillation with rising velocity fluctuation for single bubble rising in water, Ann. Nucl. Energy 174 (2022) 109153.

Zhongkai Mei, Xu Cheng, Modeling of interfacial area for single deformed bubble based on VOF method, Nucl. Eng. Des. 395 (2022) 111864.

Zhongkai Mei, Xu Cheng, Impact of bubble dynamics on aerosol transport based on CFD analysis, Prog. Nucl. Energy 161 (2023) 104723.

Zhongkai Mei, Xu Cheng, Parametric study of aerosol deposition on gas bubble surface based on CFD method, Proceedings of the 13th International Topical Meeting on Nuclear Reactor Thermal-Hydraulics Operation and Safety (NUTHOS-13), September 6-8, 2022.

Zhongkai Mei, Xu Cheng, Influence of gas-liquid surface tension on aerosol removal based on CFD method, Computational Fluid Dynamics for Nuclear Reactor Safety (CFD4NRS-9), February 20-21, 2023.